NORTH ATLANTIC TREATY ORGANIZATION

Science & Technology Organization (STO)

*AC/323(AVT-218)TP/1203*

**STO TECHNICAL REPORT** **TR-AVT-318**

# Low Noise Aeroacoustic Design for Turbofan Powered NATO Air Vehicles

(Conception aéroacoustique à faible bruit pour les véhicules aériens de l'OTAN propulsés par un réacteur à double flux)

This report contains the results of the RTG AVT-318

active in the period 2019 – 2023.

Published November 2024

*Distribution and Availability on Back Cover*

NORTH ATLANTIC TREATY ORGANIZATION


*AC/323(AVT-218)TP/1203*

**STO TECHNICAL REPORT** **TR-AVT-318**

# Low Noise Aeroacoustic Design for Turbofan Powered NATO Air Vehicles

(Conception aéroacoustique à faible bruit pour les véhicules aériens de l'OTAN propulsés par un réacteur à double flux)

This report contains the results of the RTG AVT-318

active in the period 2019 – 2023.

# The NATO Science and Technology Organization

Science & Technology (S&T) in the NATO context is defined as the selective and rigorous generation and application of state-of-the-art, validated knowledge for defence and security purposes. S&T activities embrace scientific research, technology development, transition, application and field-testing, experimentation and a range of related scientific activities that include systems engineering, operational research and analysis, synthesis, integration and validation of knowledge derived through the scientific method.

In NATO, S&T is addressed using different business models, namely a collaborative business model where NATO provides a forum where NATO Nations and partner Nations elect to use their national resources to define, conduct and promote cooperative research and information exchange, and secondly an in-house delivery business model where S&T activities are conducted in a NATO dedicated executive body, having its own personnel, capabilities and infrastructure.

The mission of the NATO Science & Technology Organization (STO) is to help position the Nations' and NATO's S&T investments as a strategic enabler of the knowledge and technology advantage for the defence and security posture of NATO Nations and partner Nations, by conducting and promoting S&T activities that augment and leverage the capabilities and programmes of the Alliance, of the NATO Nations and the partner Nations, in support of NATO's objectives, and contributing to NATO's ability to enable and influence security and defence related capability development and threat mitigation in NATO Nations and partner Nations, in accordance with NATO policies.

The total spectrum of this collaborative effort is addressed by six Technical Panels who manage a wide range of scientific research activities, a Group specialising in modelling and simulation, plus a Committee dedicated to supporting the information management needs of the organization.

- AVT Applied Vehicle Technology Panel
- HFM Human Factors and Medicine Panel
- IST Information Systems Technology Panel
- NMSG NATO Modelling and Simulation Group
- SAS System Analysis and Studies Panel
- SCI Systems Concepts and Integration Panel
- SET Sensors and Electronics Technology Panel

These Panels and Group are the power-house of the collaborative model and are made up of national representatives as well as recognised world-class scientists, engineers and information specialists. In addition to providing critical technical oversight, they also provide a communication link to military users and other NATO bodies.

The scientific and technological work is carried out by Technical Teams, created under one or more of these eight bodies, for specific research activities which have a defined duration. These research activities can take a variety of forms, including Task Groups, Workshops, Symposia, Specialists' Meetings, Lecture Series and Technical Courses.

The content of this publication has been reproduced directly from material supplied by STO or the authors.

Published November 2024



ISBN 978-92-837-2514-5

# Table of Contents

# List of Figures

# List of Tables

# AVT-318 Membership List

## CO-CHAIRS

Prof. Dr.-Ing. Jan Werner DELFS
DLR Braunschweig
GERMANY
Email: Jan.Delfs@dlr.de

Mr. Karl-Stéphane ROSSIGNOL
DLR German Aerospace Center
GERMANY
Email: Karl-Stephane.Rossignol@dlr.de

Dr. Russell THOMAS
NASA Langley Research Center
UNITED STATES
Email: russell.h.thomas@nasa.gov

## MEMBERS

Dr. Luca BENASSI
Airbus Defence and Space
GERMANY
Email: lucabenassi@hotmail.com

Dr. Francesco CENTRACCHIO
Università degli studi Roma Tre
ITALY
Email: francesco.centracchio@uniroma3.it

Mr. Fabrizio DE GREGORIO
Centro Italiano Ricerche Aerospaziali – CIRA
ITALY
Email: f.degregorio@cira.it

Mr. Samuel GOTTFARB BART
Swedish Defence Research Agency FOI
(at FOI until October 2023)
SWEDEN
Email: samuel.gottfarb.bart@foi.se

Prof. Umberto IEMMA
University Roma Tre
ITALY
Email: umberto.iemma@uniroma3.it

Mr. Mattias JOHN QUAS
Swedish Defence Research Agency, FOI
SWEDEN
Email: mattias.john.quas@foi.se

Dr. Alexander KOLB
Airbus Defence & Space GmbH
GERMANY
Email: alexander.kolb@airbus.com

Dr. Carsten LENFERS
German-Dutch Wind Tunnels
GERMANY
Email: carsten.lenfers@dnw.aero

Dr. Eric MANOHA
ONERA
FRANCE
Email: eric.manoha@onera.fr

Mr. Giorgio PALMA
Università Roma Tre
ITALY
Email: giorgio.palma@uniroma3.it

Mr. David PATIENCE (ret. 2022)
BAE Systems
UNITED KINGDOM
Email: david.patience@baesystems.com

Mr. Patrick ZIMMERMANN
Airbus Defence and Space GmbH
GERMANY
Email: patrick.p.zimmermann@de.airbus.com

## ADDITIONAL CONTRIBUTORS

Dr. Lorenzo BURGHIGNOLI
Universita' Roma Tre
ITALY
Email: lorenzo.burghignoli@uniroma3.it

Mr. Carmelo IZZO
CIRA
ITALY
Email: c.izzo@cira.it

Prof. Roberto CAMUSSI
Universita' Roma Tre
ITALY
Email: roberto.camussi@uniroma3.it

Prof. Shia-Hui PENG (at FOI until April 2023)
Swedish Defence Research Agency FOI
SWEDEN
Email: *unavailable*

## PANEL/GROUP MENTOR

Prof. Dr. Cord ROSSOW
DLR
GERMANY
Email: cord.rossow@dlr.de

# Low Noise Aeroacoustic Design for Turbofan Powered NATO Air Vehicles

## (STO-TR-AVT-318)

# Executive Summary

Military air vehicles cover a broad range of size and function, from large transports to small U(C)AVs to the turbojets of high-powered fighters. The typically intense exterior noise generated by all of these is of aerodynamic origin and this noise represents a problem in peace times during training operation and at wartime due to the acoustic detectability of operating combat aircraft. The state of the art of aircraft noise prediction and reduction is aligned with civil transport aircraft, while much less effort has been invested in noise reduction of military aircraft. Noise reduction concepts can only partially be adopted from the civilian side, because of the largely different aircraft configurations in the military domain. Military aircraft noise is practically entirely determined by engine noise. While turbofan engine noise reduction for civil aircraft is a very active topic of research and technology, any progress in this field is completely insufficient for military aircraft. The engine integration in combination with the aircraft configuration at military aircraft is vastly different which changes the relevant sound source mechanisms and also provides significant potential for noise reduction, not available at typical tube-and-wing civil aircraft. For instance, conceptually, certain techniques exploited to reduce the infrared signature of combat aircraft may be transferred to reduce sound radiation.

AVT-318 “Low Noise Aeroacoustic Design for Turbofan Powered NATO Air Vehicles,” focused on the MULDICON vehicle and added the jet noise source from the rectangular nozzle including the jet-trailing edge interaction arising from the highly integrated nozzle/airframe as well as a characterization of the inlet acoustic radiation. Experimental campaigns included a monopole point source generated inside the inlet duct and exhaust ducts. Considerable CFD and CAA studies were performed of the powered vehicle. An initial effort was performed to develop a noise reduction device, the Shielding Flap, that could be feasible to integrate with the MULDICON. Experimental and prediction studies were performed to understand the design parameters of the Shielding Flap and their acoustic impacts.

Of particular interest is a first time aeroacoustic characterization of intake and exhaust sound radiation of a UCAV-type military vehicle and a series of experiments on the Shielding Flap concept. A low noise concept in the form of a trailing edge deployable devices used to shield aft radiated jet noise. The database assembled in AVT-318 consists in wind tunnel investigations of the DLR-F24 MULDICON model conducted in the acoustic test section the DNW-NWB facility as well as generic investigations of the Shielding Flap concept in the Quiet Flow Facility at NASA. While the tests were coordinated respectively by DLR and NASA, all partners have contributed with various activities to the design and realization of the model, including flow simulations. Each group has done predictions of either the installed jet and/or the intake/exhaust diffraction problem with their respective aeroacoustic prediction suites. A dedicated code-to-code and codes-to-experiments study was accomplished.

# Conception aéroacoustique à faible bruit pour les véhicules aériens de l'OTAN propulsés par un réacteur à double flux

## (STO-TR-AVT-318)

# Synthèse

Les véhicules aériens militaires ont une large gamme de dimensions et de fonctions, depuis les grands véhicules de transport jusqu'aux petits U(C)AV, en passant par les turboréacteurs des avions de chasse très puissants. Le bruit extérieur généralement intense produit par tous ces appareils est d'origine aérodynamique et représente un problème en temps de paix, pendant l'entraînement, et en temps de guerre, à cause de la détectabilité acoustique des avions de combat en service. L'état de la technique de prédiction et réduction du bruit des aéronefs est aligné sur celui des aéronefs de transport civil, mais beaucoup moins d'efforts ont été consacrés à la réduction du bruit des appareils militaires. Les concepts de réduction du bruit appliqués aux appareils civils ne peuvent être que partiellement appliqués aux appareils militaires, parce que leur configuration est très différente. Le bruit des avions militaires provient presque entièrement des moteurs. Alors que la réduction du bruit des turboréacteurs à double flux dans les aéronefs civils suscite beaucoup de recherches et de technologies, tout progrès dans ce domaine est totalement insuffisant pour les aéronefs militaires. L'intégration du moteur et la configuration de l'aéronef sont extrêmement différentes dans le domaine militaire, ce qui modifie les mécanismes à l'origine du bruit et offre également un grand potentiel de réduction du bruit, non applicable aux aéronefs civils classiques à tube et ailes. Par exemple, sur le plan conceptuel, certaines techniques exploitées pour réduire la signature infrarouge des aéronefs de combat pourraient servir à réduire le rayonnement sonore.

L'AVT-318 « Conception aéroacoustique à faible bruit pour les véhicules aériens de l'OTAN propulsés par un réacteur à double flux » s'est concentré sur le véhicule MULDICON et y a ajouté la source de bruit de la tuyère rectangulaire du réacteur – en incluant l'interaction avec le bord de fuite du réacteur du fait de l'intégration poussée entre la tuyère et la cellule – ainsi qu'une caractérisation du rayonnement acoustique de l'admission. Les campagnes expérimentales incluaient une source ponctuelle monopole générée à l'intérieur de la conduite d'admission et des conduites d'échappement. D'importantes études CFD et CAA ont été réalisées sur le véhicule propulsé. Des travaux se sont d'abord attachés à développer un dispositif de réduction du bruit, à savoir le volet de protection (Shielding Flap), qui pourrait être intégré au MULDICON. Des études expérimentales et prédictives ont été menées pour comprendre les paramètres de conception du volet de protection et leurs effets acoustiques.

Signalons en particulier une toute première caractérisation aéroacoustique du rayonnement sonore de l'admission et de l'échappement d'un véhicule militaire de type UCAV et une série d'expériences sur le concept de volet de protection. Un concept à faible bruit a été présenté sous la forme de dispositifs déployables sur le bord de fuite, servant à faire barrière au rayonnement sonore du réacteur vers l'arrière. La base de données assemblée au sein de l'AVT-318 se compose d'études en soufflerie du modèle MULDICON DLR-F24, menées dans la section d'essai acoustique de l'installation DNW-NWB, ainsi que d'études générales du concept de volet de protection dans l'installation Quiet Flow Facility de la NASA. Bien que les essais aient été coordonnés respectivement par le DLR et la NASA, tous les partenaires ont contribué à la conception et à la réalisation du modèle par diverses activités, y compris des simulations d'écoulement. Chaque groupe a réalisé des prédictions sur le réacteur installé et/ou le problème de diffraction de l'admission/échappement, au moyen de sa suite respective de prédiction aéroacoustique. Une étude a été spécialement menée pour comparer les codes entre eux et les codes aux expériences.

# Chapter 1 – INTRODUCTION

**Karl-Stéphane Rossignol and Jan Delfs**
DLR
GERMANY

**Russell Thomas**
NASA
UNITED STATES

## 1.1 BACKGROUND

Military air vehicles cover a broad range of size and function, from large transports to small U(C)AVs to the turbojets of high-powered fighters. The typically intense exterior noise generated by all of these is of aerodynamic origin and this noise represents a problem in peace times during training operation and at wartime due to the acoustic detectability of operating combat aircraft. The state of the art of aircraft noise prediction and reduction is aligned with civil transport aircraft, while much less effort has been invested in noise reduction of military aircraft. Noise reduction concepts can only partially be adopted from the civilian side, because of the largely different aircraft configurations in the military domain. Military aircraft noise is practically entirely determined by engine noise. While turbofan engine noise reduction for civil aircraft is a very active topic of research and technology, any progress in this field is completely insufficient for military aircraft. The engine integration in combination with the aircraft configuration at military aircraft is vastly different which changes the relevant sound source mechanisms and also provides significant potential for noise reduction, not available at typical tube-and-wing civil aircraft. For instance, conceptually, certain techniques exploited to reduce the infrared signature and radar cross-section of combat aircraft may be transferred to reduce sound radiation. The following STO research activities in the past have contributed to set the background to the AVT-318:

- AVT-132 “Noise issues arising from the operation of gas turbine powered military air vehicles”.
- The specialists meeting AVT-158 addressed the noise from high-powered aircraft such as fighters, both in the community and on a carrier deck.
- AVT-233 “Aeroacoustics of engine installation of military air vehicles” has established a validated computational tool basis to enable the prediction of acoustic installation effects of arbitrary configurations, achieved by numerical simulation (CAA = Computational Aeroacoustics). Starting from generic geometries (airfoil), to a Hybrid Wing Body configuration (HWB) and ending with a military transport configuration and the agile NATO type UAS configuration SACCON the RTG was focused on validating these CAA codes in view of their capability to predict the acoustic shielding of engine noise. The source was deliberately kept highly generic (basically a monopole point source).
- AVT-251 has been providing the overall aircraft design of an aerodynamically advanced and realistic configuration of SACCON type, called MULDICON, which forms the focus of the proposed RTG; in that respect also AVT-161 and AVT-201 were instrumental in laying the foundations for AVT-251.

AVT-318 “Low Noise Aeroacoustic Design for Turbofan Powered NATO Air Vehicles,” focused on the MULDICON vehicle and added the jet noise source from the rectangular nozzle including the jet-trailing edge interaction arising from the highly integrated nozzle/airframe as well as a characterization of the inlet acoustic radiation. Experimental campaigns included a monopole point source generated inside the inlet duct and exhaust ducts. Considerable CFD and CAA studies were performed of the powered vehicle. An initial effort was performed to develop a noise reduction device, the Shielding Flap, that could be feasible to integrate with the MULDICON. Experimental and prediction studies were performed to understand the design parameters of the Shielding Flap and their acoustic impacts.

## 1.2 TOPICS OF AVT-318

AVT-318 is naturally concerned with aeroacoustics and the disciplines directly related to it, i.e., aerodynamics of high-speed subsonic flows, including turbulence and aircraft design. Specifically:

- Focus on aeroacoustic installation because of the relevance to acoustic detectability and annoyance of military aircraft. In this respect, the design of geometries which a) maximize the exploitation of acoustic shielding, and b) minimize installation related excess source noise.
- Qualification of aircraft noise prediction methods with regard to propulsion system installation effects, as far as installation sources for jet and acoustic installation properties of complex intakes and exhausts is concerned.
- Source noise of jet-powered agile military air vehicles, e.g., MULDICON.
- Source to receiver propagation as a basis for acoustic design assessment.
- Aeroacoustic simulation (CFD/CAA) with tools of different fidelity: RANS+perturbations, Scale resolving approaches, integral methods, as tested/validated on generic configurations in AVT-233.

AVT-318 represents the next R&T step after AVT-233 (and partially AVT-251) on the aeroacoustics of agile air vehicles of SACCON type. While AVT-233 tested/validated tools on relevant but simplified aircraft geometries and with very simple sources, this RTG considers a much more realistic and detailed geometry including a realistic extended jet noise source. The MULDICON configuration appears highly appropriate, particularly because it has gone through a thorough multidisciplinary design process in AVT-251. Acoustic installation properties of the geometries with respect to (turbofan) noise propagating from the intake and the exhaust were analyzed.

Of particular interest is a first time aeroacoustic characterization of intake and exhaust sound radiation of a UCAV-type military vehicle and a series of experiments on the Shielding Flap concept. A low noise concept in the form of a trailing edge deployable device is used to shield aft radiated jet noise. The database assembled in AVT-318 consists in wind tunnel investigations of the DLR-F24 MULDICON model conducted in the acoustic test section the DNW-NWB facility as well as generic investigations of the Shielding Flap concept in the Quiet Flow Facility at NASA. While the tests were coordinated respectively by DLR and NASA, all partners have contributed with various activities to the design and realization of the model, including flow simulations. Each group has done predictions of either the installed jet and/or the intake/exhaust diffraction problem with their respective aeroacoustic prediction suites. A dedicated code-to-code and codes-to-experiments study was accomplished.

## 1.3 OBJECTIVES OF AVT-318

Task Group to focus on:

- Demonstrating (on a realistic configuration) the qualification and applicability of tools for the prediction of the effects of propulsion system installation on received sound (using acoustics characteristics of the propulsion system without the engine itself).
- Additionally, the important topic of predicting noise reduction technology as an exercise in aeroacoustic design at agile NATO air vehicles will be covered, particularly at the MULDICON configuration.
- The mentioned objectives imply not only code-to-code comparisons among partners, but a dedicated validation dataset from tests in an appropriate (i.e., large enough size) acoustic wind tunnel, which is to be accomplished as well.

The task group is meant to fill an existing gap as far as i) Reliable prediction of noise from military aircraft; and ii) Simulation assisted low noise design is concerned. After completion of the RTG this capability shall have been demonstrated at a highly relevant agile NATO air vehicle. As far as the knowledge readiness level of the activity is concerned, one has to keep in mind that aeroacoustics is relatively new to the field of aircraft design, especially providing means to include noise in the early design phase of military aircraft.

Although the proposed research task is definitely focusing on a military aircraft class, much of the new knowledge to be gained will be applicable in the civilian domain as well (e.g., sound radiation from semi-buried intakes).

## 1.4 WORK PLAN

According to the defined contents of AVT-318 a work breakdown structure was set up. Four main technical work packages were established, plus a reporting phase as a concluding package:

- **WP 1:** Common wind tunnel tests.
- **WP 2:** Tool adjustment.
- **WP 3:** Analysis and validation.
- **WP 4:** Low noise design.
- **WP 5:** Reporting.

AVT-318 was initially planned to extend over a timespan from 2019 to 2021 (Figure 1-1). In 2020, a two year extension was granted to the group which finally ended by end of 2023 (Figure 1-2).

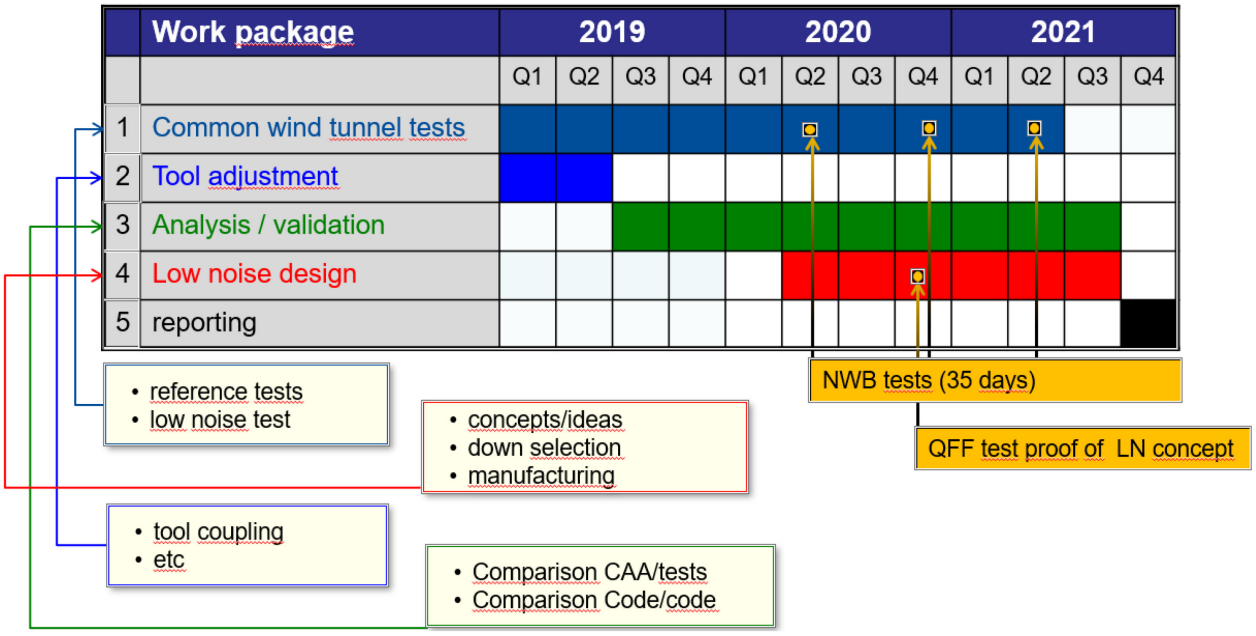


**Figure 1-1: Work Packages of AVT-318 and Original Schedule Before the Grant of a Two Year Extension.**

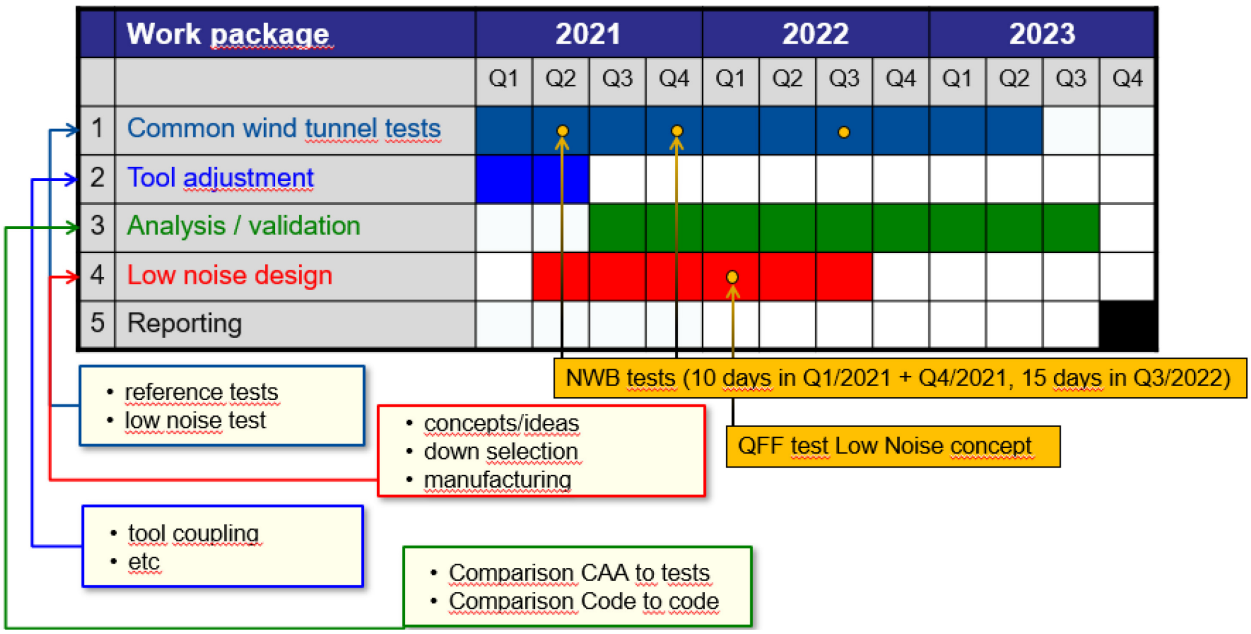


**Figure 1-2: Work Packages of AVT-318 and Schedule After the Grant of a Two Year Extension.**

# Chapter 2 – COMMON WIND TUNNEL TESTS

**Karl-Stéphane Rossignol and Jan Delfs**
DLR
GERMANY

**Florence Hutcheson**
NASA
UNITED STATES

**Fabrizio De Gregorio and Carmello Izzo**
CIRA
ITALY

## 2.1 WIND TUNNEL MODEL

### 2.1.1 DLR-F24 MULDICON UCAV Model

Karl-Stéphane Rossignol and Jan Delfs, DLR, GERMANY

The original MULDICON (MULti-Disciplinary CONfiguration) configuration was developed in the framework of NATO STO Task Group AVT-251 (Conceptual UCAV Design). The aim of this Task Group was to perform an aerodynamic re-design of the SACCON UCAV, only through the use of flow simulations methods i.e., CFD. This was made possible through knowledge gained throughout earlier Task Groups. In AVT-161, the ability of computational methods to accurately predict static and dynamic stability was evaluated. The AVT-201 Task Group aimed at including control surfaces in the aerodynamic assessment as well as investigating ways to perform full flight simulations [1]. AVT-251 was not about designing a competitive UCAV but rather aimed at improving SACCON while making it a realistic, flyable, vehicle. To achieve this goal SACCON was first evaluated with respect to its ability to fulfil a flight mission, i.e., prescribed flight trajectory at a given altitude of 11 km and Mach number of 0.8 for a given payload [1]. The result of this evaluation emphasized the poor control characteristics of SACCON, due to the high-sweep design of its trailing edges. This led the group to design a new configuration, MULDICON, circumventing the issues encountered with SACCON.

In AVT-318 DLR provided an experimental wind tunnel setup based on the MULDICON UCAV configuration. The original MULDICON UCAV planform design, which originated in NATO AVT-251 [1], was adopted and modified to allow, from an experimental standpoint, the integration of an intake and an exhaust channel, as depicted in Figure 2-1. The original planform remained untouched while the centerbody design by FOI (Swedish Defence Research Agency) was selected [2]. This design has a thicker centerbody, leaving more room for the intake and exhaust channels integration. The centerbody and intake are based on a design by FOI [2], while the nozzle is a DLR-design. The complex curved intake and nozzle geometries were designed with radar signature minimization in mind, with no a priori consideration of the acoustic radiation problem. The wind tunnel model is referenced as the DLR-F24 UCAV MULDICON model. Its planform dimensions are given in Figure 2-2.

The design allows for the realization of a controlled high-velocity intake flow as well as a cold high-velocity exhaust jet; through a connection to a suction air system or a pressurized air supply, respectively. An intake suction mass-flow rate on the order of 0.9 kg/s was achieved in the experiments while a mass-flow rate on the order of 1.8 kg/s, corresponding to an estimated jet Mach number of 0.8, can be reached at the nozzle. The model is equipped with 58 surface pressure taps to acquire aerodynamic loads as well as total pressure ports to monitor the model internal plenum pressure.

The test bed was specifically designed for testing in the anechoic test section of the low-speed acoustic wind tunnel of DNW in Braunschweig (DNW-NWB), e.g., Figure 2-11, and thus for subsonic test conditions up to a Mach number of 0.2. The overall design of the DLR-F24 MULDICON model is highly modular to allow

the intake, nozzle, and internals to be easily modified or be replaced by other designs, e.g., Figure 2-3. This is especially interesting with regard to the evaluation of noise mitigation technologies and also adds some flexibility in dealing with various experimental measurement technique requirements. The main components of the model are also displayed in Figure 2-3. Both the intake and nozzle were fabricated through rapid prototyping techniques and painted to obtain a smooth surface finish. The middle part of the model consists of the internal plenum which is accessible through rectangular opening on the upper and lower side. On each side of the central plenum, two openings provide the interface where pressurized air or suction air can be applied to the model. The connection to the wind tunnel compressor system occurs through the horizontal holder shown in Figure 2-11.

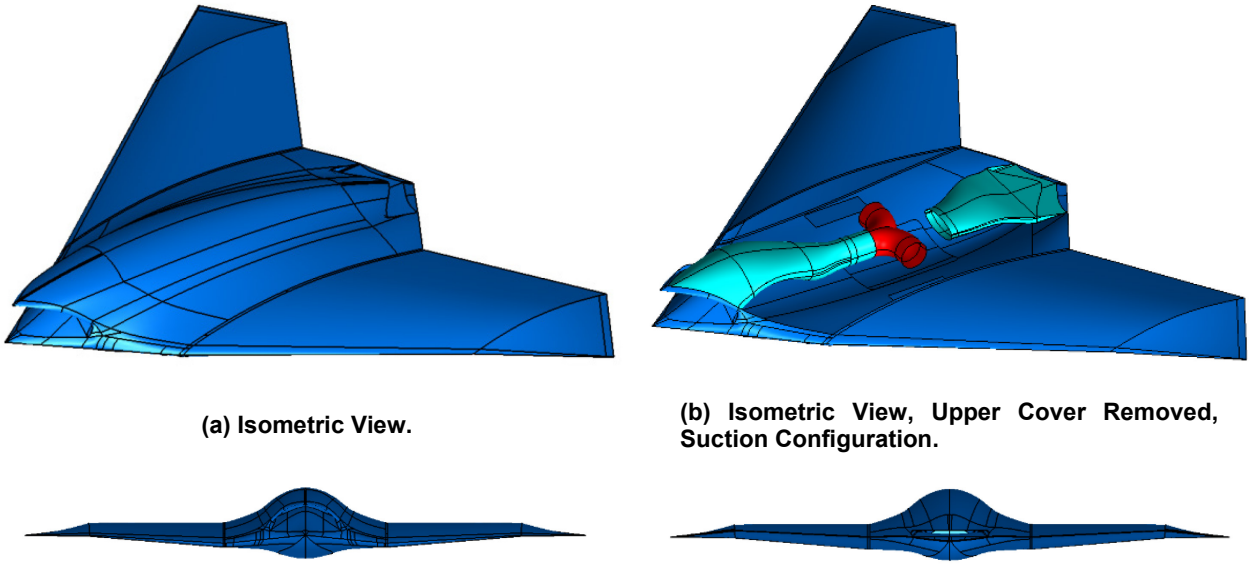

**(a) Isometric View.**

**(b) Isometric View, Upper Cover Removed, Suction Configuration.**

**(c) Front View (Intake Duct).**

**(d) Back View (Nozzle).**

**Figure 2-1: DLR-F24 MULDICON UCAV Model Views.**

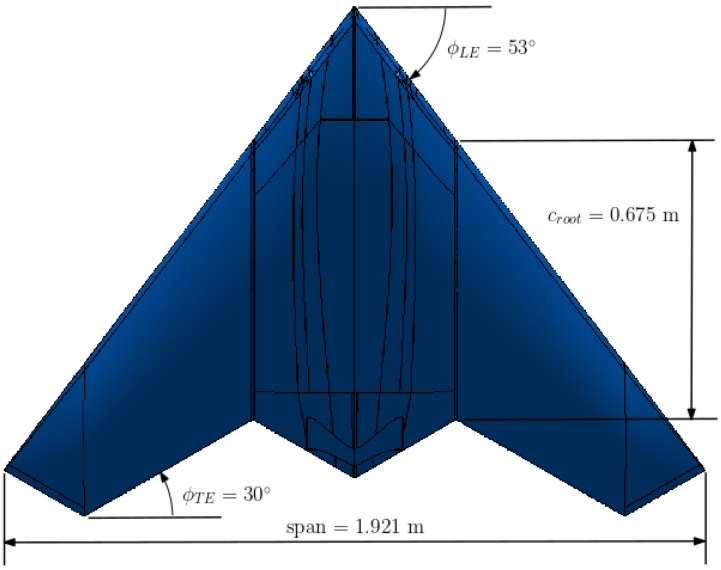


**Figure 2-2: DLR-F24 MULDICON Planform Geometry.**

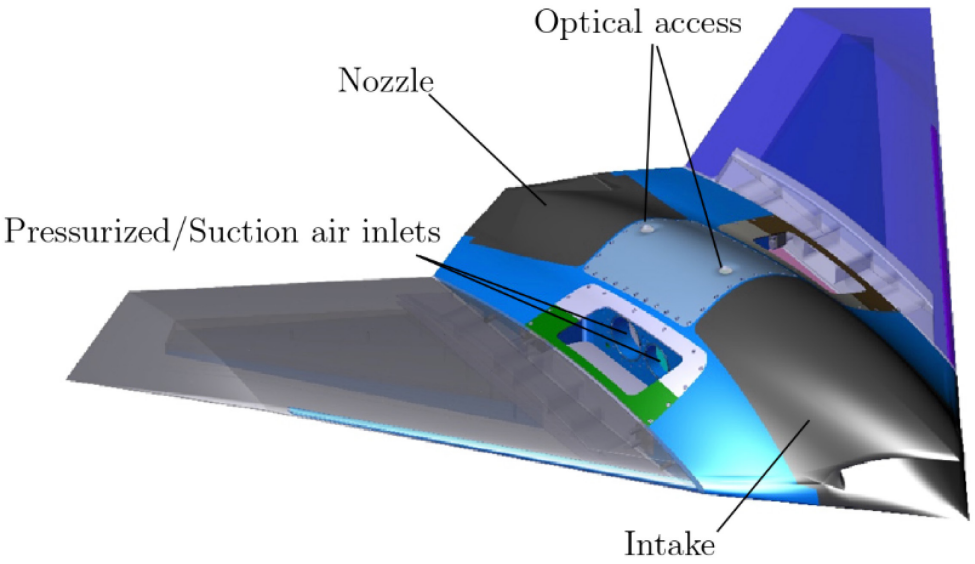


**Figure 2-3: DLR-F24 Modular Design. View of optical access ports and pressurized air inlets.**

Different perspectives on the model are given in Figure 2-1. In particular, Figure 2-1(b) gives an isometric view of the model with its upper part removed to reveal details of the internal connections of the intake duct to the pressurized air system, e.g., shown in red. The decision to split the intake duct inside the model center chamber is an attempt to keep the duct velocities near the model's outlet to the compressor system as low as possible and thus keep any spurious source of noise as low as possible.

Detailed views of the model's internal chamber in the jet mode and suction mode configurations are presented in Figure 2-4. The direction of airflow in these configurations is indicated by the arrows. In the jet mode configuration, e.g., Figure 2-4(a), the horizontal holders provide pressurized air through the upstream most opening in the chamber side walls, e.g., Figure 2-3. The flow of compressed air is first forced through porous aluminum sound absorber where most of the upstream spurious noise is dampened. A flow straightener installed in the center of the chamber helps in uniformizing the flow before reaching the nozzle. The nozzle itself has an elliptical cross-section at the interface with the center chamber which evolves to a rectangular cross-section towards the exit plane. The exit plane cross-section has a width of 266 mm and a height of 20 mm corresponding to an aspect ratio of 13.3, e.g., Figure 2-4. In the suction mode configuration, e.g., Figure 2-4(b), suction is applied through the horizontal holder at the rear most opening in the chamber side walls, e.g., Figure 2-3. The rear part of the intake duct, before the splitter, is designed to have a constant cross-section of 76 mm in diameter. It is equipped with an optical access port to allow the use of a laser-based sound source to trigger propagating acoustic duct modes inside of the intake. Details about the laser sound source technique have been published elsewhere and can be found in references [4], [5], [6]. This arrangement enabled the investigation of the effect of the intake flow on the propagation of acoustic duct modes. A cross-cut view through the model center is shown in Figure 2-5, making visible the arrangement of all components and the detailed contours of the intake duct and nozzle. The section area distribution of the intake duct and nozzle are given in Figure 2-6. Both ducts have converging cross-sectional areas.

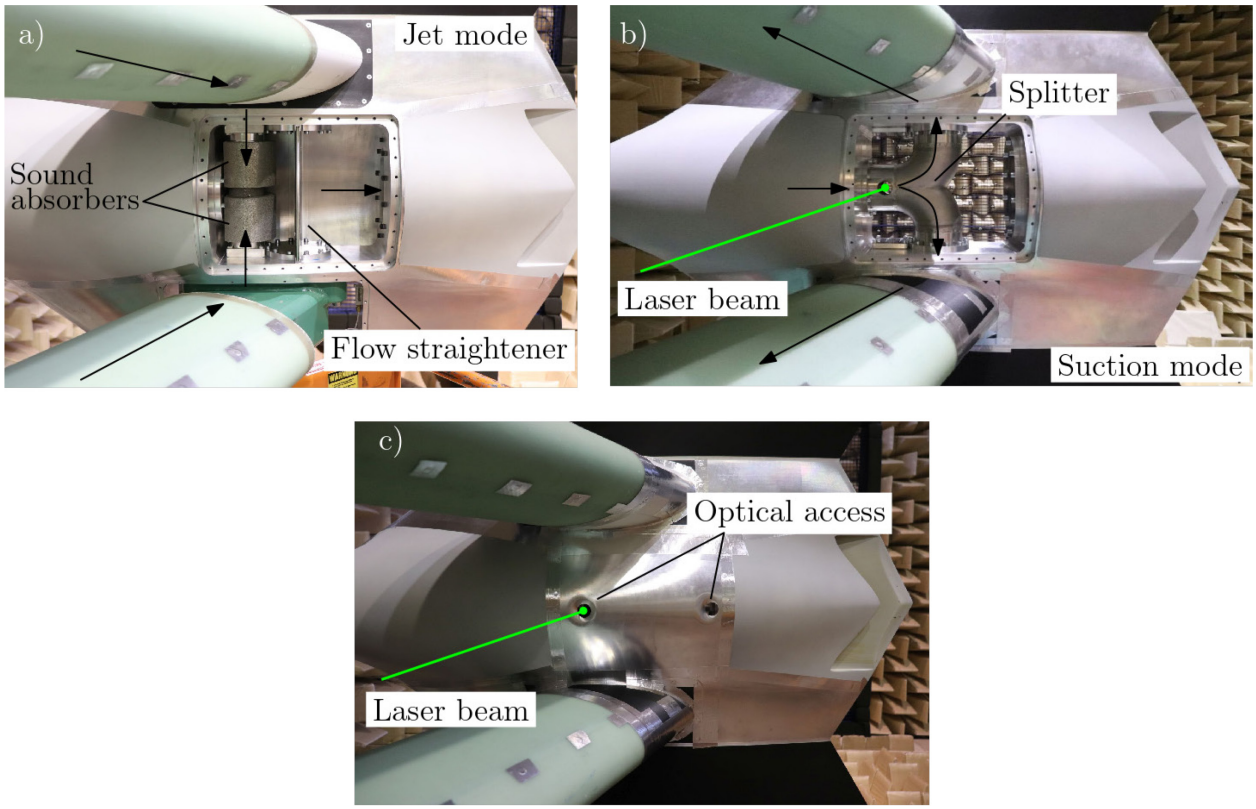


**Figure 2-4: View of the Model's Plenum in a) Jet Mode Configuration, b) Suction Mode Configuration and c) with its Upper Cover Installed. In a) and b) the arrows indicated the directions of the internal stream of air.**

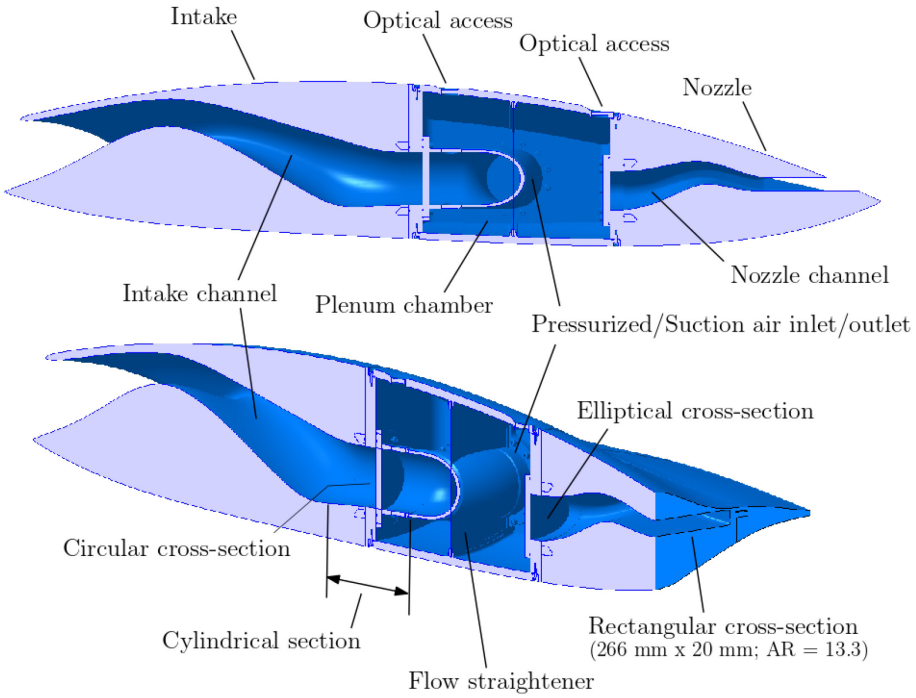


**Figure 2-5: CAD Details of the Intake, Nozzle and Plenum Geometries with the Splitter Junction and Flow Straightener Installed.**

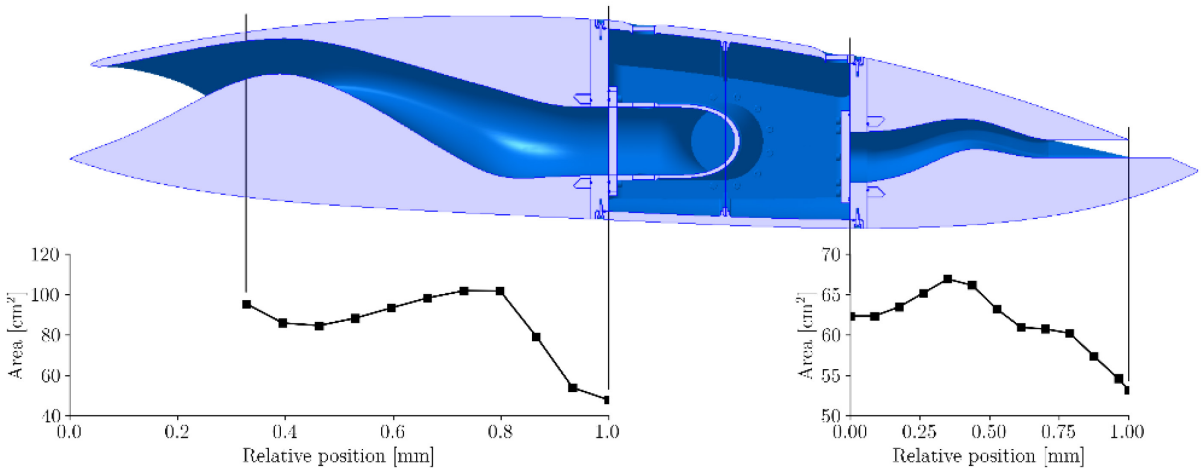


**Figure 2-6: Intake and Nozzle Ducts Section Area Distribution.**

## 2.2 WIND TUNNEL FACILITIES

### 2.2.1 NASA QFF and NACA 0012 Experimental Approach

Florence Hutcheson, NASA

The NASA experimental effort was conducted in the Quiet Flow Facility (QFF) of the NASA Langley Research Center in Hampton, Virginia. The QFF is specifically designed for aeroacoustics testing. The test chamber is equipped with a 0.61 by 0.91 m rectangular open-jet nozzle. Side plates attached to the 0.61 m sides of the nozzle are used to support models above the nozzle, while the 0.91 m sides of the test section remain open. The flow circuit employs baffles, turbulence screens and turning vanes to ensure a quiet, low-turbulence air flow from the open jet. Flow speeds up to a Mach number of 0.17 can be obtained. The anechoic room (7.3 m wide by 9.2 m long by 6.1 m high) is lined with wedges, 91.5 cm deep, to provide an essentially echo-free environment for acoustic measurements down to about 70 Hz. The room is also constructed with a 91.5 cm air space between double walls and is mounted on springs to isolate it structurally from the remainder of the building and thus minimize the transmission of structure-borne noise arising from other parts of the building.

The test setup, shown in Figure 2-7, was similar to that used for AVT-233. A NACA 0012 airfoil of 0.91 m span and 0.2 m chord was positioned at the center of the test section and was supported vertically above the nozzle by the two test section side walls. A 1/8” (0.3175 cm) 4138 Brüel & Kjær microphone equipped with a GRAS RA0173 nose cone was used to acquire the acoustic measurements inside the test section at different streamwise stations. The microphone was mounted on a linear traverse attached to the two test section side walls.

The sound source was a laser-induced plasma which, once formed, rapidly expands to generate a nearly omnidirectional pressure wave that propagates as an isentropic acoustic wave in the far field. The localized plasma was generated by a high-energy, focused laser beam. The laser system used was a Nd:YAG, Gemini PIV laser, with a pulse energy of 120 mJ, a wavelength of 532 nm and a pulse width of 3 to 5 ns. As depicted in Figure 2-8, the laser system was positioned behind one of the test section walls (which was modified to incorporate a 0.95 cm thick tempered glass window). A set of 7.62 cm diameter achromatic, expansion, collimating, and focusing lenses was used to focus the laser beam at the test section midspan.

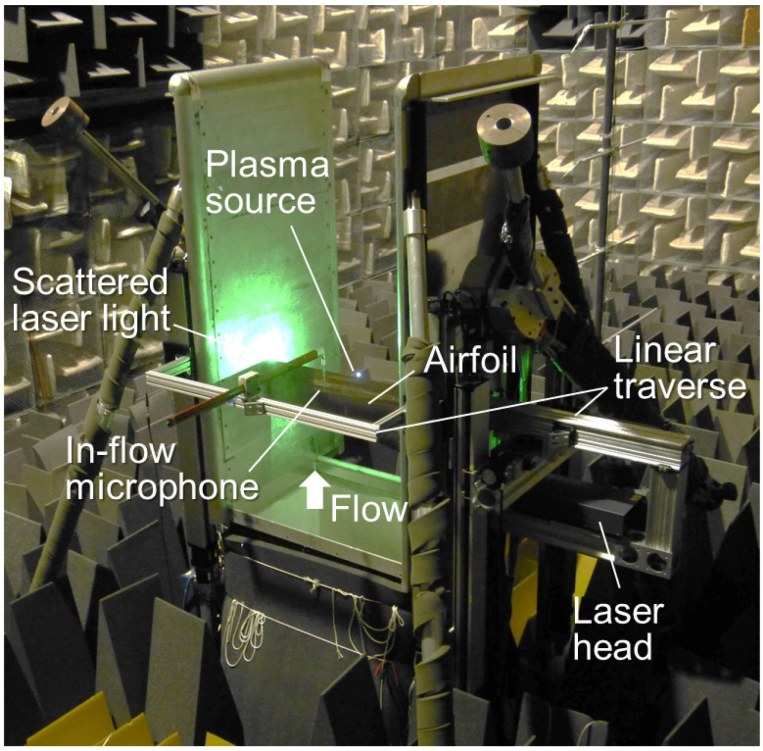


**Figure 2-7: NASA QFF Experimental Setup [Source: NASA].**

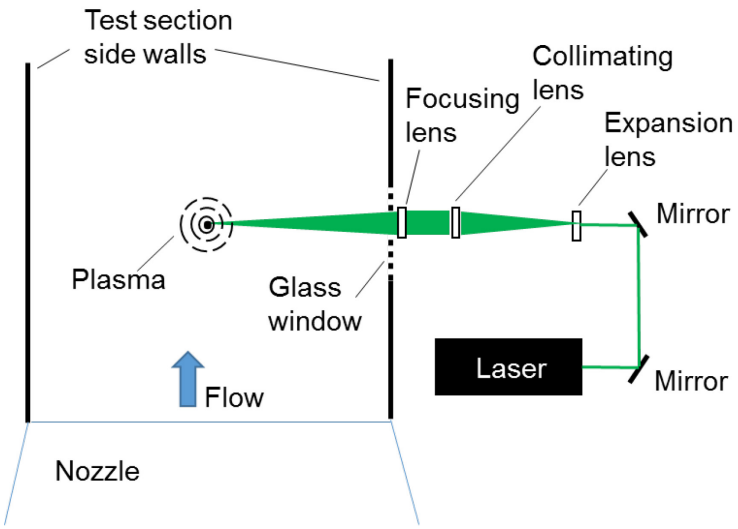


**Figure 2-8: Sketch of Laser and Optical Lens Setup.**

To minimize laser reflections, the path of the laser beam from the laser head to the test section wall window was enclosed by installing tubes between optical lenses, and between the focusing lens and the test section wall window (see Figure 2-9). A photodetector was also positioned near the laser window to record the plasma (sound source) occurrence time.

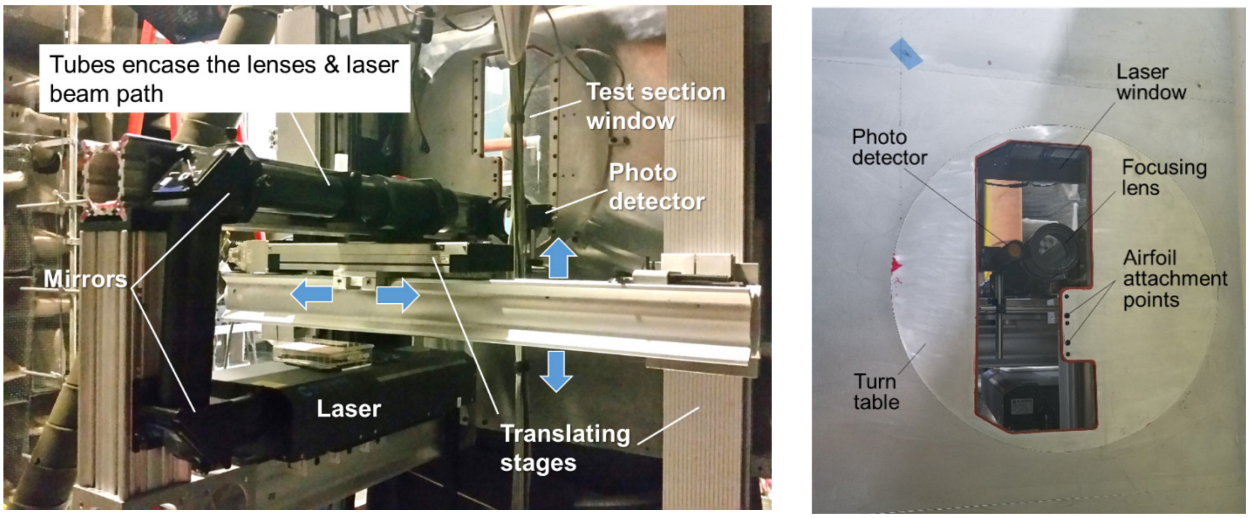


(a) (b)

**Figure 2-9: Laser and Optical Lens Assembly; (a) View from Behind the Test Section Wall; (b) View from Inside the Test Section [Source: NASA].**

The traverse system used to position the in-flow microphone and the laser/optic assembly is shown in Figure 2-10. It was designed to be compact and rigid in order to minimize flow-induced vibrations. It was used to traverse the in-flow survey microphone in the streamwise direction, and the laser system assembly in both streamwise and crosswise directions to position the sound source at chosen locations.

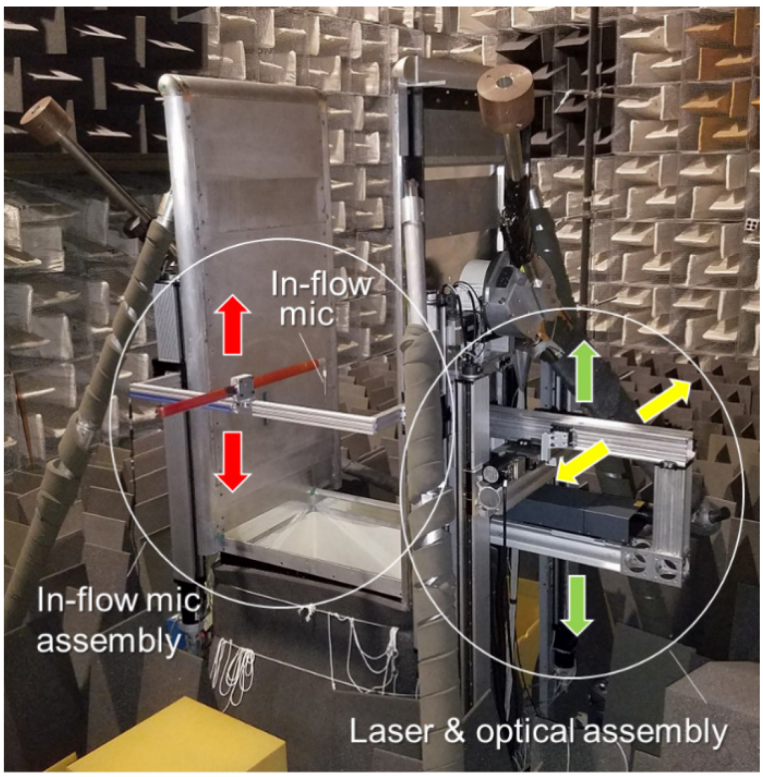


**Figure 2-10: Traverse Assembly for the In-Flow Microphone and Laser System [Source: NASA].**

### 2.2.2 DNW-NWB Test Environment

Karl-Stéphane Rossignol and Jan Delfs, DLR, GERMANY

The DLR-F24 MULDICON model was specifically designed for use in the anechoic test section of the DNW-NWB low-speed anechoic wind tunnel. The DNW-NWB has nozzle surface of 3.25 m x 2.8 m and a test section length of 6 m. Its acoustic plenum has dimensions 14 m x 16 m x 8 m (length x width x height) and is certified for a frequency range of 100 Hz to 40 kHz in accordance with Appendix A of ISO 3745. The wind tunnel, in the open jet configuration, can be operated at free-stream velocities up to 80 m/s. Pressurized air or suction air can be supplied to the model through the tunnel's own compressors system.

An overview of the complete experimental setup in the test section of the DNW-NWB is provided in Figure 2-11. This figure includes the in-flow microphone setup, the laser tower and the model's support rig. The support rig consists of an oversized L-shaped construction where the two elliptically-shaped horizontal model holders attach. The horizontal holders connect to the pressurized air circuit through pipes mounted to the back side of the rig. The stable construction of the rig was necessary to ensure repeatable positioning of the laser sound source inside the intake duct. The model is mounted vertically in the test section. This allows for free space on the model's lower side where acoustic field is to be acquired. At the same time, it provides a certain amount of shielding from spurious sources of noise on the upper side, e.g., flow noise through interaction with the horizontal holders. The L-rig is mounted directly onto DNW-NWB turntable, making small adjustment in angle of attack possible; although the model was not designed to withstand wing loads occurring above an angle of attack of 5°. The horizontal holders were designed with an elliptic contour to help limit their effect on the free-stream; although their influence on the flow in the close proximity of the model's upper surface is clearly apparent from flow visualizations made in the course of the experiments.

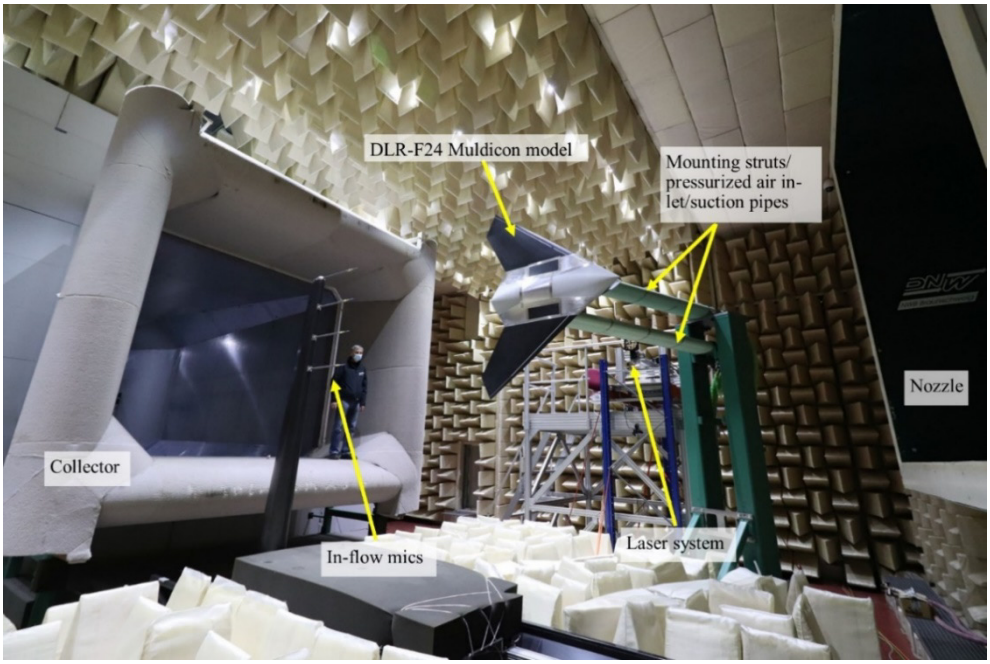


**Figure 2-11: DLR-F24 MULDICON Test Bed in the Open-Jet Acoustic Test Section of DNW-NWB. The flow direction is from right to left.**

This design choice constitutes a compromise allowing a very stable model fixation through the rig's stiffness while promoting lower flow velocities in the pressurized pipe system prior to reaching the model. Moreover, the horizontal holders are tilted by 15° in the upstream direction to reduce the influence of the tunnel

shear-layers on the structure and keep the holder length as short as possible. This rotation also effectively reduces the chordwise velocity near the holder's trailing edge and thus, also reducing trailing noise radiation.

The acoustic emissions of the model in its various configurations are acquired by a set of four in-flow microphones mounted to a linear displacement system. When using the laser sound source, four 1/8" GRAS 40 DP microphones are used. Otherwise, four ¼" GRAS 46BF-1 free-field microphone provided by NWB were used. NWB's 160 microphone phased array mounted to a second linear traversing stage, is used as a complementary measurement technique; primarily for source identification. Specific details regarding the microphone setup and measurement range are provided in Figure 2-12 and Figure 2-13.

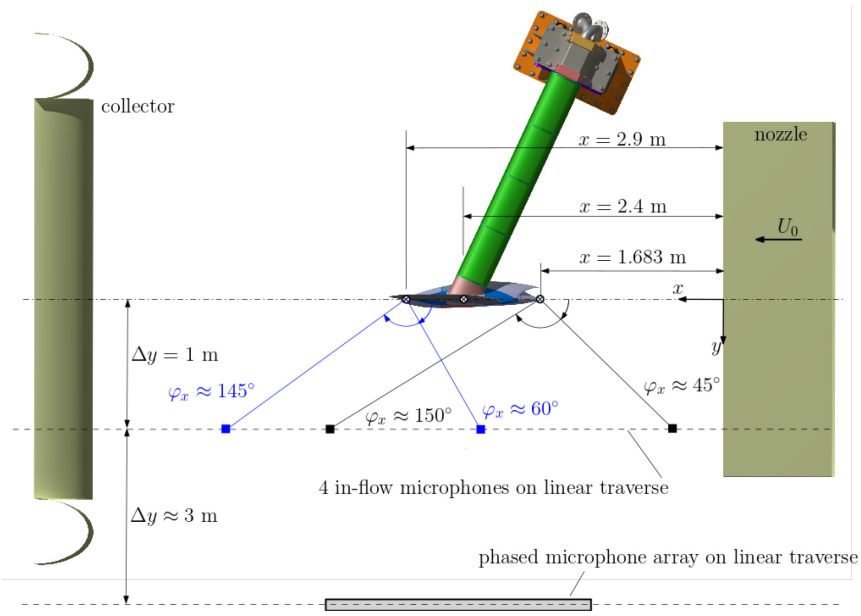


**Figure 2-12: Experimental Setup in NWB. The range indicated in black and blue correspond to the in-flow measurements ranges for the intake acoustic and jet acoustic, respectively.**

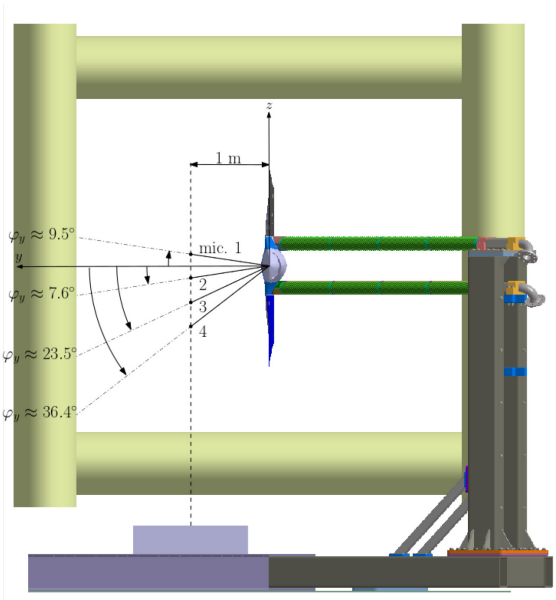


**Figure 2-13: Experimental Setup. Spatial range of the in-flow measurements indicated in blue.**

### 2.2.3 CIRA Test Environment

Fabrizio De Gregorio and Carmello Izzo, CIRA

The wind tunnel test carried out at DNW-NWB wind tunnel suggested to investigate the nozzle flow characteristics, in particular the jet turbulent level for the different test conditions. The F24 MULDICON nozzle will be investigated at CIRA laboratories. The nozzle will be fed by the pressurized air of the CIRA transonic wind tunnel PT-1. The PT-1 air flow system provides a mass flow up to 26 kg/s at a static pressure of 36 bar.

The MULDICON nozzle will be installed inside the PT-1 building characterized by the following dimensions: 18 × 15 × 10 m (L × D × H). The nozzle will be installed at a distance of about 12 meters from the main gate in order to reduce possible recirculation effects. If necessary, the gate will be open, and the jet will discharge outside to minimize wall effect. Figure 2-14 shows the planimetry of the transonic wind tunnel building with the position of the test case.

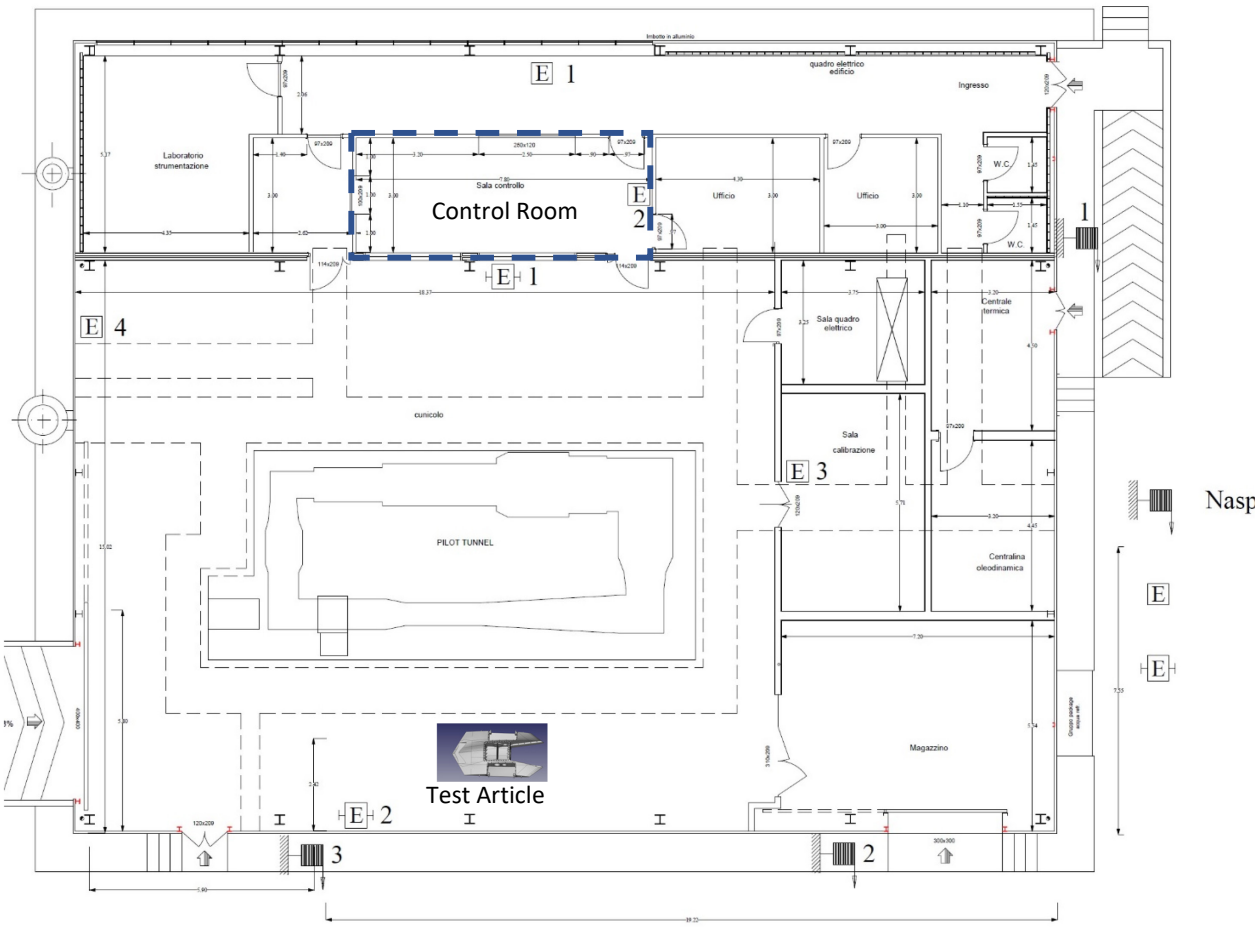


**Figure 2-14: Transonic Wind Tunnel Planimetry.**

The main nozzle flow characteristics will be measured on different longitudinal planes by 2C-PIV measurements as shown in Figure 2-15. The PIV system is composed of a pulsed Nd-Yag laser, model CFR400 manufactured by Big Sky Laser, characterized by a repetition frequency of 10 Hz and a maximum energy value of 200 mJ at wave length of 532 nm.

**Figure 2-15: PIV Measurement Planes.**

A system of two sCMOS cameras will be installed consisting of two ILA.PIV.sCMOS CLHS (25 frame rate, 2560 × 2160 pixels, 16-bit, pixel dimension 6.3 μm). The cameras can be equipped with Canon EOS lens with 60 or 200 mm focal length respectively and remotely controlled. For stereo measurements, motorized Scheimpflug systems are available. A special seeding generator operating up to 5 bar is available for high-speed flows [7].

One Hot Wire (HW) anemometer system is available for velocity fluctuation measurements. A measurement point will be considered inside the nozzle. The HW system is composed of an IFA 300 Constant Temperature Anemometer System from TSI with four channels.

In order to monitor the pressure distribution inside the nozzle and control eventual flow separation, the static pressure inside the nozzle will be measured by the pressure system PSI 8400 available on the PT-1 wind tunnel. Several electronic pressure scanners are available:

- ESP 32 ports at 30 psid (206842.7 Pa);
- ESP 32 + 16 ports at 15 psid (103421.4 Pa);
- ESP 64 ports at 5 psid (34473.79 Pa);
- ESP32+16 ports at 2.5 psid (17236.89 Pa);
- ESP 64 ports at 1 psid (6894.757 Pa).

Although the building is not acoustically treated, some acoustic measurements will be performed. The acoustic system is composed of:

- Two, 1/4” 4135 B&K microphones and five, 1/4” 4939 B&K microphones. Both are fitted with a preamplifier and connected to a B&K Nexus 2690 signal conditioner. The frequency response of both types of microphones is flat up to 100 kHz and their full-scale value is 162 dB.
- Eight 1/4” Microtech Gefell M360 microphones, whose frequency response is flat in the range 20 – 20 kHz and whose full-scale value is 138 dB.

# Chapter 3 – TOOL ADJUSTMENT

**Yueping Guo and Russell Thomas**
NASA
UNITED STATES

**Patrick Zimmermann**
Airbus Defence and Space
GERMANY

**Mathieu Lorteau**
ONERA
FRANCE

**Mattias John Quas, Shia-Hui Peng and Samuel Gottfarb Bart**
FOI
SWEDEN

## 3.1 ACOUSTIC SIMULATION METHODOLOGIES

### 3.1.1 NASA Scattering Prediction Methodology

Yueping Guo and Russell Thomas, NASA

For over two decades there have been sustained efforts in NASA Aeronautics research to develop prediction approaches for the aeroacoustic effects resulting from propulsion airframe integration, or PAA effects. This has been for at least three general reasons: the pursuit of more accurate, higher fidelity aircraft system-level predictions [8], [9], as a new avenue to innovate noise reduction technology [10], [11], and as an integral and necessary element with which to achieve ambitious noise reduction goals with unconventional aircraft concepts [12]-[18].

For the wide range of applications at NASA, from advanced conceptual aircraft studies to the development of noise reduction technologies or operational procedures for modern aircraft, it remains generally the case that system-level methods and mid-fidelity computational methods continue to be the most practical and capable of meeting cycle turnaround time requirements. For many studies, results are needed long before the high-quality geometry needed for CAA methods is even available. In addition, for project planning and technical formulation, the aircraft system-level methods provide the best insight, at the earliest stages, into the prioritization of noise sources and interactions, Ref. [19] for example.

Given the value of predicting PAA effects, noise shielding for example, several approaches have been investigated with the objective to provide a more capable method compared to the existing method in NASA's Aircraft Noise Prediction Program, ANOPP [20], that is based on semi-infinite barrier theory with an empirical approximation, the WING method. While the WING method in ANOPP is relatively easy to use and can be used for both shielding and reflection, it is basic in both physics and geometry capabilities. For NASA's PAA and Aircraft System Noise research and for use with ANOPP, a completely new method has been developed from first principles with grounding in the practical execution of aircraft system noise problems. This all-new method starts with classical geometric acoustics theory. However, for more accurate and robust practical aircraft applications, there are several modifications and extensions in analytical formulations that have been added to the classical theory together with the numerical implementation. This results in a completely new code capable of shielding, diffraction, and reflection prediction, the Propulsion Airframe Aeroacoustic Scattering or PAASc code. Using only a subset of the PAASc method just for diffraction and shielding prediction, a second code can be used, the Propulsion Airframe Aeroacoustic Shielding Attenuation or PAAShA code.

In two previous papers [21], [22], the theoretical formulation of the PAASc method has been briefly described. In addition, systematic validation has been presented to demonstrate the applicability, accuracy, and robustness of the method using a wide range of analytical solutions, experiments with canonical

geometries [23], experiments of point source scattering by a symmetrical airfoil [24], broadband scattering from a complex aircraft model [25], and scattering from a full-scale aircraft flight test [26]. For a wide range of aircraft system noise studies and optimization, the method is sufficiently fast in both computation time and total cycle time for problem setup and processing. For example, for a prediction of scattering from a full-scale Boeing 787-10 aircraft geometry, the computation time for all frequencies is in the order of minutes on a standard desktop personal computer.

Geometric acoustics has been researched extensively in the past and has been applied in various areas in acoustics [27]-[35]. The basic principles of the theory and its limitations and favorable features are well documented and discussed. The main limitation is its high frequency asymptotic formulation, limiting its applications to cases where the acoustic wavelength is smaller than the characteristic length scale of the scattering geometry. Despite this limitation, geometric acoustics remains an attractive method in practical applications because of its favorable features, which include its intuitive formulation of rays and ray tubes that closely mimic the physical propagation of sound waves, its ability to accommodate complex surface geometries, and its high computational efficiency. The last is still a critical requirement for practical aircraft noise applications even with the drastic improvements of computing power of modern computers in recent years; it is orders of magnitude more efficient than any other numerical methods, such as the volume discretization method of Computational Aeroacoustics (CAA) and the surface discretization method of Boundary Element Method (BEM), and it is the only method feasible for quick turnaround engineering applications of full configuration aircraft for the most important frequencies in the kilohertz range. Because of this, geometric acoustics has attracted attention in recent years for aircraft noise applications [36]-[41]. A key to the effective use of geometric acoustics in aircraft noise scattering, however, is not a simple matter of straightforward application. Rather, the basic theories need to be modified and extended to account for the unique features of complex aircraft noise sources, effects, and geometric features.

Aircraft applications involve the complex geometry of curved surfaces. In addition, the surfaces are sometimes treated with acoustic liners for noise reduction and the geometry is embedded in nonuniform flows. These features are essential and can affect the reflection of acoustic waves, and thus, affect the noise scattered by the aircraft. For the PAASc method, a general formulation of the reflection coefficient was derived by asymptotic analysis and includes all these effects in closed form analytical formulas to allow for efficient numerical implementation [21].

The smooth geometry and the sharp wedge diffraction implemented in PAASc uses the classical theories [42]-[49], with the surface creeping wave generation and radiation for smooth geometry and the wedge diffraction for abrupt geometry. The concepts are physically intuitive, and the theories are well developed for canonical geometries. In adapting the theories for aircraft noise, use was made of the fact that the scattering geometry contains elongated elements, such as the wing leading and trailing edges and the fuselage, characterized by approximately invariant cross sections over a range of many wavelengths in the length direction. Thus, the smooth geometry diffraction can be formulated for long cylindrical surfaces of irregular cross sections by application of the classical diffraction theory. Furthermore, a method was implemented to efficiently compute the properties of the helical waves on the diffraction surfaces, including the path of the surface wave propagation, the phase changes of the waves along the propagation path, and the amplitude decay of the surface waves, which control the diffracted sound.

For sharp geometry diffraction in PAASc, the analytical solutions for semi-infinite wedges were adapted as the starting point for trailing edge diffraction. The basic theory for the canonical geometry is in analytical form and was cast in a format consistent with ray tracing. However, corrections were added to account for the effects of finite dimensions of the aircraft geometry. This was done by approximate models, derived from simple considerations of the scattering configurations. The approximate models are acceptable for engineering applications because the finite-dimension effects are of second order under the framework of geometric acoustics, where the dimensions of the scattering surfaces are larger than the acoustic wavelength. Comparisons between the asymptotic results, the analytical solutions, and the

Kirchhoff approximation [40]-[43] have been shown [22] for the simple canonical problem of sound diffraction by a semi-infinite plate, demonstrating the accuracy of the asymptotic results and the shortfall of the Kirchhoff method.

Many aircraft noise sources are only partially coherent. This poses a challenge for numerical methods such as CAA and BEM, because the computation of such methods gives the total acoustic pressure at the measurement locations without information on how the sound propagates from its sources to the measurement locations, and thus, the results always imply perfectly coherent sources when the pressures are squared to construct the noise spectra. Since geometric acoustics follows individual rays, or propagation paths, source coherence can be naturally accounted for because the differences in ray path lengths represent different source times of the ray contributions. The source coherence effects can then be calculated by the differences in ray path lengths when the ray contributions are summed at the measurement locations. The formulation of the coherence effects under the framework of geometric acoustics is analytical, but empirical models will be introduced to characterize the constructive and destructive interferences of various ray contributions. Examples have been shown [21] to illustrate the importance of source coherence modeling including comparisons with wind tunnel data.

Overall, the method developed and implemented in the NASA PAASc code has demonstrated excellent validation results. For reflection, some examples have been reported to illustrate the accuracy, and, more importantly, to demonstrate the effects of key features. These have included the importance of curved surface reflection in comparison with analytical solutions and if the approximation of panel reflection used. While the agreement between the analytical solutions and the formulation for curved surface reflection is very good, it has been shown that the panel reflection approximation greatly overpredicts the interference between the incident and the reflected waves, leading to large errors. The importance of source coherence in sound scattering calculations has been demonstrated with comparisons between the coherent and the incoherent calculations, together with comparisons with wind tunnel test data.

A systematic validation of the diffraction and shielding methodology in PAASc (and PAAShA) has been reported [22] for progressively more complex problems and experiments that are representative of aircraft-like applications. The effects of second-order corrections in the transition region between insonified and shadow zones have been shown to be needed to render the results continuous. The errors in the diffraction by smooth geometry in shadow zones due to the use of the approximate method of the Taylor transformation to account for mean flows have been discussed. For sharp geometry diffraction, the advantage of the wedge diffraction formulation over the method of Kirchhoff integration has been demonstrated and discussions have been given for the cause of the large errors in the latter method. Comparisons have been reported for geometries of increasing complexity and for a variety of sources from multiple experiments and facilities. In some cases, comparison was made with analytical solutions. Over this wide range of problems, geometries, and sources, the method was proven to be robust and efficient. Accuracy is typically 1-4 dB (and often on the lower end of this range) over a wide range of the most significant frequencies and polar and azimuthal angles. Accuracy can also be somewhat diminished for high azimuthal angles, often of less relevance. This measure of accuracy, 1-4 dB determined by comparing to experimental data, must also consider that for all the experiments used in the study, there are reasonable issues of experimental uncertainty, particularly at high frequencies, high angles, and with the source characteristics.

As expected, there are many requirements needed to obtain an accurate prediction. Perhaps the most difficult, in general for aircraft applications, will be having the accurate characteristics, such as polar and azimuthal directivity of the noise source.

Overall, the method has clearly met the need for scattering prediction for aircraft application studies with the NASA aircraft system noise code, ANOPP, as executed within the ANOPP2 framework. The PAASc code is a mid-fidelity method with overall excellent accuracy. In the context of aircraft system noise studies, it is sufficiently fast in both computation time and total cycle time for problem set up and processing. The code

also provides the additional necessary capability to predict reasonably well for a wide range of azimuthal angles, which is key for realistic three-dimensional aircraft geometry shielding and the directivities that impact ground noise contours.

Of course, PAASc can also be used as a stand-alone method and overall is well suited for the objective of the task of NATO AVT-318, development of a noise reduction design for a military-type vehicle with the propulsion noise sources on the top side of the vehicle. For this application, it is a promising noise reduction approach to focus on the aft-radiated noise from the fan and jet noise sources. The Shielding Flap concept will be described in Chapter 4, experimental results from the NASA QFF will be shown in Section 5.2 and, finally, comparisons between prediction and data will be presented in Section 6.1.

### 3.1.2 Airbus's Methodology

Patrick Zimmermann, Airbus Defence and Space

The numerical investigations conducted by Airbus Defence and Space comprise intake noise and jet noise calculations of the NATO blended wing body configuration referenced as DLR-F24 MULDICON UCAV. The numerical tools for acoustic simulation are chosen in accordance with the application.

1) **Intake noise**

The intake noise propagation is calculated in the time domain with the Discontinuous Galerkin (DG) code DISCO++ developed by DLR [50], [51]. The tool chain is outlined in Figure 3-1. The linear Acoustic Perturbation Equations (APE) are solved on three-dimensional tetrahedral grids by a quadrature-free DG method. The explicit fourth-order Runge-Kutta scheme is used for time integration. The laser-based sound source from the measurements by DLR is modeled with a monopole. The acoustic waves are extrapolated to the far field according to the Ffowcs-Williams Hawkings method (FW-H). The flow field around and inside of the intake is considered by interpolating a RANS mean flow field.

The acoustic domain includes the MULDICON intake with a spherical boundary. Slip wall boundary conditions are assigned to the intake surfaces setting the wall-normal fluctuations to zero. The position of the monopole sound source is taken from the wind tunnel measurements by DLR and lies in the center of the circular duct section. As only the intake geometry is considered in the CAA domain scattering effects around the vehicle are not investigated. The mesh cell size is chosen to resolve a maximum frequency of 10 kHz. The captured time signals of the acoustic pressure fluctuations are postprocessed using Fast Fourier Transform (FFT).

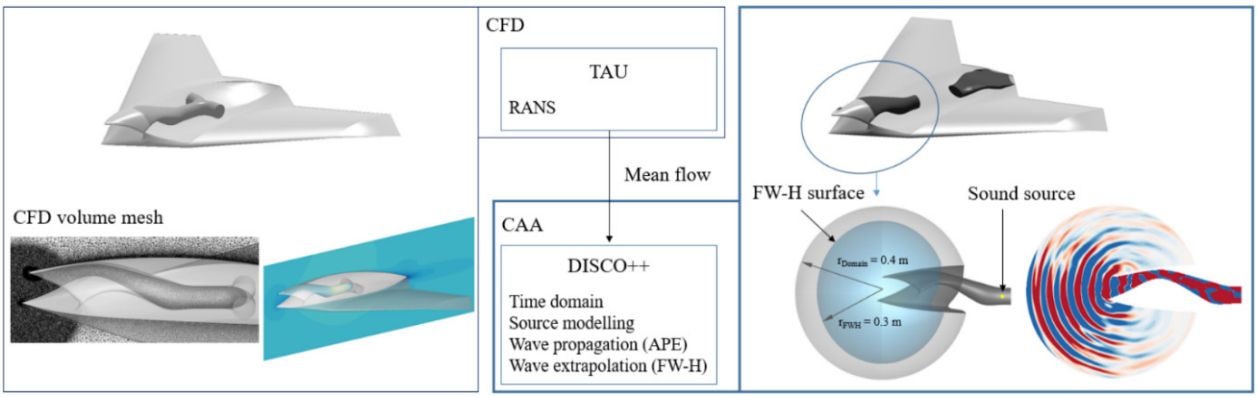


**Figure 3-1: Numerical Tools for Intake Noise Calculation.**

The numerical source model can be traced back to previous studies with similar setups [5], [52]. The mechanism of the laser-based source is described by the formation and expansion of plasma due to the energy input generating a pear-shaped pressure wave. After forming an idealized sphere of approximately 10 mm radius the pressure front propagates as an isentropic acoustic wave. The source shows monopole-like characteristics with an approximately uniform directivity and broadband behavior.

The numerical monopole source is referred to a heat source specified by a pressure impulse. The spatial distribution is approximated by a Gaussian function. The temporal behavior is modeled by a Gaussian function defined by a peak time, half width and amplitude.

2) **Jet noise**

The jet noise calculations by Airbus D&S are performed by using the solver ProLB based on the Lattice Boltzmann method. A Hybrid Recursive Regularized (HRR) collision model is implemented with a D3Q19 lattice scheme [53]. Immersed boundary conditions allow complex geometries with Cartesian meshes. The MULDICON configuration is simulated in freestream conditions. Near the vehicle surfaces a wall model based on a Reichard log-law is applied. A velocity boundary condition is set at the elliptical exhaust zone inside of the exhaust duct. Towards the exhaust exit the nozzle describes a rectangular cross section with V-shaped upper and lower trailing edges, see Figure 3-2. An extension plate is installed at the lower nozzle exit. The intake is closed for the jet simulations. The jet noise simulations are performed in athermal conditions. A co-flow velocity is defined according to the corresponding wind tunnel measurement by DLR. The pressure fluctuations are captured at microphones corresponding to the wind tunnel positions by DLR.

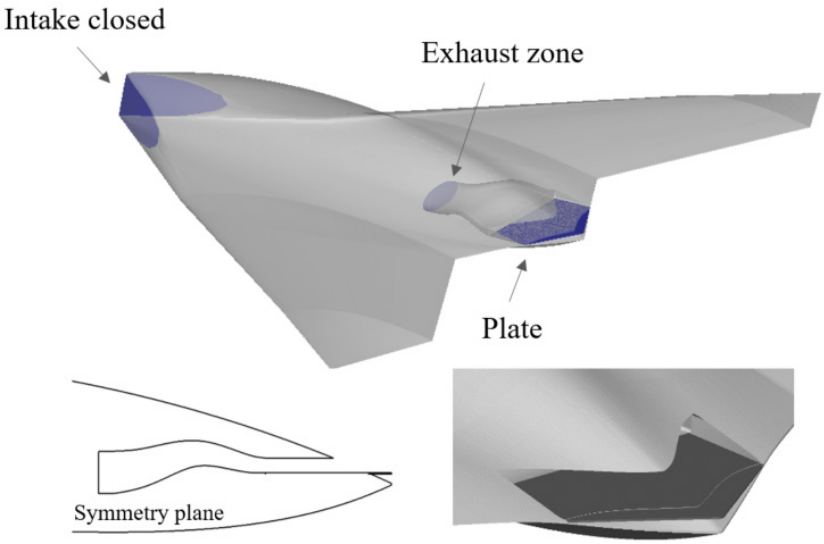


**Figure 3-2: MULDICON Model for Jet Noise Calculations.**

### 3.1.3 ONERA's Methodology

Mathieu Lorteau, ONERA

The CAA calculations are conducted with ONERA's sAbrinA structured CAA solver [54], [55], [56], [57], [58] that solves either the full or the linear Euler's equations, in a conservative and perturbed form. The sAbrinA solver employs high-order, finite difference operators, involving 6th-order spatial derivatives and 10th-order filters, as well as a 3rd-order compact Runge-Kutta explicit time-marching scheme. More detailed information about the sAbrinA solver and its underlying methodology can be found in Refs. [59], [60].

In the CAA computations, the geometry of interest is taken into account with the IBM (Immersed Boundary Method) approach, which thus greatly simplifies the CAA mesh design process for such geometry. The mesh consists of a single 3D Cartesian grid. A refined mesh zone was defined around the nacelle by setting a maximum mesh size chosen to accurately resolve the acoustic waves. Outside of the refined mesh zone, a grid stretching is applied with a geometrical ratio equal to r = 1.05 in all three directions to increase by a factor 20 the refined grid size to the exit boundary conditions. The maximum cell size inside the refined mesh zone was calibrated from the target frequency 5 kHz. 27 points per acoustic wavelength are considered for the latter frequency in the upstream and downstream directions, the source injection plane being the reference. The mesh size $\Delta x$, associated to the apparent wavelength due to the convection effects, is then $\Delta x = \lambda.(1 \pm M\infty)/27$ with $\lambda$ the wavelength at rest and $M\infty$ the Mach number. This gives a total number of points of 103 × 106 for the acoustic mesh. The same mesh has been used for all the CAA computations since the Mach number is at the most $M\infty = 0.24$, for which the mesh resolution is sufficient. Figure 3-3 depicts both the computational domain and a longitudinal cut for the computed configurations.

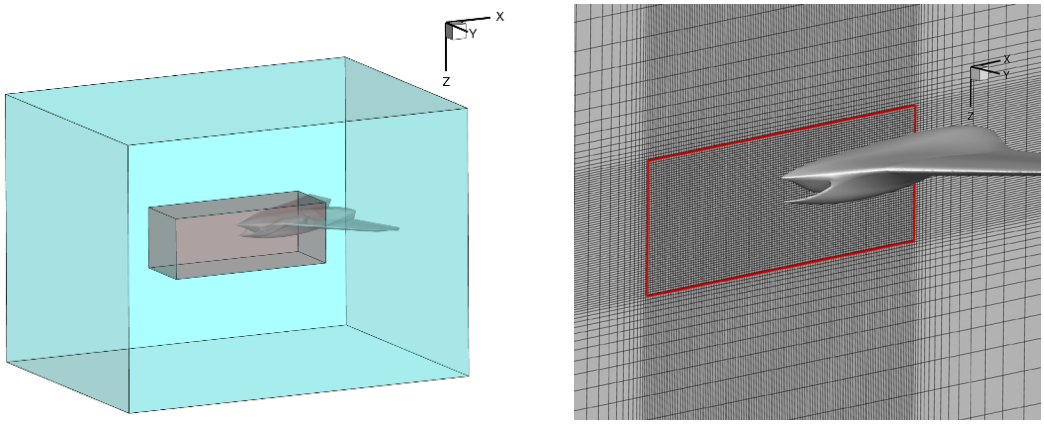


**Figure 3-3: Views of (Left) the CAA Computational Domain and (Right) a Cut of the Mesh in the Geometry Midsection Plane (One in Four Points are Plotted for the Sake of Clarity); with the Refined Mesh Zone Delimited in Red.**

Three configurations have been studied:

1) Without any base flow, i.e., $M\infty = 0$ and a mass flow rate Q = 0;
2) With a base flow at $M\infty = 0$ and a mass flow rate Q = 0.4 kg.s-1 at the inlet; and
3) With a base flow at $M\infty = 0.116$ and a mass flow rate Q = 0.4 kg.s-1 at the inlet.

The base flows have been computed with ONERA's solver Fast and interpolated on the CAA mesh grid for the acoustic computation. See Section 3.2.2 for more details on these base flow computations.

For the three configurations simulated, the same harmonic source at the frequency 5 kHz and with an arbitrary amplitude has been injected as the acoustic source. It is located at (0.58 m; 0; 0.02 m) for the three simulations, which corresponds to the experimental source location.

The time step $\Delta t$ was chosen to get a maximum CFL number of about 0.75. Results and statistics are acquired over 5T once the convergence is reached (where T is the period associated to the frequency of interest) after a numerical transient time of 100T for all simulations. Each acoustic simulation required about 1.5 × 103 CPU hours (on 390 parallel cores). These computational times are rather inexpensive compared to computations with curvilinear and body-fitted meshes thanks to the IBM which enables to maximize the time step and thus to minimize the number of iterations for one period of the source, here: $\Delta t = T/50$. Furthermore, the IBM pre-processing was performed in less than 1% of the overall computational time.

### 3.1.4 FOI's Methodology

Mattias John Quas, Shia-Hui Peng and Samuel Gottfarb Bart, FOI

Aerodynamic flow induced noise is firmly connected to the turbulent flow and the subsequent turbulent coherent structures in their full range of scales. By definition, the time dependence of aeroacoustics cannot be neglected, and the analyses must have a temporal resolution to accommodate both the fluid flow properties, as well as the acoustics frequency range if no model for this is used. Due to this, the computational aeroacoustics analysis of noise generation by turbulent flows and, subsequently, of noise propagation, requires detailed information of turbulent fluctuations and their temporal and spatial correlations.

Based on scale resolving hybrid RANS-LES simulations, see Section 3.2.3, the computational aeroacoustics analyses for the propagated flow induced noise are conducted using so-called acoustic analogies, as first proposed by Lighthill [61]. For the computational aeroacoustics the M-Edge code [62] was used. The implementation in the code is based on the Ffowcs-Williams and Hawkings (FW-H) acoustic analogy [63]. For this implementation of the FW-H analogy, a permeable integral surface enclosing the near field noise generating sources needs to be established. This surface is used to sample relevant flow noise related entities. The location of the integral surface is difficult to determine. In general, it should be positioned close enough to the source flow to avoid significant numerical dissipation of the sampling data, yet far enough away so that all significant noise sources are captured within the enclosed region. For the analyses conducted here, the location of the integral surface is based on information from the vorticity field computed from a steady state RANS computation, performed prior to the scale resolving simulations. For the present analyses, two integral surfaces are created, as seen in Figure 3-4. The position of the inner surface is chosen approximately where the vorticity magnitude is between 10 and 20 based on the steady state RANS simulations. The outer integral surface is located approximately 100 mm outside the inner surface for the purpose of estimating the noise signal decay and the level of artificial (numerical) damping, due to the grid in combination with the differencing schemes.

In the M-Edge implementation of the FW-H analogy the propagated sound pressure for a stationary integral surface is computed considering representation of acoustic sources related to the mass flux, the pressure fluctuations and to the momentum. All terms are evaluated on the integral surface, with local source quantities evaluated at the retarded time $\tau$, where $\tau = t - R/c_0$. In the expression for $\tau$, $R$ is the distance between target and observer at emission time and $c_0$ is the speed of sound in the medium. Similar approaches have been used in other work, see e.g., Refs. [64] and [65], and make it possible to evaluate the propagated flow induced noise at the observer location.

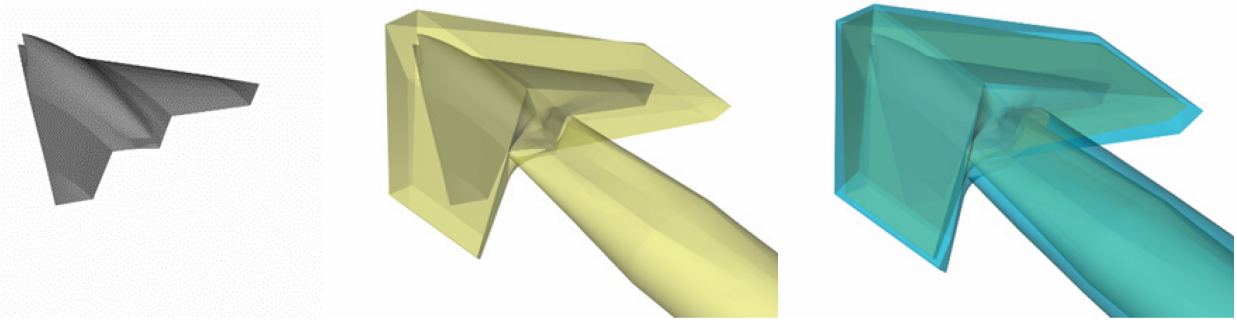

**Figure 3-4: Integral (Transparent) Inner and Outer Surfaces for Acoustics Sampling Shown for the B1 Geometry. Left: The MULDICON geometry. Middle: Inner integral surface enclosing the MULDICON and jet exhaust volume. Right: Outer integral surface.**

## 3.2 FLOW SIMULATION METHODOLOGIES

### 3.2.1 Airbus's Methodology

Patrick Zimmermann, Airbus Defence and Space

The flow simulation methods applied by Airbus Defence and Space can be divided into RANS calculations for the intake noise background flow and calculations based on the Lattice Boltzmann Method (LBM) for jet noise.

The mean flow fields for the intake noise propagation are calculated on an unstructured mesh with DLR's TAU solver using the Reynolds-Averaged Navier-Stokes equations (RANS). As turbulence model the k-ω Menter SST model is used with central flux discretization and scalar dissipation. The mean flow results are subsequently interpolated to the CAA grid. Viscous wall effects are considered for the surfaces of the MULDICON including the intake duct. Mass flow rate boundary conditions are used for the Intake zones. The exhaust of the MULDICON is closed for the intake calculations.

The numerical setup for the jet flow simulations based on the Lattice Boltzmann method is described in Section 3.1.2.

### 3.2.2 ONERA's Methodology

Mathieu Lorteau, ONERA

Two mean flow fields have been computed: one for the ($M\infty = 0$; $Q = 0.4$ kg.s-1) case and the other for ($M\infty = 0.116$; $Q = 0.4$ kg.s-1) case. The mean flow around the geometry is obtained via a RANS approach using the Cartesian solver of FastS [66], [67], [68], [69], [70], [71] developed at ONERA, the geometry being taken into account also via the IBM (as for the CAA). More details on the IBM implemented in FastS can be found in Péron et al. [67], [70].

For both simulations, the intake suction is modelled by two disks, one on each end of the T-junction. The two disks are depicted in red in Figure 3-5 (left). On these two disks, an outlet boundary condition based on a uniform static pressure pout is imposed. The boundary conditions parameters values have been adapted in order to get the specific mass flow rate corresponding to the target point $Q = 0.4$ kg.s-1. It can also be noted in Figure 3-5 (left), that no exhaust opening is present for the numerical geometry as the present simulations focus on the intake only.

The CFD octree mesh is composed of 20.5 × 106 cells with 244 Cartesian blocks. A longitudinal cut in a mid-nacelle plane of the 3D mesh is depicted in Figure 3-5 (right), where the local mesh refinements near the sharp edges of the geometry can be noticed.

The turbulence modelling is handled by the Spalart-Allmaras model [72]. Musker's algebraic wall function is applied within the IBM approach on Cartesian grids to solve high-Reynolds number flows. The second-order accurate Roe-MUSCL spatial scheme is used with a first-order accurate implicit time integration and a local time step. The RANS computation was performed on 1 node of an ONERA in-house cluster with 24 OMP threads. More than 20 × 103 iterations were computed to ensure a convergence of the residuals (a decrease of about 4 orders of magnitude was obtained). The total computational time was about 200 hours (elapsed) for each computation.

Color maps of the axial velocity of the mean flow around and inside the geometry are depicted in Figure 3-6. On the right figure, the influence of the ambient flow can be seen around the intake lips, notably with the velocity drop. This may influence the propagation of the acoustic waves coming from inside the geometry to the outside, besides the presence of the ambient flow at $M\infty = 0.116$.

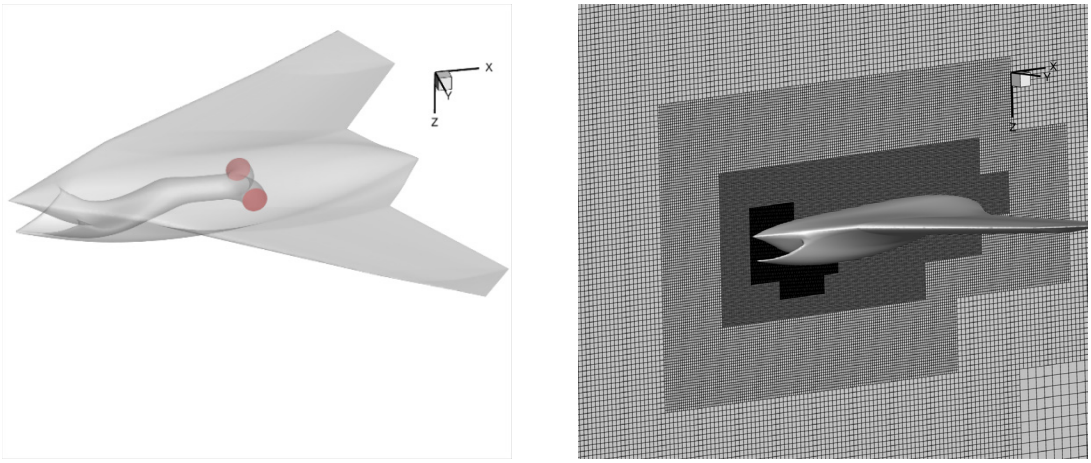

**Figure 3-5: Illustrations of (Left) the Geometry with the Static Pressure Boundary Conditions (in Red) and (Right) the CFD Mesh for the Mean Flow Computations.**

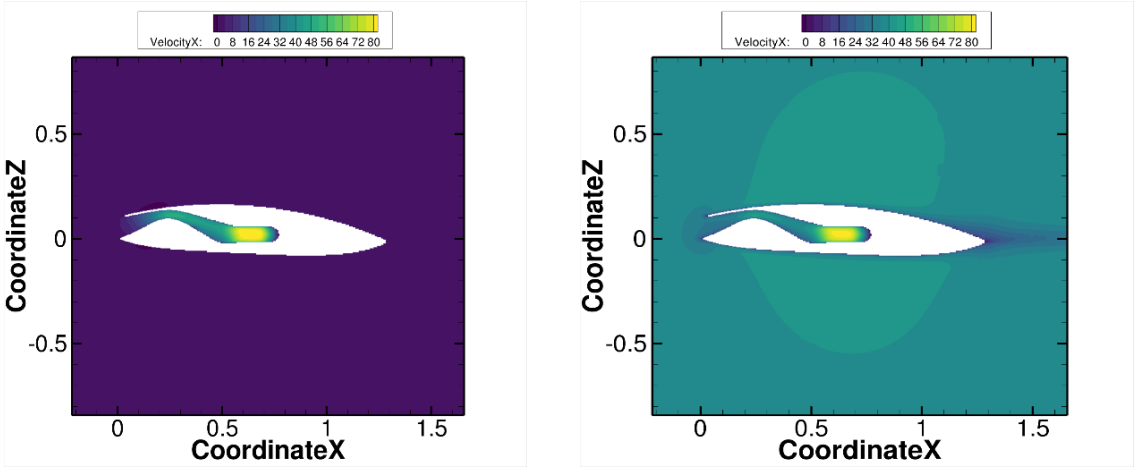


**Figure 3-6: Contour Maps in the Midsection Plane of the Geometry of Axial Velocity of the mean Flow with Q = 0.4kg.s$^{-1}$ for (Left) the $M_\infty$=0 Configuration and (Right) the $M_\infty$ = 0.116 Configuration.**

### 3.2.3 FOI's Methodology

Mattias John Quas, Shia-Hui Peng and Samuel Gottfarb Bart, FOI

Fluid dynamics simulations and computational aeroacoustics simulations have been conducted related to the jet noise for different designs of a 1/8 scale version of the MULDICON airframe. The MULDICON design originates from planforms as first proposed by Nangia [73] and Schütte [74] during the work in AVT-251, see also in Ref. [1] by Cummings, Liersch and Schütte for a comprehensive overview. The AVT-251 group investigated different designs of intake and outlet for the MULDICON airframe from many aspects, see e.g., Refs. [2], [75], and [76]. The largest characteristic length scale for the MULDICON geometry is the span. One of the other larger length scales for MULDICON is the aircraft length $L_{AC}$, for the scaled model approximately 1.3 m for the fuselage. The jet outlet double curved S-shaped channel is roughly 0.3 m long and the rectangular shaped, lid-like cross section of the nozzle outlet is 0.020 m × 0.26 m. The shape of channel and nozzle is highly three-dimensional, as seen in Figure 3-7, with an oval shaped engine outlet exiting into a double curved S-shaped exhaust channel. Four different designs were investigated during the course of the work with respect to steady state fluid dynamics, see Table 3-1 and Figure 3-7. The four designs B1a, B1b, B2a

and B2b differ from each other at the inlet region and outlet, aft body region. The design name convention is to be interpreted in such a way that design *1* had no extension plate on the nozzle whereas design *2* had an extension plate. Index *a* indicates that the design had an open air intake and index *b* indicates that an intake cover was applied. For the scale resolving simulations, designs B1a and B2b were considered.

The grids used in the steady state RANS computations were created using the software Cadence/ Pointwise. The grids used in the RANS-LES simulations were created using ANSYS ICEM CFD as an initial background grid and then exported and refined in the volume using the FOI in-house mesh generation program TRITET [77], [78]. All grids were unstructured with tetrahedral cells in the volume and prism cells in the near wall region, with triangular faces towards the surfaces. The grids created for the steady state RANS computations correspond to half the MULDICON geometry and facilitate a symmetry plane with symmetry boundary conditions. The grids used in the time resolved RANS-LES simulations were generated based on the complete geometry. The computational domain farfield border was spherical and at a distance of more than 150 aircraft lengths from the MULDICON airframe. The MULDICON airframe was located in the center of the computational domain.

**Table 3-1: Four Different MULDICON Designs Investigated by Means of Steady State RANS Computation and Scale Resolving RANS-LES Simulation. The RANS geometries only considered half the MULDICON airframe and incorporated symmetry conditions. The hybrid RANS-LES geometries facilitated the full geometry.**

| | B1a | | B1b | B2a | B2b | |
|---|---|---|---|---|---|---|
| | RANS | RANS-LES | RANS | RANS | RANS | RANS-LES |
| Control volumes | 11 000 000 | 47 000 000 | 11 000 000 | 12 000 000 | 11 000 000 | 51 000 000 |
| Intake channel | Open | | Covered | Open | Covered | |
| Outlet extension | No | | No | Yes | Yes | |

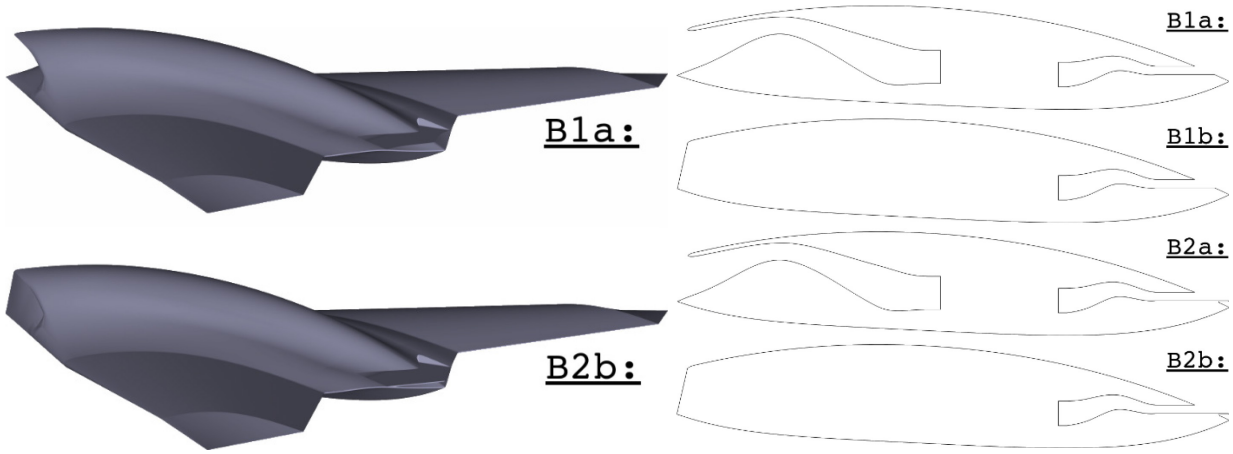


**Figure 3-7: MULDICON Geometry. Left: Perspective views of designs B1a and B2b. Right: Symmetry cross section outline for designs B1a, B1b, B2a and B2b. The intake aperture is located to the left with open intake, index *a* or covered, with index *b*. The outlet is located to the right, with or without extension plate, index *1* or *2* respectively.**

On the surface of the MULDICON fuselage, intake, outlet and wing sections, the default surface triangle grid size was set to 5 mm. In regions with large geometry curvature, the grid size was adjusted smaller, to facilitate the geometric shape of the airframe. In the outlet nozzle region, the volume grid size length scale

was set to 5 mm. The overall target thickness of the prism layer used to capture the velocity gradients of the near wall flow was set to 0.06 m on the external surface of MULDICON, with a first layer thickness of $1 \cdot 10^{6}$ m and an expansion ratio of 1.2 ending up with a target number of about 65 layers depending on the geometry. In the outlet channel, the thickness of the prism layer was much smaller, 0.018 m in the first part and only 0.007 m in the narrow nozzle region, see Figure 3-8, right. The grids facilitate extensive step-wise refinement downstream the MULDICON to properly resolve the jet flow physics. The jet refinement was divided into five regions positioned downstream of the nozzle, each with its individual grid size. The division into refinement regions corresponds to the individual segments on the integral surface adopted for acoustics analysis purpose. In Figure 3-9 the outer integral surface surrounding the jet from the B1 geometry outlet is shown in two different views, from the side and in perspective. Within the five different regions, the target tetrahedral grid size was different ranging from 7 mm up to 25 mm with smaller cells in the vicinity of the nozzle and larger cells further downstream. Outside the jet flow region, the grid sizes were gradually increased. Grid sizes are indicated in Table 3-1.

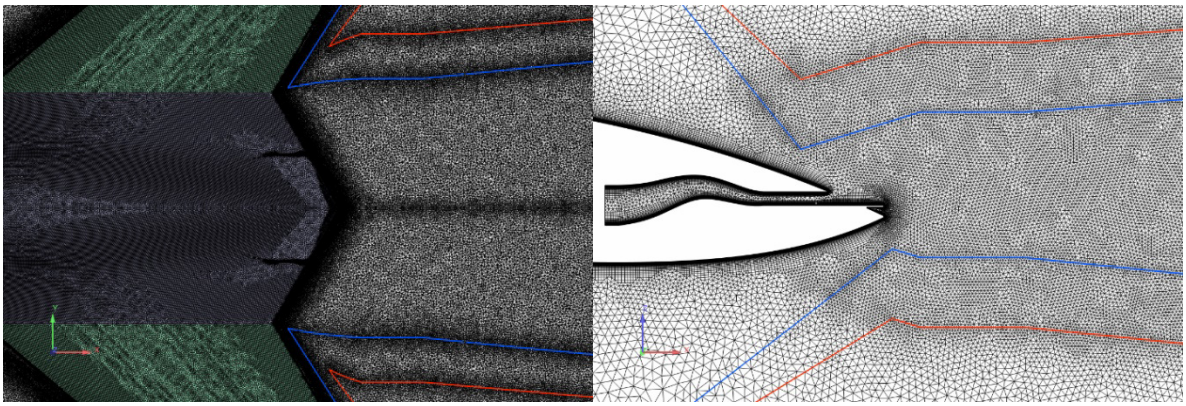

**Figure 3-8: MULDICON B2b Full Model Grid Used for Hybrid RANS-LES. The blue lines indicate the inner integral surface. The red lines indicate the outer integral surface. Left: View of the aft body, from above. Right: View from the side, the symmetry cross section.**

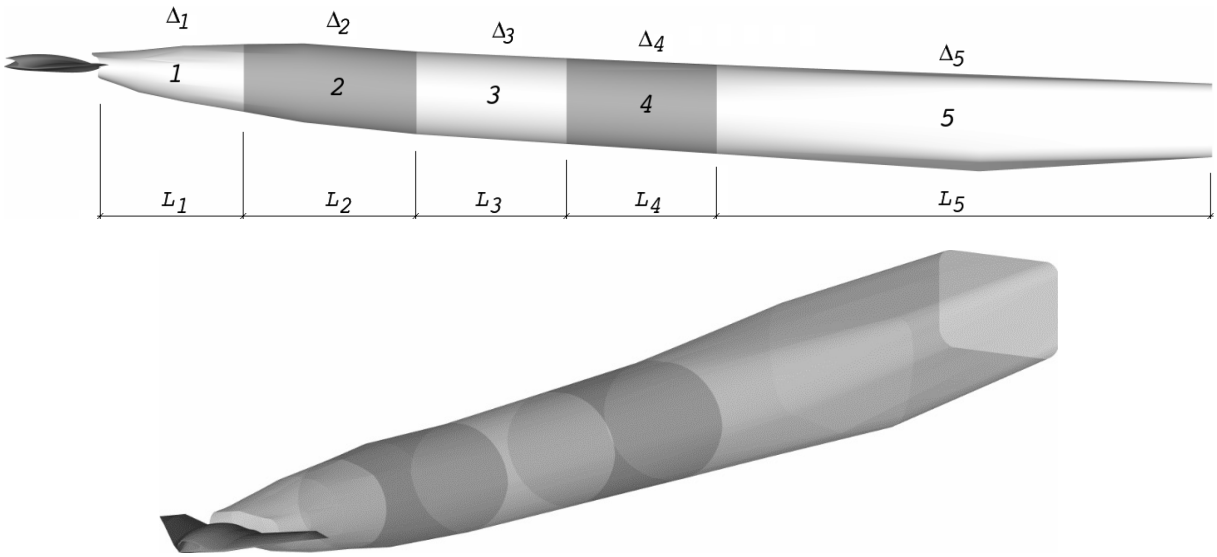


**Figure 3-9: Outer Integral Surface for Acoustics Sampling Shown for the B1 Geometry. Segment Length $L_i \in \{1.5, 1.5, 1.5, 1.5, 5\}L_{AC}$, and i ϵ {1, 2, 3, 4, 5} Respectively. The segments are enclosing volume regions 1 through 5 with corresponding grid size length scales $\Delta_i \in \{0.007, 0.012, 0.016, 0.022, 0.025\}$ mm. Upper: Side view. Lower: Perspective view.**

Both steady state RANS computations as well as scale resolving transient hybrid RANS-LES computations on the jet plume exiting the engine nozzle have been conducted. The computations were carried out to explore both the mean as well as the instantaneous aerodynamic flow features for the different designs considered. The simulations also serve as a basis for the aeroacoustics analyses. For both steady state RANS and hybrid RANS-LES computations, the M-Edge code [62] has been used. M-Edge solves the compressible Navier-Stokes equations based on a node centered finite volume approach. In the simulations, the aim was to compute wall resolved flow and thus, no wall model was used. To obtain the mean flow characteristics, computations were conducted using the Spalart-Almaras one-equation model [72] or the explicit algebraic EARSM [79] for the turbulence closure. For the purpose of obtaining time dependent data needed for the aeroacoustics analyses, as argued in Section 3.1.4, a hybrid RANS-LES approach was adopted. The basic idea with the hybrid RANS-LES numerical method is to use the more affordable unsteady RANS numerical approach in the part of the computational domain, where the flow features are steady (non-fluctuating), and an LES filtered numerical approach where the flow experiences large fluctuations, such as regions with flow separation and wakes. Hybrid RANS-LES is the engineering approach to high-fidelity computational fluid dynamics and the methods promise less computational cost than full LES and higher fidelity than unsteady RANS in the regions of large fluctuating flow. Being a topic of extensive research, approaches for hybrid RANS-LES come in many variants. The hybrid RANS-LES adopted in this context were set up using the zero-equation algebraic HYB0 model by Peng [80], [81].

In the simulations, slip boundary conditions were applied to the major parts of the wings of MULDICON. That way, the contribution with respect to vorticity from the wings to the acoustic noise profile of the jet was lowered. The fluid dynamic and transport properties used in all computations correspond to those of air at room temperature $T_0$ = 293.15 °K, with the freestream static pressure $p_0$ = 101325 Pa, the dynamic viscosity $\mu$ = 1.825 $\cdot 10^{-5}$ Pa·s, the Prandtl's number $Pr$ = 0.72 and the heat capacity at constant pressure $Cp$ = 1004.5 J/°K and ratio of $\gamma$ = 1.4 assuming that ideal gas law applies.

# Chapter 4 – SHIELDING FLAP NOISE REDUCTION DESIGN

**Ian Clark, Yueping Guo, Russell Thomas**
NASA
UNITED STATES

The noise reduction approach that the NASA team chose would focus on the aeroacoustic effects associated with the integration of the propulsion and airframe of the MULDICON [1] vehicle. An image of the MULDICON geometry is shown in Figure 4-1 showing the rectangular nozzle blended with the center body trailing edge of the vehicle. The design requirements stated that the technology should:

- Reduce aft-radiated noise;
- Prioritize reducing the scattering of turbomachinery noise over reducing jet noise;
- Conceivably be integrated with the MULDICON vehicle design although the detailed mechanical design would not be a focus; and
- Possibly be a deployable device.

In addition, it was desired that essential aeroacoustic effects could be investigated experimentally at a reasonable cost in the NASA Langley QFF using the basic NACA 0012 experimental approach with the laser spark point noise source that was developed in the AVT-233 task group.

An added design requirement is that the aft-radiated noise reduction should be primarily in the aft polar angles; that is, in the angles farther downstream. This is because achieving noise reduction in these far downstream angles is typically more difficult to accomplish [11], [12], [16].

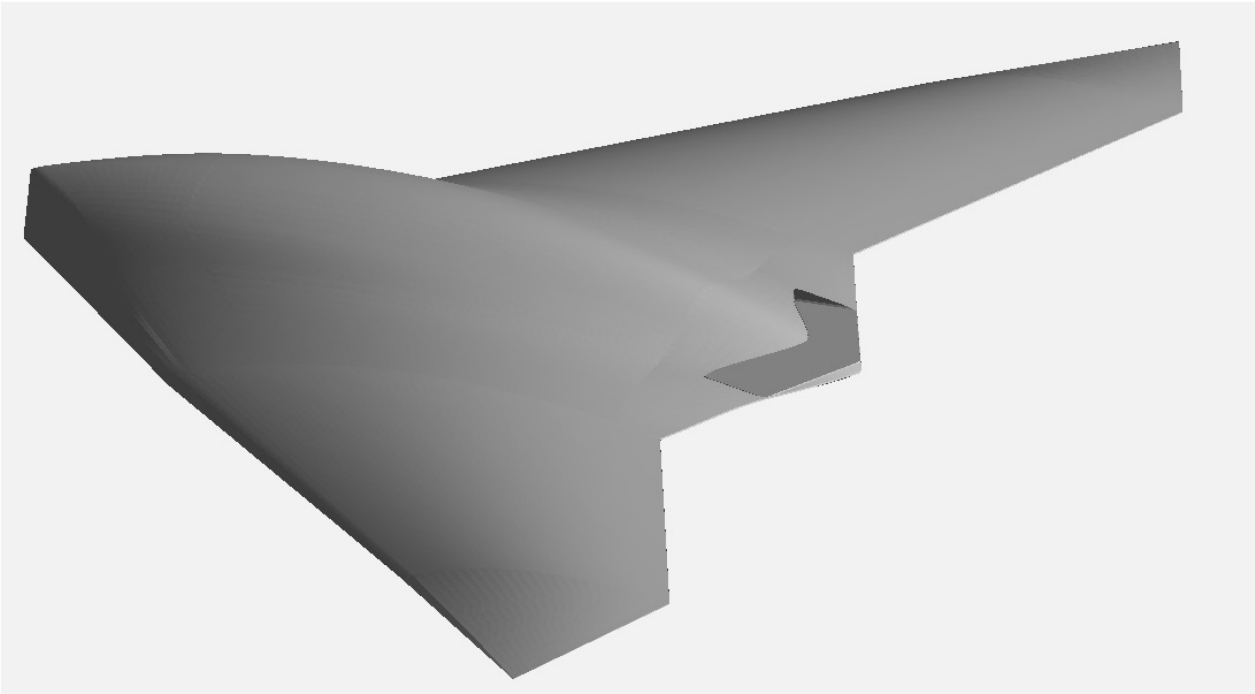

**Figure 4-1: MULDICON Uninhabited Combat Aerial Vehicle Design with Rectangular Nozzle.**

A view of the cross section of the nozzle and trailing edge is shown in Figure 4-2. The small horizontal extension of the lower nozzle surface was added by the AVT-318 team to prevent the nozzle jet exhaust flow from deflecting downward because of a Coanda effect. The view of Figure 4-2 also shows two primary noise sources, turbomachinery and jet, that will scatter off of the trailing edge geometry. While the turbomachinery noise propagates from the exit plane of the nozzle, the jet has a distribution of noise sources over an axial length downstream as indicated by the image. A third noise source is an interaction of the high-speed turbulent jet flow with the trailing edge. In this case, the source of the interaction is in the immediate vicinity of the trailing edge. The work of the AVT-318 team described in Chapter 5 has shown that the jet-trailing edge interaction is a significant element of the total aft-radiated noise signature.

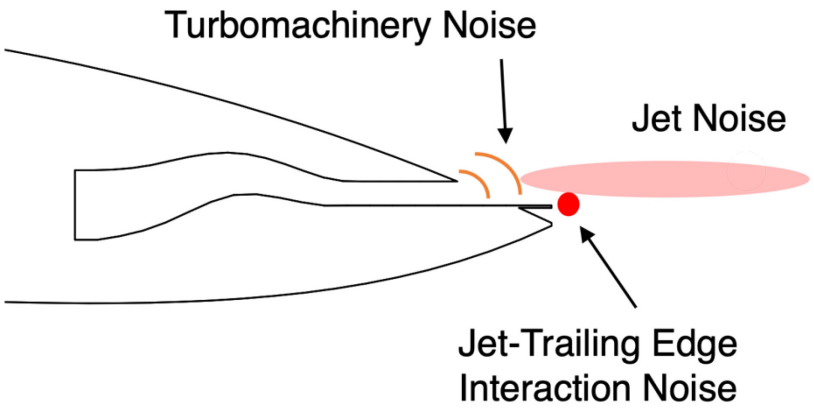


**Figure 4-2: Cross-Section View at the Centerline of the MULDICON Nozzle and Trailing Edge.**

The most basic addition to the geometry that could reduce turbomachinery noise in the far downstream polar angles would be a simple extension onto the lower surface of the jet nozzle. This could also shield some of the jet noise sources. However, it would only move the jet-trailing edge interaction to the new, farther downstream, trailing edge location. The deployment of this extension, while conceivable, is practically less obvious.

As a result, this simplistic extension concept was rejected by the NASA team in favor of the more complex Shielding Flap concept. The original MULDICON centerline design, the simple Edge Extension, and the selected Shielding Flap concept are all shown in Figure 4-3 for comparison. The Shielding Flap introduces several advantages for noise reduction:

- Prevention of jet scrubbing on the Shielding Flap such that there would be no jet-trailing edge interaction noise;
- The Shielding Flap would be lower and downstream of the jet-trailing edge interaction so that the Shielding Flap would shield not only turbomachinery noise but also the jet-trailing edge interaction noise and jet noise;
- The Shielding Flap could easily be a deployable device, stowed in cruise in the underside of the MULDICON and deployed for noise-sensitive parts of a mission at lower speed, low-altitude flight conditions; and
- The Shielding Flap could be utilized for vehicle control or as a speed brake in addition to deployment for noise reduction.

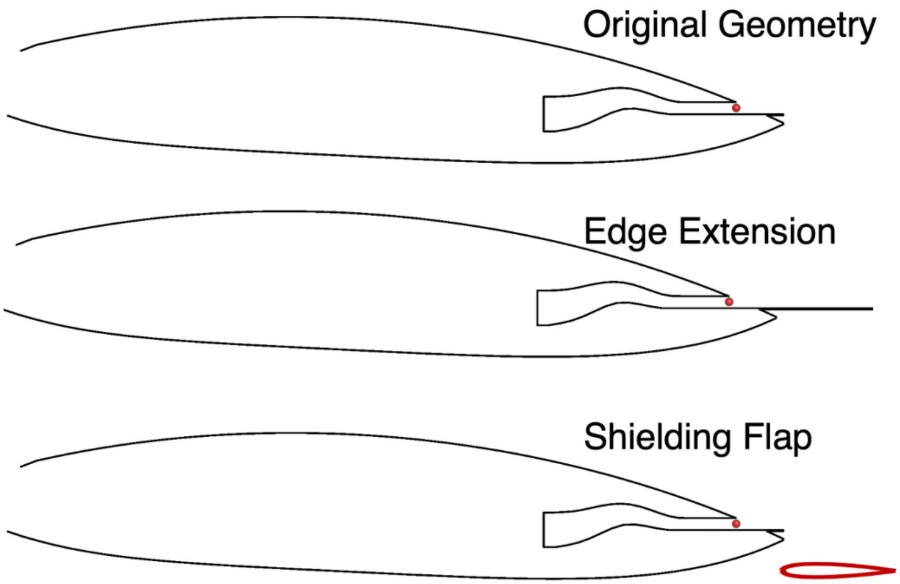


**Figure 4-3: Side View of the Original MULDICON Centerline Geometry (top), the Simplistic Edge Extension Concept (Middle), and the Shielding Flap Noise Reduction Concept (Bottom).**

The Shielding Flap is deceptively simple in that while it has the advantages listed above, it also introduces additional parameters and physical effects that require the investigation of the AVT-318 group and that make this a challenging design exercise. These parameters include:

- Positioning below and axially downstream or upstream relative to the main-body trailing edge;
- The width of the gap between the Shielding Flap and main body with a nonuniform flow;
- Angle-of-attack that could be positive or negative;
- The cross section, which could be a flat plate or an airfoil; and
- The planform shape of the Shielding Flap, which could have many possibilities and choices.

The refined design objective is summarized notionally in Figure 4-4 for the Shielding Flap relative to the more simplistic Edge Extension concept. It represents a tradeoff of less noise reduction in the shadow region (directly under the vehicle) while seeking more noise reduction in the downstream polar angles that do not have direct line-of-sound shielding potential. Introducing the gap between the flap and main body creates some leakage of sound into that shadow region under the body and, in turn, there are new parameters, listed above, that can be used in the design to increase noise reduction in the downstream angles.

It is asserted that much of the essential acoustic physics of scattering effects can still be studied in the NASA Langley QFF with the simplifications of using the NACA 0012 experiment with the laser spark noise source developed during the AVT-233 task group, schematically represented in Figure 4-5. Figure 4-6 shows how essential physics relevant to the Shielding Flap can be experimentally studied with parameter variations including:

- Sharp edge diffraction;
- Scattering from multiple bodies (main body and the Shielding Flap);
- Effect of the gap flow on upstream scattering; and
- Effect on scattering of the main body and flap boundary layers.

Of course, it does represent an additional step to transfer the learning from the QFF experiment to the MULDICON with realistic turbomachinery and hot jet noise sources. Much of this can be done with the prediction methods developed by the group, the PAASc method in the case of the NASA team.

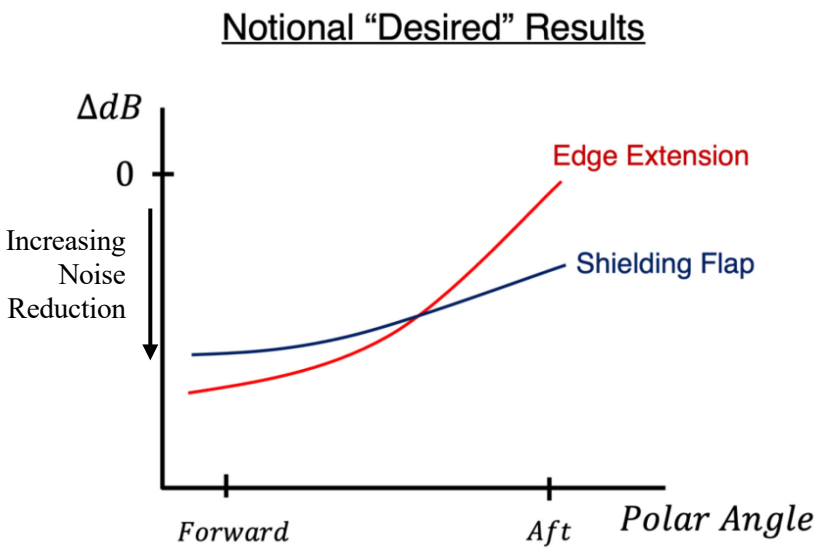


**Figure 4-4: Notional Refined Design Objective of Achieving Increased Noise Reduction in the Downstream Angles Even at the Expense of Some Noise Reduction Directly Under the Vehicle.**

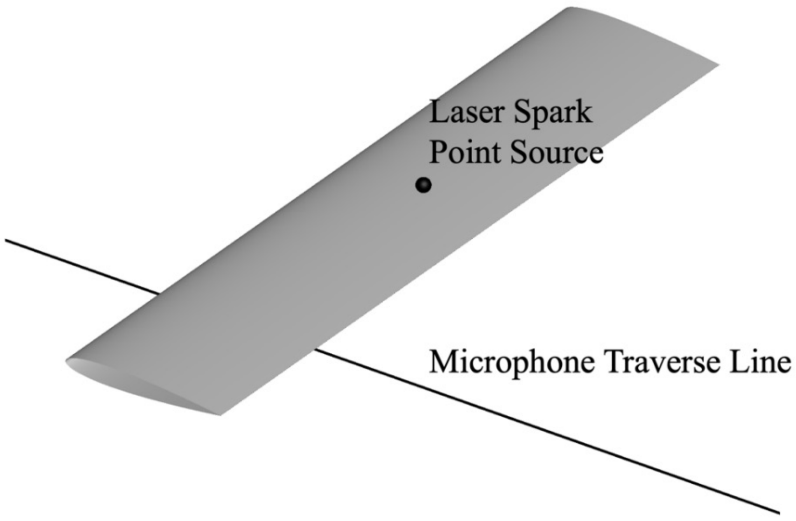


**Figure 4-5: Simplified Schematic of the NACA 0012 Airfoil Experiment with the Laser Spark Point Source to Study Much of the Essential Physics for the Shielding Flap Concept.**

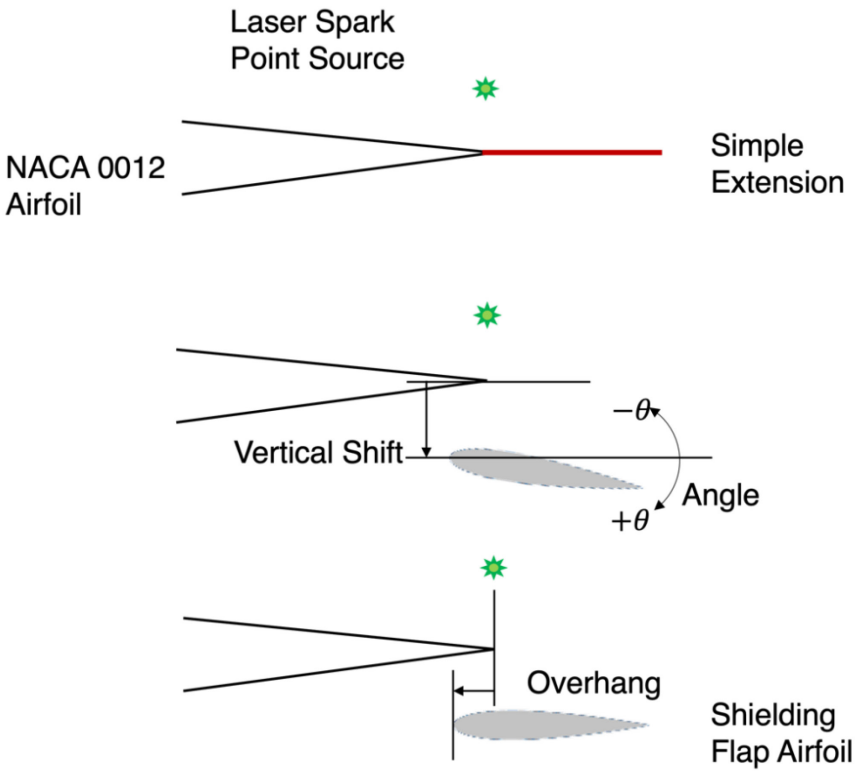


**Figure 4-6: Schematic of How the NACA 0012 Experiment with Laser Spark Source can Study Much of the Essential Noise Scattering Physics Relevant to the Shielding Flap Concept.**

The ultimate implementation of the Shielding Flap concept on the MULDICON can be rendered, in end view, in Figure 4-7, and in an additional pictorial view, in Figure 4-8. Conceptually, therefore, the Shielding Flap should meet all the design requirements. The real design challenge for the team is to understand the acoustic effects of the parameters and, through experiment and prediction, to select the successful design.

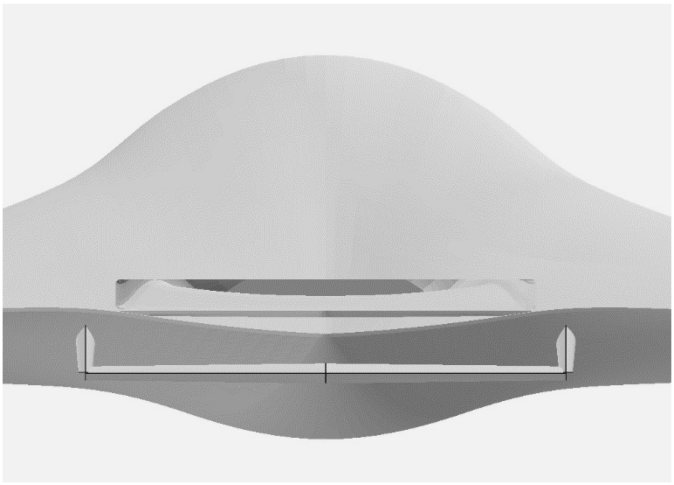

**Figure 4-7: End View of the MULDICON Vehicle with the Rendering of the Shielding Flap Concept as it Would be Deployed During a Noise-Sensitive Segment of a Mission.**

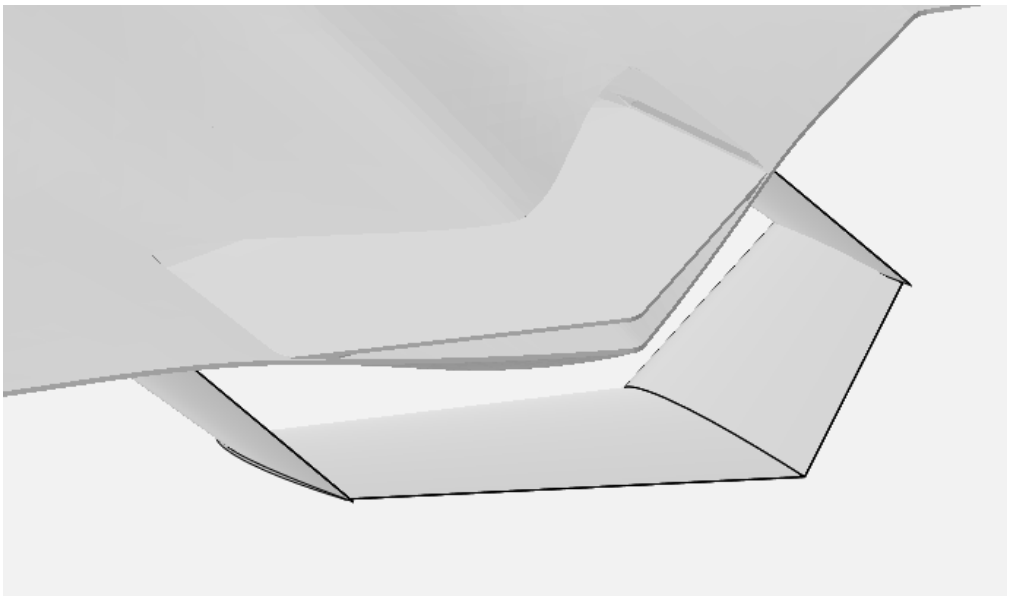

**Figure 4-8: Rendering of the Shielding Flap Noise Reduction Concept as Deployed from the Trailing Edge of the MULDICON Vehicle.**

# Chapter 5 – RESULTS OF THE EXPERIMENTAL INVESTIGATIONS

**Karl-Stéphane Rossignol and Jan Delfs**
DLR
GERMANY

**Yueping Guo and Florence Hutcheson**
NASA
UNITED STATES

**Fabrizio De Gregorio and Carmelo Izzo**
CIRA
ITALY

## 5.1 RESULTS OF THE DLR-F24 MULDICON UCAV MODEL INVESTIGATION

Karl-Stéphane Rossignol and Jan Delfs, DLR

In this section, analyses of both the intake and jet noise radiation of the DLR-F24 MULDICON model are presented in terms of their source directivity and spectral characteristics. Most of the results presented in this section were previously published in Refs. [3] and [73].

### 5.1.1 Intake Acoustics

The parameters of interest for the experiment included variations in upstream Mach number, variations in suction mass flow rate, and combinations of both. Furthermore, the model is equipped with optical ports to allow the use of a laser-based impulsive point-like sound source to generate pressure pulses in the intake duct. Thus, using this technique, acoustic propagating modes can be triggered inside the duct and the corresponding acoustic free-field radiation is acquired using the in-flow microphones.

Third octave band directivity data for frequencies $f_{c,1/3}$ = 0.8, 4, 10, 40 kHz are given in Figure 5-1 as a function of free-stream Mach number and suction mass flow rate. In this figure, the sound radiation from the laser-based sound source is given in black, airframe noise is given in green and suction noise in blue. At the 4 kHz third octave band suction and airframe sound approximately reach their peak amplitude, whereas the laser sound source peaks in the 40 kHz third octave band. The emitted intake's sound directivity is found to have its maximum towards the upstream direction at angles below or equal to $\varphi_x = 45°$, regardless of the operating conditions considered in the experiments. Airframe noise, on the contrary, is almost omni-directional.

The parametric dependence of the laser-induced intake sound on the free-stream Mach number and mass flow rate is presented in Figure 5-2 for a third octave band frequency of $f_{c,1/3} = 40$ kHz; frequency at which laser sound reaches its peak. The results of Figure 5-2 demonstrate that convection effects through variations of the free-stream velocity do not affect the directivity of intake sound nor does it affect its absolute level. The most important factor influencing the acoustic emissions is the suction mass flow rate, which potentially affects both the directionality and absolute sound pressure level.

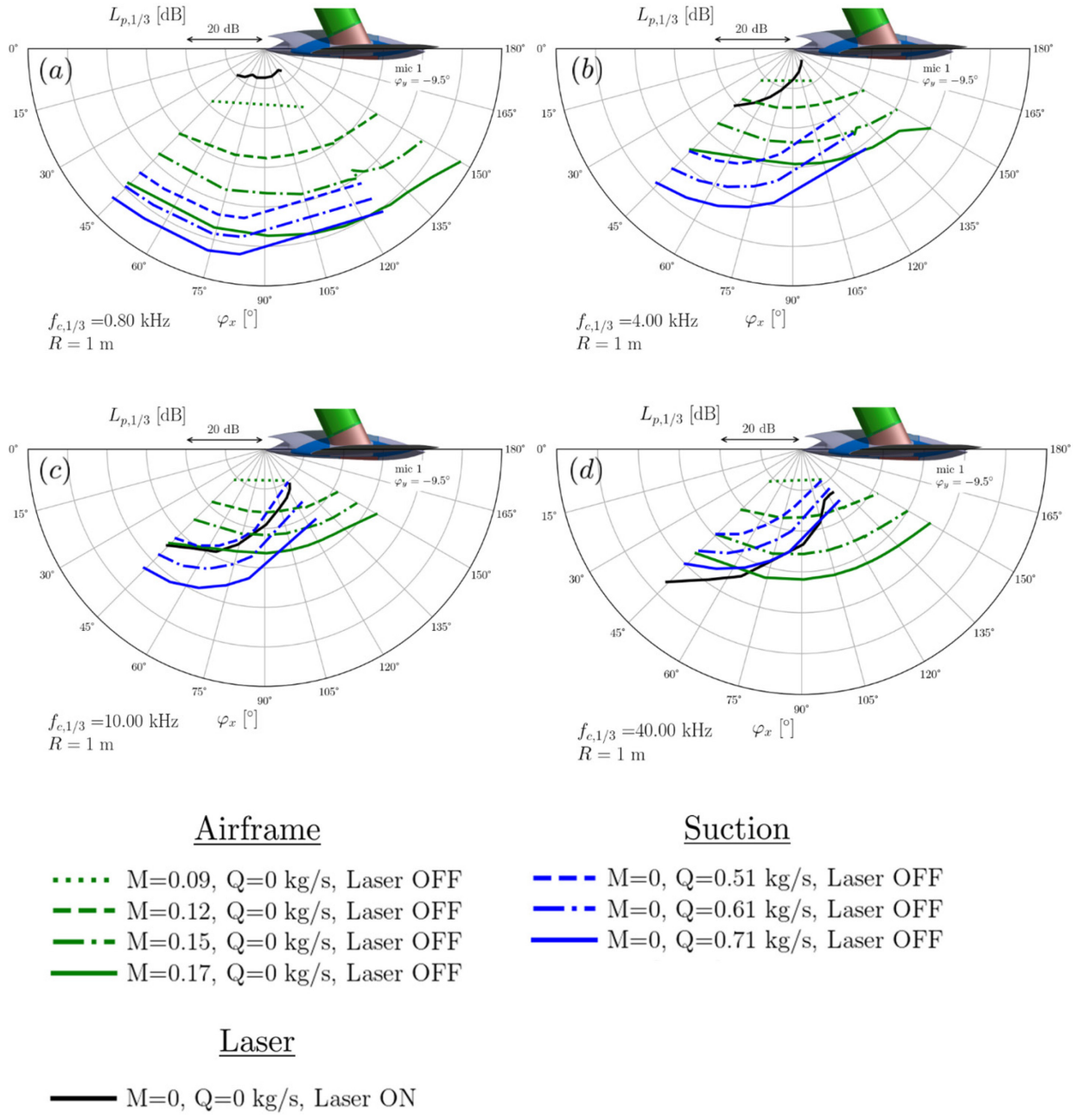


**Figure 5-1: Intake Sound Radiation vs. Free-Stream Mach Number (M) and Suction Mass Flow Rate (Q) for Selected Third Octave Band Frequencies.**

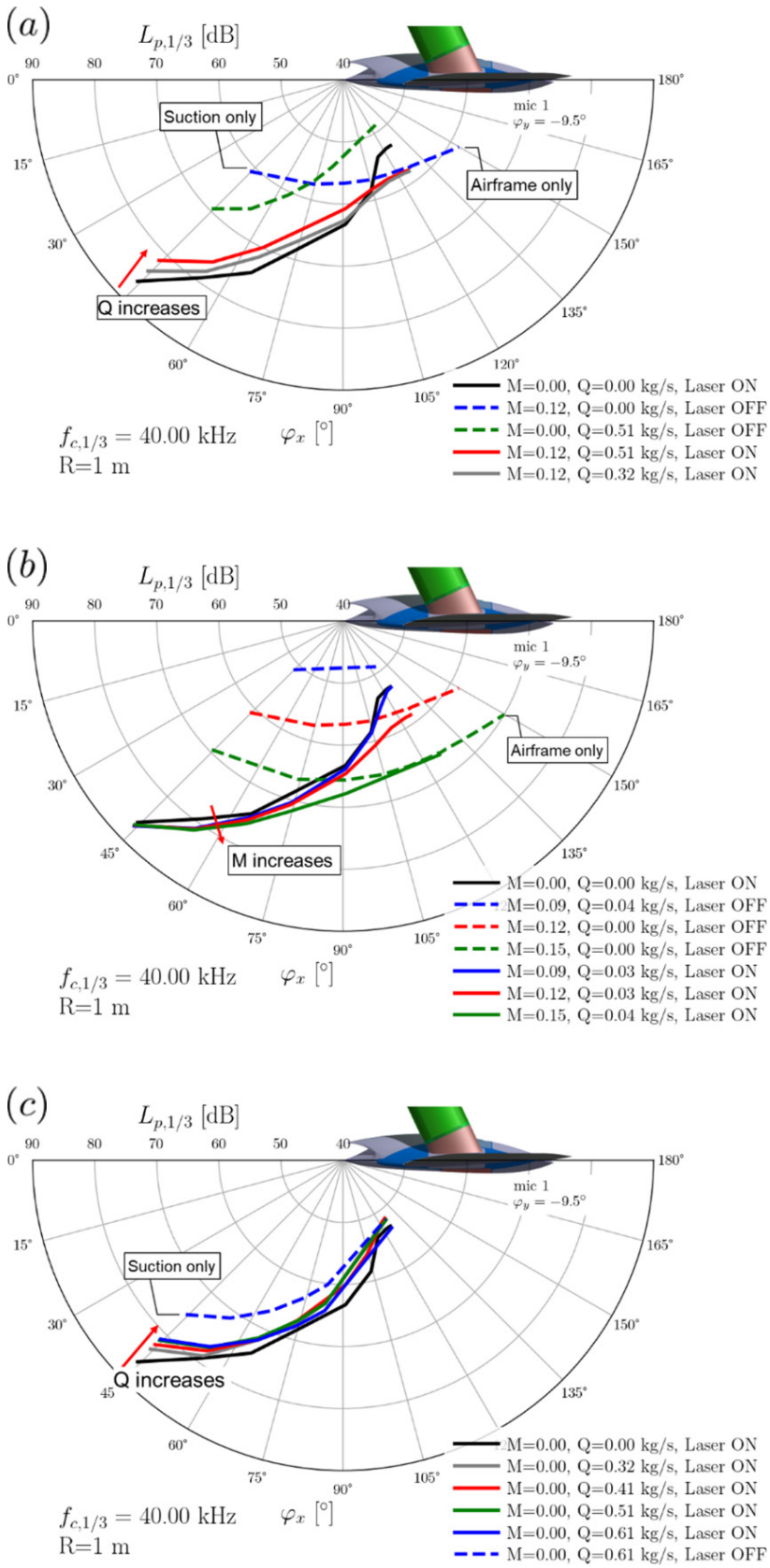


**Figure 5-2: Effect of the Free-Stream Mach Number (M) and Mass Flow Rate (Q) on Laser-Induced Intake Sound Radiation. $f_{c,1/3} = 40$ kHz**

### 5.1.2 Nozzle Acoustics

Results for the nozzle acoustic radiation as a function of the free-stream Mach number and jet mass flow rate are presented in Figure 5-3 for selected one-third octave band frequencies. At the lowest one-third octave band frequencies considered herein, in Figure 5-3(a), Figure 5-3(b), jet noise appears to reach its maximum sound pressure level at an approximative angle $\varphi_x = 105°$. Variations in free-stream Mach number or nozzle mass flow rate only have a minor effect on the absolute acoustic radiation levels; as if some cutoff conditions were met. From $f_{c,1/3} = 3.15$ kHz up to $f_{c,1/3} = 10$ kHz, the acoustic data are found to depend strongly, and almost exclusively on the nozzle mass flow rate. The overall directionality of the sound at $f_{c,1/3} = 3.15$ kHz and $f_{c,1/3} = 4$ kHz, suggest a combination of two main source components, one aligned with the $\varphi_x = 105°$ direction and a second one aligned with the $\varphi_x = 140°$ direction. At $f_{c,1/3} = 6.3$ kHz and $f_{c,1/3} = 10$ kHz, the first component loses in intensity compared to the second one, giving rise to a typical rearward-oriented jet noise maximum.

These observations are somewhat unexpected and could be a characteristic of the type of nozzle considered in the investigation. To offer some clarification we now look at the narrow-band spectral data. We are considering the topmost in-flow microphone shown in the arrangement of Figure 2-12 and Figure 2-13, with $\varphi_y = 9.5°$. Our focus is put on the $\varphi_x = 90°$ and $\varphi_x = 145°$ measurement directions, where according to Tam et al. [83] for an isolated jet in static conditions, jet noise radiation is related to two distinct source mechanisms. The authors respectively define two seemingly universal spectra: the F-spectrum or peaky spectrum fits all noise spectra measured in the downstream directions within a cone around the jet axis, and the G-spectrum or the broad spectrum which fits all noise spectra radiated in the upstream and sideline directions. In the transitional directions a superposition of the contributions from the two spectra is required to fit the measured spectra [83]. Moreover, these universal spectra were also shown to be an adequate representation of subsonic jet noise from axisymmetric and non-axisymmetric nozzles [84]. There is no a priori reason to believe that these spectra should accurately represent our experimental data; especially considering the current nozzle geometry. However, the analysis of Rossignol et al. [3] does suggest the existence of two source components in the current data.

In Figure 5-4, narrow band spectra are given for the static and co-flow cases respectively. In all cases, one notices the peaky nature of the spectra with a peak frequency dependent on jet velocity. As noted in Ref. [3], apart from slight changes in high-frequency behavior, the spectral shape of the results appears unaffected by the co-flow. Interestingly, at $\varphi_x = 90°$, the co-flow also has almost no impact on the absolute spectral level, particularly for frequencies up to about 4 kHz. An indication that a trailing edge-like mechanism, which is dependent on the absolute velocity in the vicinity of the edge, most probably plays an important role. This is not the case at $\varphi_x = 145°$, where at $U_\infty = 60\ \mathrm{m/s}$ the maximum spectral level drops by approximately 7 dB.

We now look at the amplitude and frequency scaling of the narrow-band data of Figure 5-4. The frequency axis is made dimensionless, on a Strouhal number basis, using the nozzle height, h, as characteristic length scale, and the velocity difference, $U_j - U_\infty$, or the absolute jet velocity $U_j$, as characteristic velocity scales.

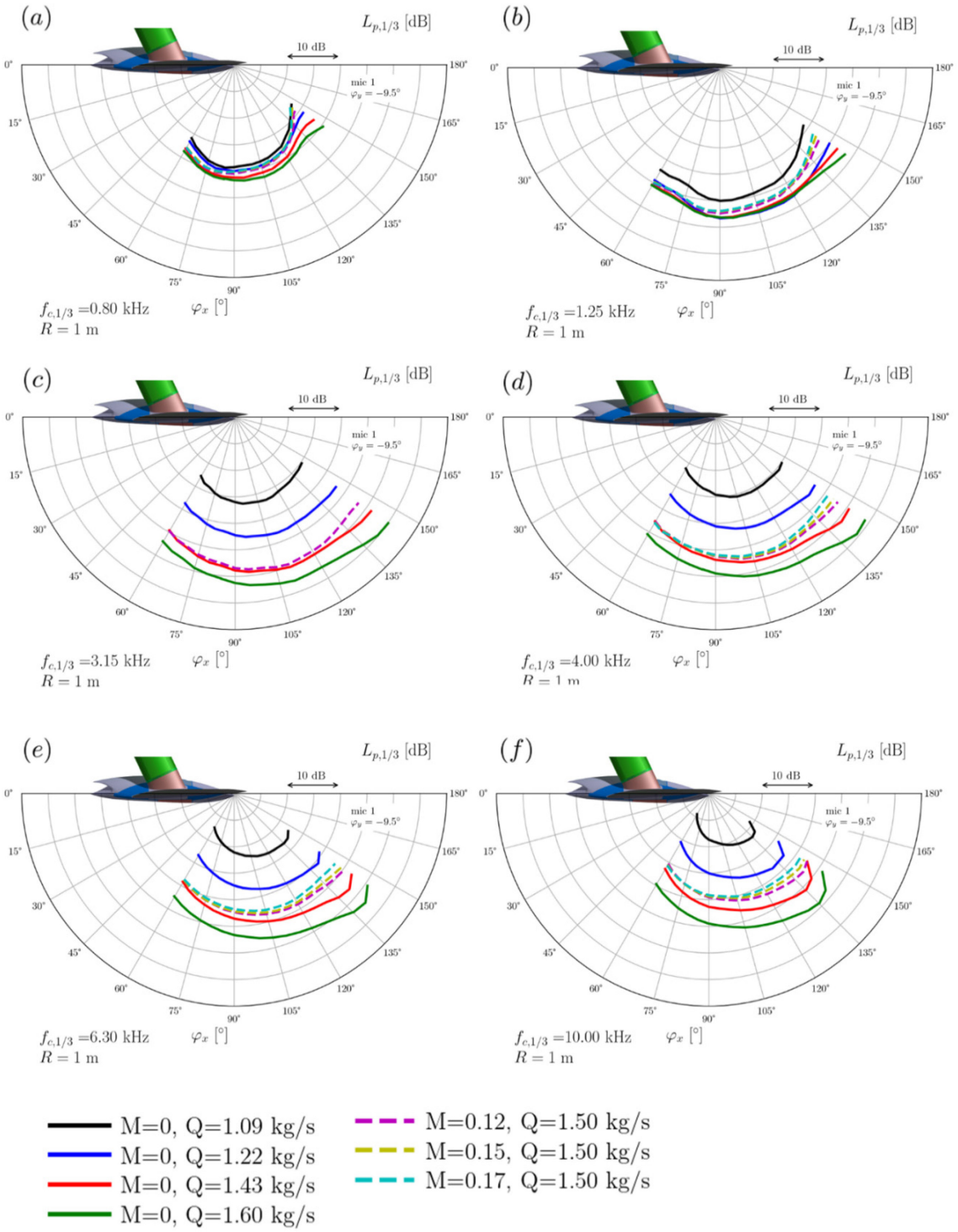


**Figure 5-3: Jet Noise Directivity 9.5° to the Sideline vs. Free-Stream Mach Number (M) and Jet Mass Flow Rate (Q) and for Selected Third Octave Band Frequencies.**

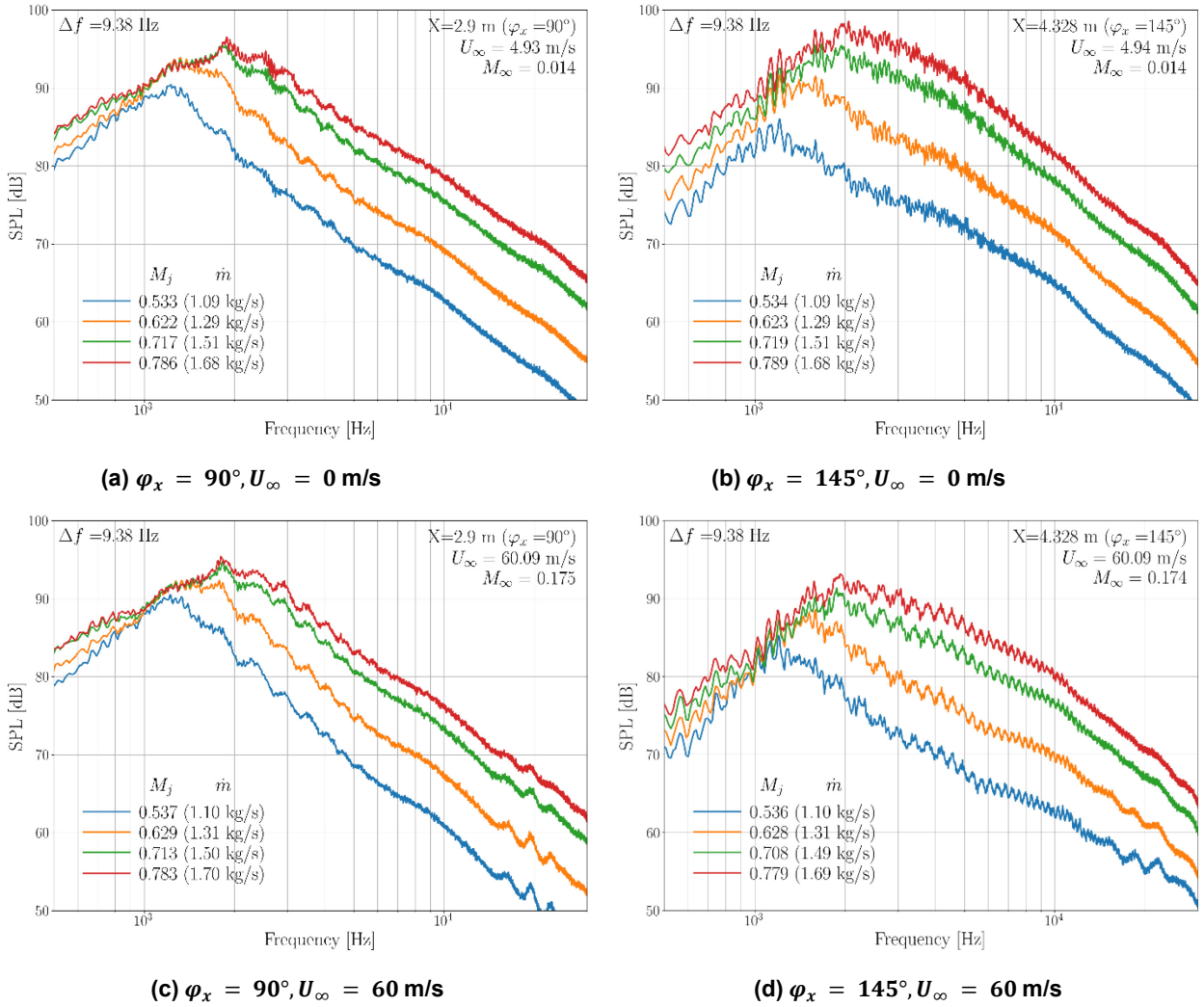


**(a) $\varphi_x = 90°, U_\infty = 0$ m/s** **(b) $\varphi_x = 145°, U_\infty = 0$ m/s**

**(c) $\varphi_x = 90°, U_\infty = 60$ m/s** **(d) $\varphi_x = 145°, U_\infty = 60$ m/s**

**Figure 5-4: Effect of Co-Flow on Jet Noise Radiation for $\varphi_x = 90°$ and $\varphi_x = 145°$ and $\varphi_y = 9.5°$. In-flow measurements, $R$ = 1 m.**

### 5.1.2.1 Static Conditions

For the static case we consider an amplitude scaling assuming a proportionality of the form $L_p \propto U_j^n$ with $n = 5$, i.e., edge noise source mechanism, and $L_p \propto (U_j - U_\infty)^n$ with $n = 8$, i.e., jet noise source mechanism. Spectra scaled with a $n = 5$ scaling exponent are given in Figure 5-5(a) and (c), while results obtained with a $n = 8$ scaling exponent are given in Figure 5-5(b) and (d). Figure 5-5(a) and (b) are for emission angle $\varphi_x = 90°$ and Figure 5-5(c) and (d) are for emission angle $\varphi_x = 145°$. For emission angle $\varphi_x = 90°$, the spectral peak levels, up to $St \approx 0.3$, are successfully scaled using a $n = 5$ power exponent. Above $St \approx 0.3$ the data scale using a $n = 8$ exponent. This emphasizes that, for $\varphi_x = 90°$, the interaction of the jet with the aft-deck of the nozzle dictates the most part of the spectra. Free turbulence jet noise only plays a secondary role. A different picture is found for emission angle $\varphi_x = 145°$, where a better collapse of the spectra is possible only with a power exponent $n = 8$. Here, free turbulence jet mixing noise dominates.

The spectral shape of the scaled spectra for both emission angles is reminiscent of the large scale universal similarity spectrum, i.e., F-spectrum, defined by Ref. [83]. This is rather unexpected at the $\varphi_x = 90°$ radiation direction while consistent with the awaited rear arc radiation from the literature. Here we can only

conjecture that the peaky nature of the spectra at $\varphi_x = 90°$ is in part due to the passage of coherent patches of vorticity from the nozzle upper lip over the nozzle lower edge. Thus, the generation of a rather coherent trailing edge noise radiation. This exact mechanism was already postulated for over-the-wing mounted rectangular jets by [86]. It was later further addressed by [87] and [88] in terms of the production of jet-plate interaction tones, through a feedback amplification mechanism. A phenomenon which is not very pronounced in the current configuration; both in static as well as co-flow conditions.

The results of Figure 5-5 clearly identify edge interaction noise as a major source of acoustic production. Phased array maps (not shown here) also reveal important sources of noise at the nozzle's exit plane corners in the frequency range $2\,\text{kHz} \leq f_{c,1/3} \leq 3.15\,\text{kHz}$. This might be related to the specific double-bevel nozzle design used in the current experiment. Further research, especially with regards to the local jet flow characteristics, is required to gain better insight into the specific sound production mechanism of these corner sources. The identified trailing edge noise part of the jet is likely to be shieldable (Shielding Flap, see above).

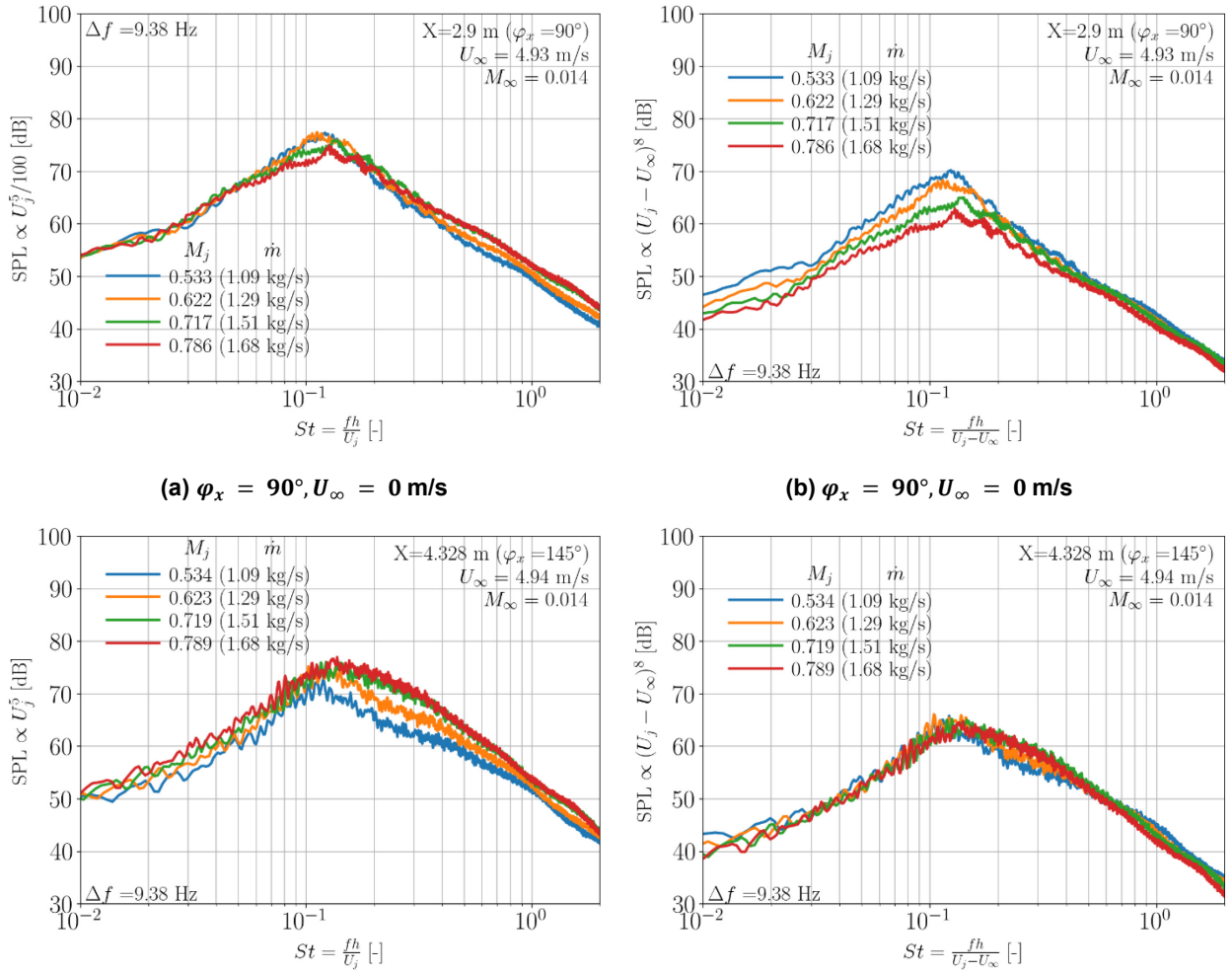


**(a) $\varphi_x = 90°, U_\infty = 0$ m/s** **(b) $\varphi_x = 90°, U_\infty = 0$ m/s**

**(c) $\varphi_x = 145°, U_\infty = 0$ m/s** **(d) $\varphi_x = 145°, U_\infty = 0$ m/s**

**Figure 5-5: Static Jet Noise Radiation for $\varphi_x = 90°, \varphi_x = 145°$ and $\varphi_y = 9.5°$. In-flow measurements, $R = 1$ m.**

### 5.1.2.2 Co-Flow Conditions

For the co-flow case we consider an amplitude scaling based on the theoretical derivation of [89] with a proportionality of the form $L_p \propto \left(1 - U_\infty/U_j\right)^5 U_j^8$. According to the authors, the fifth power dependency accounts for co-flow related effects on sound generation. The eighth power dependency relates to the classical jet noise source mechanism. In Figure 5-6(a), spectral levels are normalized using only the fifth power term. This should remove the co-flow dependency out of the data, leaving only pure jet noise effects. One observes that this kind of scaling is able to bring the peak levels together. However, outside of the approximate peak level range $0.15 < St < 0.25$, the spectra do not scale with a $n = 8$ power exponent as postulated above, but rather with the fifth power of the jet velocity, e.g. Figure 5-6(b). This result implies that at the $\varphi_x = 90°$ emission direction, co-flow effects are contributing only to defining the maximum absolute sound pressure levels. The remainder of the spectrum is defined by the interaction of the jet with the nozzle aft-deck trailing edge. This is consistent with the observations of Figure 5-4(a) and (c).

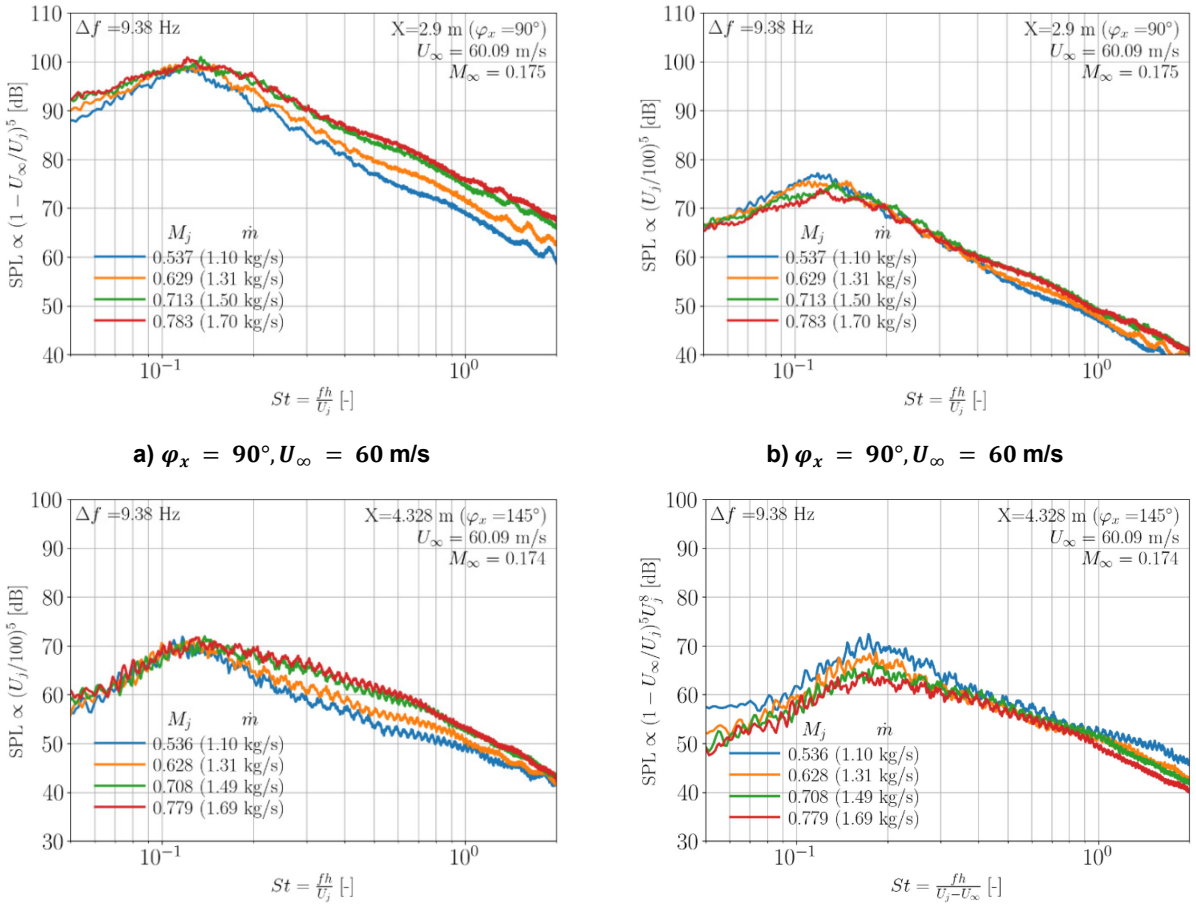


**a) $\varphi_x = 90°, U_\infty = 60$ m/s** **b) $\varphi_x = 90°, U_\infty = 60$ m/s**

**c) $\varphi_x = 145°, U_\infty = 60$ m/s** **d) $\varphi_x = 145°, U_\infty = 60$ m/s**

**Figure 5-6: Effect of Co-Flow on Jet Noise Radiation for $\varphi_x = 90°, \varphi_x = 145°$ and $\varphi_y = 9.5°$. In-Flow Measurements, $R = 1$ m.**

In Figure 5-6(c) and (d) results are given for the $\varphi_x = 145°$ emission angle. The spectral peak is found to be dependent on the jet velocity to the fifth power, e.g. Figure 5-6(c). For $St > 0.25$, the spectra appear to follow the functional dependency proposed by [89], i.e., $L_p \propto \left(1 - U_\infty/U_j\right)^5 U_j^8$, and thus can be understood as jet mixing noise. Based on the above observations, in co-flow conditions and both radiation directions, the main driver to the acoustic production is a flow-edge interaction mechanism. Even in the rear arc direction, classical

jet mixing noise only defines the mid- to high-frequency range of the spectrum. Two physical mechanisms support these findings. First consider trailing edge noise at a nozzle edge. At each line element of this edge the jet turbulence produces trailing edge noise, radiating maximally in the plane perpendicular to the respective line element. For a standard circular nozzle this leads to a circumferential spread of the sound power. The high aspect ratio rectangular nozzle features two long parallel edges, such that the sound generated at all edge line elements gets radiated in the same direction perpendicular to the jet flow direction and the line element. Second, assuming that jet mixing noise as well as nozzle edge noise are present the co-flow reduces jet mixing noise, while it does not reduce trailing edge noise. In this way, edge noise tends to dominate more as the co-flow is increased. It is noted, that in the actual operational range of this vehicle the co-flow Mach number is considerably higher and thus probably even enhancing this effect. This implies that for the type of nozzle and nozzle installation considered herein, an effective noise mitigation strategy should be aiming at reducing the edge noise production.

### 5.1.3 Nozzle Flow

Fabrizio De Gregorio and Carmello Izzo, CIRA

To accomplish the F24 MULDICON nozzle flow characterization some activities have been identified as preliminary to the measurements. In particular, the following activities are necessary:

- Design and realization of a pneumatic control system;
- Design an interface between the seeding generator and nozzle plenum chamber to allow PIV measurements;
- Design of the measurement instrumentation for characterizing the internal pressure distribution and the flow conditions.

#### 5.1.3.1 Pneumatic Control System

The test campaign foresees the investigation of the flow characteristics at different nozzle exit Mach speeds M = 0.5, M = 0.66 and M = 0.74 requiring respectively an input flow pressure of $p_{ext}$ = 4.4 bar, $p_{ext}$ = 6.4 bar, and $p_{ext}$ = 7.4 bar, respectively. The pressurized air available in the transonic wind tunnel building is at a pressure of p = 36 bar and mass flow Q = 26 kg/s. The pneumatic control and measurement system has been designed and it is under construction.

#### 5.1.3.2 PIV Seeding Device

A series of seeding pipes (Figure 5-7(a)) for feeding the nozzle plenum have been designed and will be manufactured together with the nozzle improvements, etc.

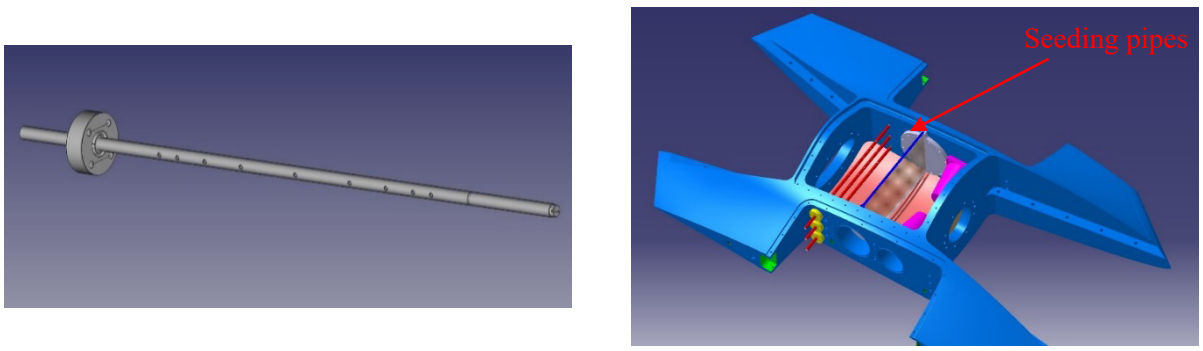


(a) (b)

**Figure 5-7: Seeding Pipe View (a) and Nozzle Plenum with the Seeding Pipes Installed (b).**

#### 5.1.3.3 Nozzle Instrumentation

The pressure distribution along the internal nozzle will be measured by 32 pressure taps (Figure 5-8). The pressure ports will be distributed on the upper and lower surface along the longitudinal plane of symmetry. Spanwise measurement will be considered as well in order to verify possible flow separation inside the nozzle.

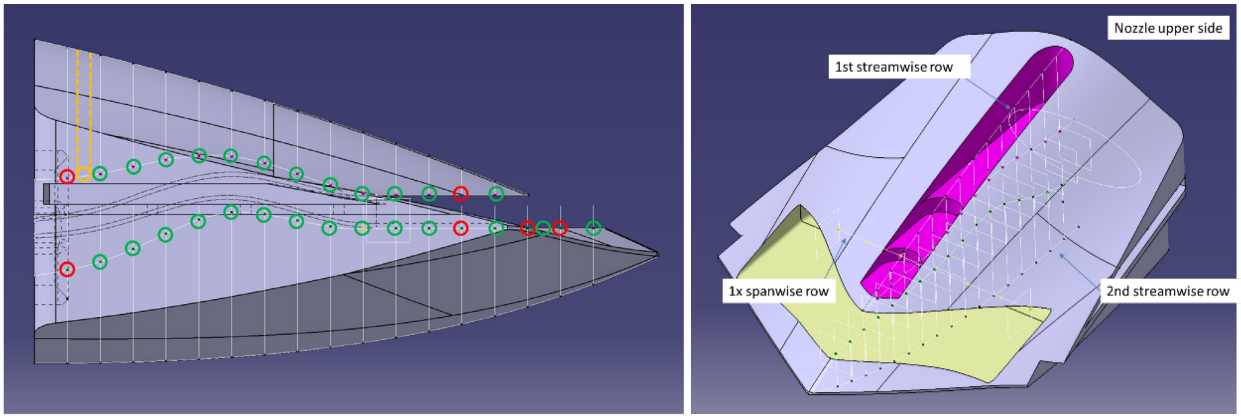


**Figure 5-8: Pressure Tap Locations on the Upper and Lower Nozzle Surface.**

The nozzle flow measurements were delayed due to the unavailability of the pressurized air flow control system as well as the F24 MULDICON model.

## 5.2 EXPERIMENTAL RESULTS OF SHIELDING FLAP INVESTIGATIONS

### 5.2.1 Test Setup and Data Reduction

Florence Hutcheson, NASA

The aeroacoustic effects of the Shielding Flap noise reduction concept described in Chapter 4 were investigated experimentally in the QFF. Schematics of the test setup and model configurations tested are shown in Figure 5-9. The NACA 0012 airfoil with chord of 200 mm was installed in the test section at 0 degree angle-of-attack and a small NACA 0015 airfoil (representing the shielding flap) was installed in the trailing edge region of the NACA 0012 airfoil. Referring to Figure 5-9, four shielding flap configurations were evaluated by varying the shift, overhang and deflection angle of the flap as listed in Table 5-1. A fifth configuration (also depicted in Figure 5-9) was tested where the flap was removed and replaced with a 0.254 mm thick flat plate installed as an extension to the trailing edge of the NACA 0012 airfoil. The NACA 0015 airfoil and flat plate each had a span and chord of 0.91 m and 2.54 cm, respectively. While the surface of the flat plate remained untripped, thin strips of serrated tape (0.127 mm thick) were placed along the span of the NACA 0012 and shielding airfoils to trip the boundary layer and induce its transition to a turbulent state. The strips were positioned at 5% chord on the main airfoil and at approximately 10% chord on the shielding flap.

The microphone measurements were acquired in the midspan plane of the airfoil, one chord away (200 mm) from the NACA 0012 chordline. The survey microphone was traversed in the streamwise direction, up to 200 mm upstream and 400 mm downstream of the airfoil leading edge, while the sound source (laser-induced plasma) was positioned on the opposite side of the airfoil, in the trailing edge region. Each set of in-flow (survey) microphone measurements was acquired with and without the airfoils installed (i.e., for shielded and unshielded conditions). The sound source was positioned, respectively, at 70%, 75% and 100% chord of the

NACA 0012 airfoil (corresponding to streamwise stations, x = 140, 150 and 200 mm). When positioned at 75% and 100% chord, the source was at a normal distance of 25 mm from the airfoil surface, while when positioned at 70% chord, the source was at a normal distance of 40 mm from the airfoil surface. The microphone surveys were performed for three flow speeds (Mach numbers 0, 0.13 and 0.16).

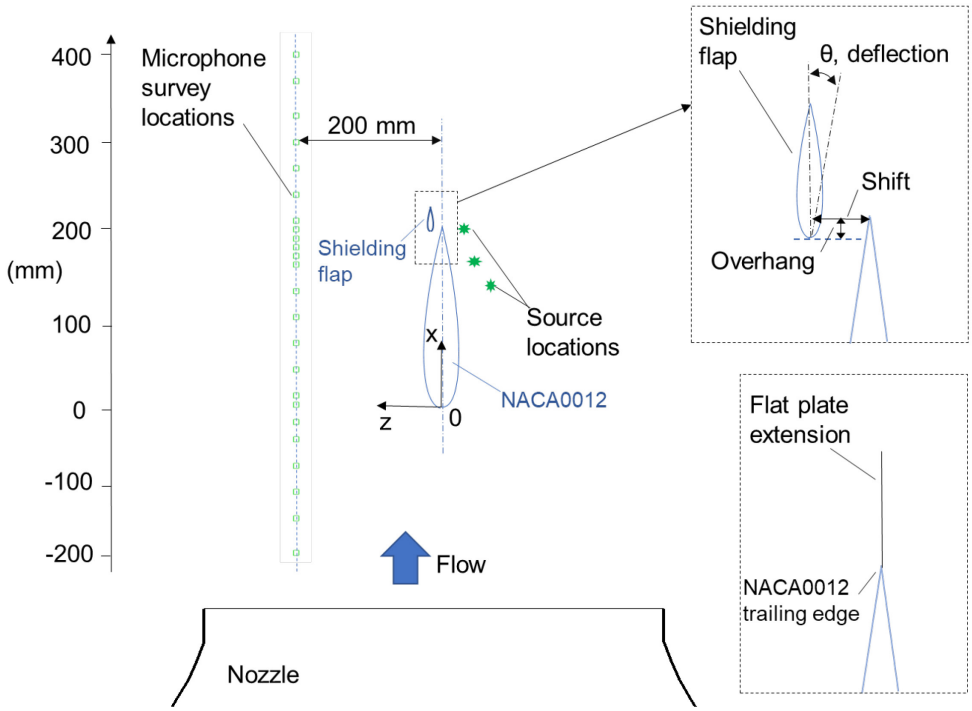


**Figure 5-9: Schematic of QFF Test Setup and of NACA 0012 with, Respectively, the Shielding Flap and Flat Plate Extension.**

**Table 5-1: Test Matrix for NACA 0012 Airfoil with Shielding Flap.**

| Configuration | Shift (mm) | Overhang (mm) | Deflection (degrees) |
|---|---|---|---|
| 1 | 12.7 | 0 | 0 |
| 2 | 12.7 | 0 | 10 |
| 3 | 12.7 | 6.32 | 0 |
| 4 | 12.7 | 6.32 | 10 |

The sound source was generated with a repetition rate of 10 Hz, and the survey microphone response was recorded for 30 s, creating time records of 300 acoustic pulses per data point. The survey microphone data were acquired with a sampling rate of 1.25 MSamples/s. An analog highpass filter was set at 250 Hz and the default lowpass antialiasing filter for the data acquisition cards was used. For the processing of each data point acquired, the time signal was gated with 25% Tukey windows to isolate the portions of the signal that corresponded to the sound that was directly propagating from the source or to the scattered sound that was propagating from components of the model such as leading and trailing edges and the flap gap. This gating rejected reflections from facility surfaces, mitigated facility background and airframe noise, and retained the portions of the time signal that contained the acoustic pulses of interest. Finally, root-mean-squared averaged spectra were obtained from spectra calculated using data blocks that were zero-padded to the number of samples needed to obtain a frequency resolution of 61 Hz.

### 5.2.2 Source Characteristics

Yueping Guo and Florence Hutcheson, NASA

The characteristics of the noise source generated by the laser spark pulse have been extensively investigated and documented in the past, showing that the source is highly coherent, has a small effective size, and closely mimics monopole directivity. These have been very useful in many applications and have enabled the use of ideal monopoles in modeling and predicting the radiated sound. Since computations by PAASc, which is discussed in Section 3.1.1, are used to design the best shielding flap configurations, and the comparison and validation by the test data are an important step in the design process, it is desirable to present the source characteristics, especially in aspects that may have impact on the shielding predictions.

The source characteristics can be shown by the sound pressure levels as a function of frequency for isolated sources without the scattering bodies. Two cases are given in Figure 5-10 for a source at the nominal position of 70% chord downstream of the leading edge of the main airfoil, which is absent in the measurements for the isolated source, showing the sound pressure levels received by the microphones normalized to a distance of 1 meter from the source and without atmospheric attenuation and flow effects, for both the static case (left plot) and the case of M = 0.16 (right plot). The spectra in this figure show peaks at about 30 kHz, and the spectral shapes are well defined, except for frequencies above about 40 kHz. This is due to the use of GRAS microphone nose cones that appear to have a high frequency cutoff at 40 kHz. Thus, the data analysis for both the isolated and the installed case will be limited to below 40 kHz. Below the cutoff, the spectra have smooth variations and the changes in the sound pressure levels between microphone locations are small. The spread of the spectra is an indication of the source directivity. For the static case shown in the left plot, the variations are smaller than about 2 dB, but for the case with mean flow shown in the right plot at M = 0.16, the variations become more noticeable, up to about 4 dB.

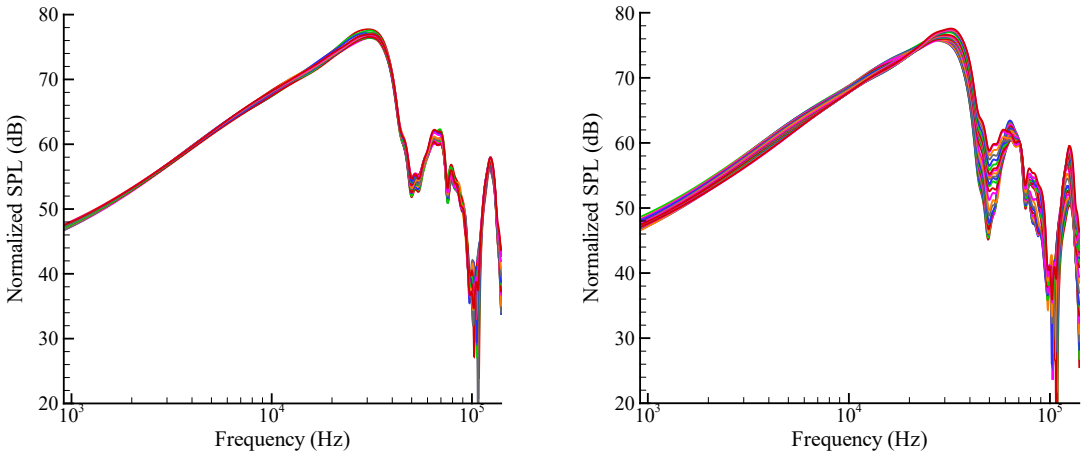


**Figure 5-10: Normalized SPL of Isolated Source for M = 0 (Left) and M = 0.16 (Right).**

For noise shielding investigation, the absolute source amplitude is irrelevant, because it does not affect the amount of noise reduction due to shielding. The source directivity, however, plays an important role because the amplitude of the scattered noise is determined by the noise in the direction from the source to the scattering point, which is in most cases different from the direction from the source to the microphone. To clearly show the source directivity, the source spectrum data are further processed as a function of frequency and polar angle, with the polar angle measured at the source locations with the upstream direction as zero degrees. Spectral levels are normalized by the levels measured at 90 degrees. Two cases are shown in Figure 5-11 with the changes in source directivity plotted as a function of the source polar angle and frequency, for the static case of M = 0 and two nominal source locations, which are identified (see Section 5.2.1) by the chordwise station of the source with

respect to the main airfoil when it is installed in the test section. In the absence of the scattering bodies, the laser spark source can be expected to behave the same, regardless of its location. This is indeed confirmed in Figure 5-11 by the two plots that only show very minor differences. The yellow patch in the right plot at small angles and high frequencies, corresponding to about 2 dB deviation from the monopole directivity, is absent in the left plot because the angular domain for this source does not extend far enough at small angles. For a monopole directivity, which the spark source is designed to mimic, the changes in directivity should be close to zero dB, which is the case for the results shown in the two directivity plots for most of the frequencies and polar angles. The small deviations of up to about 2 dB at small angles and high frequencies by no means make the source directional, and the deviations are well within the acceptable error range for practical applications. It is helpful, however, to note these deviations when the data are used to compare and validate predictions.

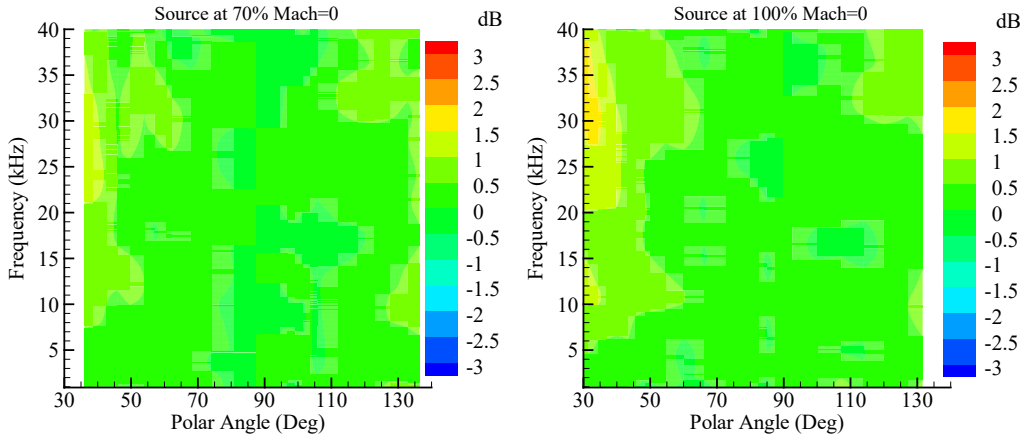


**Figure 5-11: Directivity of Source at 70% (Left) and 100% (Right) of Absent Airfoil Chord for M = 0.**

In the presence of mean flow, the source directivity is shown in Figure 5-12, for M = 0.13 in the left plot and for M = 0.16 in the right plot. The mean flows seem to increase the deviations from the monopole directivity. The increases are both in the amplitudes, up to ±3 dB, and in the polar angle and frequency ranges. As discussed for the static case, the increases in the deviations are still small compared with the magnitudes of the shielding for practical applications. The deviations, however, become important when the data are compared with predictions using ideal monopole sources.

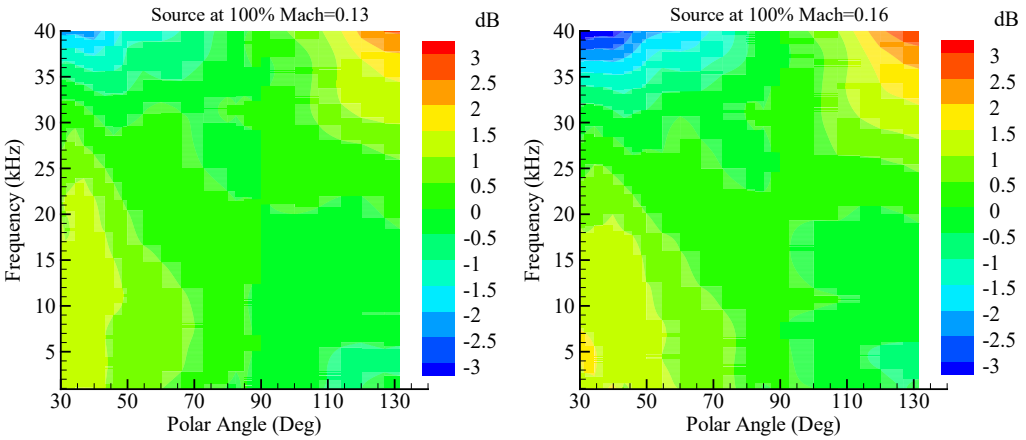


**Figure 5-12: Source Directivity for M = 0.13 (Left) and M = 0.16 (Right).**

### 5.2.3 Shielding Results

Yueping Guo, NASA

The effects of shielding are measured by the differences in sound pressure levels between the case with the scattering geometry and the case of an isolated source in an empty tunnel. The spectral shapes and the directivity patterns have been discussed in the previous section. Some examples of the spectra for the scattered sound are shown in Figure 5-13, where the sound pressure levels are plotted as a function of frequency in the range below 40 kHz to avoid the measurement error at higher frequencies. The frequency variable is plotted in linear scale, instead of the conventional logarithmic scale, to clearly show the interference patterns resulting from various scattering paths. The results are for the extension plate configuration with the source at the position of 70% chord from the main airfoil leading edge, without mean flow. All the measurements are one airfoil chord length away from the airfoil on the opposite side to the source. The four curves are for four streamwise locations, with the red curve for the position that is one airfoil chord upstream of the airfoil leading edge, the green curve for the position that is aligned with the airfoil leading edge, the purple curve for the position that is aligned with the airfoil trailing edge, and the blue curve for the position that is one airfoil chord downstream of the airfoil trailing edge.

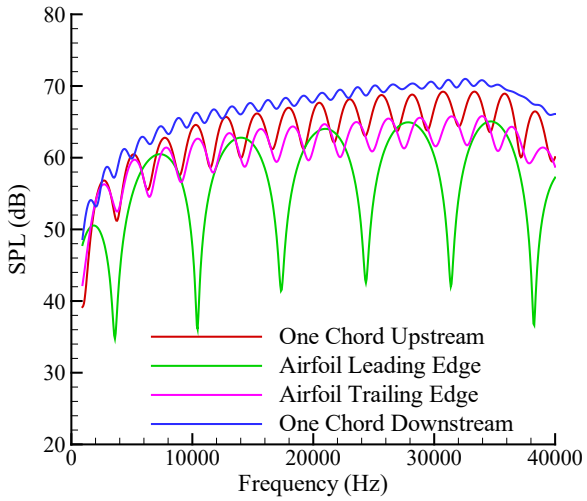


**Figure 5-13: SPL for Extension Plate with the 70% Source Location in Static Medium.**

A dominant feature of the scattering process is the strong interference between the two diffracted pressure components from the highly coherent source, one from the leading edge of the airfoil and the other from the trailing edge of the attached plate, which produces the sharp dips and the broad peaks in the spectra. The interference also occurs in the spatial domain, making the sound levels highly dependent on the measurement location. This calls for careful considerations in defining the metric to assess the effects of shielding, because the result for a single frequency band at a single measurement location can easily mask the true scattering effects. Such a result can also complicate the comparison with a prediction if the prediction is done for a single frequency at a mathematical point. Since the spectra of the source without the scattering body are smooth, as shown in Figure 5-10 in the previous section, the effects of the scattering, measured by ΔSPL, can be expected to also show the interference patterns. This is shown in Figure 5-14, for the same case and the same measurement locations as in Figure 5-13 with the SPL data converted to ΔSPL.

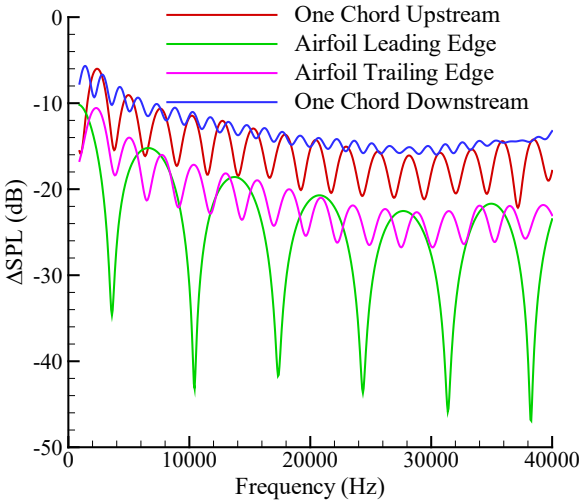


**Figure 5-14: ΔSPL for Extension Plate with the 70% Source Location in Static Medium.**

The scattering process can also be affected by the presence of mean flows. Some examples are shown in Figure 5-15, which is for the same configuration and the same four measurement locations as in Figure 5-13. The mean flow only slightly changes the overall amplitudes of the scattered noise but can noticeably shift the interference patterns, more so as frequency increases. This shift in the interference patterns makes it difficult to examine the mean flow effects at fixed frequencies, because the offset in the spectral shapes can make the amplitudes at fixed frequencies vary without clear trends. Even for the spectral peaks, the variations in the peak levels do not follow any clear trends, because the mean flow also shifts the interference patterns in the spatial domain.

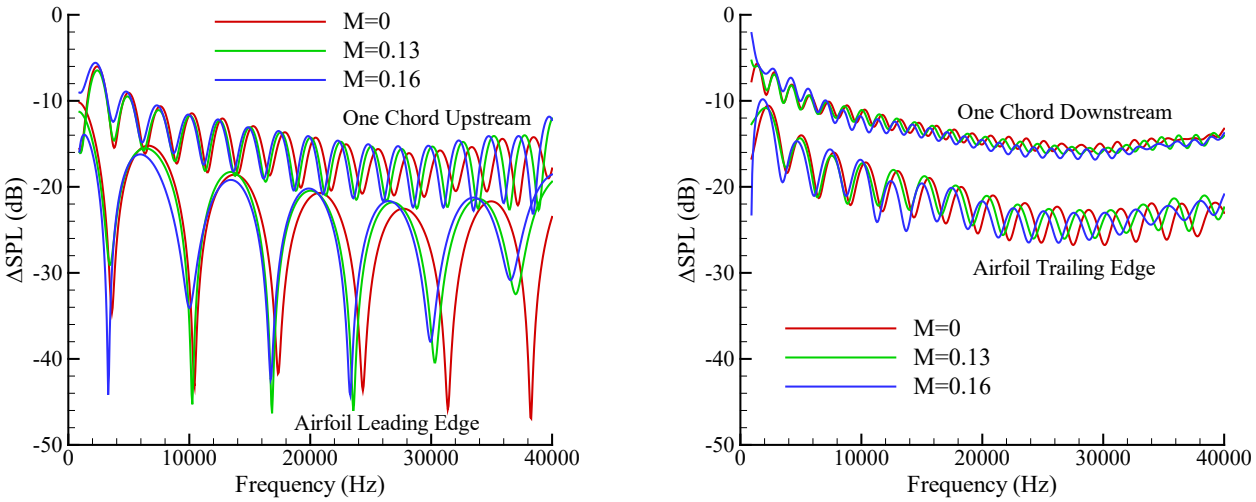


**Figure 5-15: Effects of Mean Flow on ΔSPL for Extension Plate with the 70% Source Location.**

For scattering mechanisms, the baseline and the extension plate configuration are similar to each other. In both cases, the scattered sound is given by two diffraction components, one from the smooth geometry diffraction at the airfoil leading edge and the other from the sharp edge diffraction at the trailing edge of either the airfoil or the attached plate. The configurations with shielding flaps, however, involve more scattering from multiple edges, some of which may block the diffractions from others. This leads to more

complex interference patterns, as shown in Figure 5-16. for two sample configurations. Referring to Figure 5-9, the flap is shifted 0.5 inches towards the microphone and without overhang. For the scattered pressure spectra shown in the left plot, the flap is not deflected (i.e., θ is 0°), while for those shown in the right plot, the flap is deflected 10 degrees towards the main airfoil (i.e., θ is -10°). In both cases, the source is at the 70% chordwise location with respect to the main airfoil and the mean flow Mach number is zero.

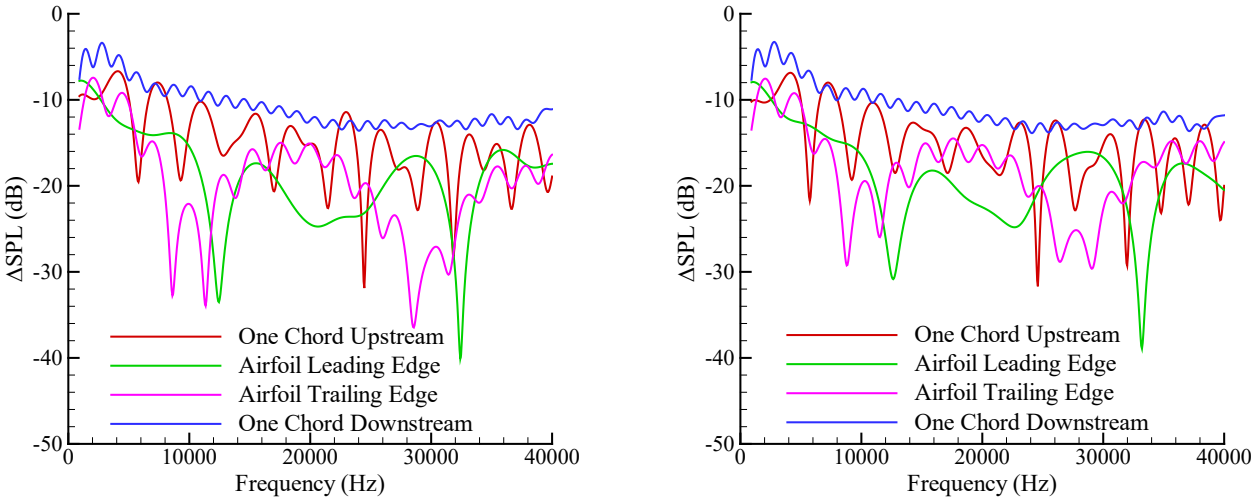


**Figure 5-16: ΔSPL for Shifted Flap with the 70% Source Location in Static Medium with Flap Angle at 0 (Left) and -10 Degrees (Right).**

A drastic difference is observed between the interference patterns displayed in Figure 5-14 and Figure 5-16, as they change from a somewhat ordered pattern for the extension plate to a very irregular variation with no clearly discernable trends for the shifted flap. Of the four measurement locations shown in Figure 5-16 and Figure 5-17, the only exception is when the microphone is positioned one main airfoil chord length downstream of the airfoil trailing edge. This is because the scattering at this location is dominated by the diffraction from the trailing edge of either the flap or the attached plate, which are both sharp edge diffraction. The interferences at this location are weak because it is far away from other edges. The weak interferences also manifest themselves by the small magnitudes of variations between the dips and peaks in the spectra. By comparing the two plots in Figure 5-16, the flap deflected at a negative angle produces slightly lower noise levels, which is intuitively expected because the trailing edge of the flap makes a slightly larger shadow zone when the flap is at a negative angle.

The highly coherent source and the multiple paths of scattering lead to rapid variations in both frequency and spatial domains, which makes it difficult to compare results from different configurations based on single frequency band and single measurement location. A way to analyze the data, without being buried in the rapid variations from frequency to frequency and from location to location, is to compare shielding effect contour maps between different configurations. One such comparison is given in Figure 5-17, between the baseline configuration with the NACA 0012 airfoil alone (left plot) and the extension plate configuration (right plot) for static medium and the source located at 70% chord of the main airfoil. In Figure 5-17 and as depicted in Figure 5-9, 0 and 0.2 m correspond to the streamwise positions of, respectively, the leading edge and trailing edge of the NACA 0012 airfoil. The color contours are the levels of ΔSPL (i.e., shielding) as a function of microphone streamwise position and frequency. A qualitative conclusion can be easily drawn from the overall comparison, in that the presence of the extension plate provides more shielding than the baseline configuration by extending the shadow zone, and hence, lowering the noise levels. Since the test setup is very idealized with a simple source and a canonic scattering geometry, qualitative conclusions such as this should be sufficient because the detailed quantitative results are not likely to be transferable to any real vehicle.

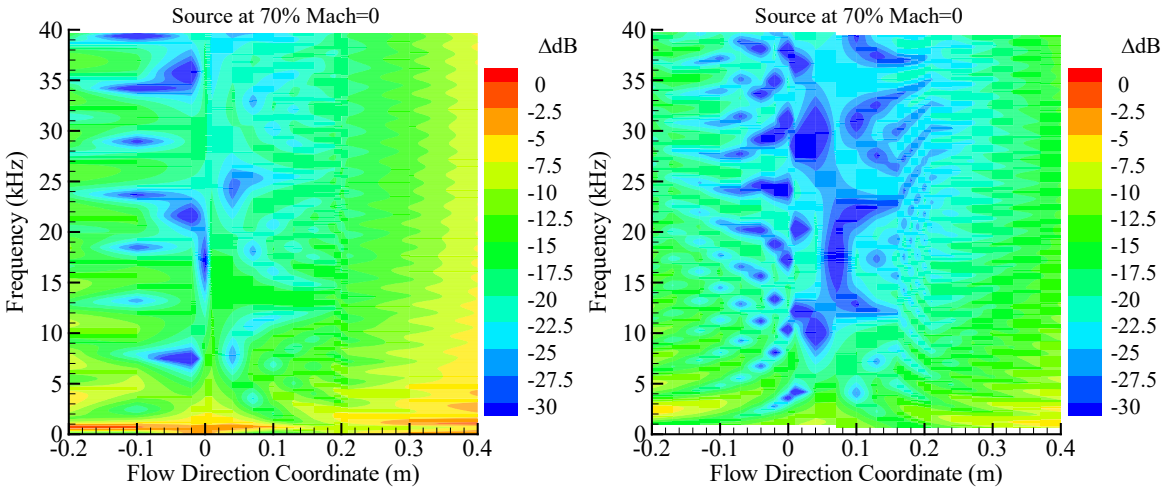


**Figure 5-17: Comparison between Baseline (Left) and Extension Plate (Right) for M = 0 and the 70% Source Location.**

The contour maps can also be used for detailed quantitative analysis, if needed, for validating prediction tools, for example. The rapid variations in both frequency and measurement location are clearly shown in the contour maps. It is interesting to note that the highly oscillatory patterns are in the regions either upstream or downstream of a small region in the shadow zone. In this small region, the shielding effects are strong and the variations in frequency are gradual. This is further shown in Figure 5-18 where ΔSPL is displayed as a function of frequency for M = 0 and the source located at 70% chord of the main airfoil. For the baseline case, the measurement streamwise location is at x = 0 and for the extension plate case, the location is a little more downstream at x = 0.07 m. The reason for the gradual variations observed is that the two propagation paths, one through the leading edge of the airfoil and the other through the trailing edge of either the airfoil or the attached plate, have approximately equal lengths. When the two propagation distances are equal, the phase functions of the two scattering components are the same so that there is little interference between the two. The equal-distance locations for the two configurations shown in the figure are different because the extension plate extends the trailing edge of the scattering geometry further downstream, and thus, moves the equal-distance point further downstream, in comparison with the baseline. This also implies that comparisons of shielding results between different scattering configurations at the same measurement location may not be the most appropriate or straightforward. For example, if the same location of x = 0 was chosen for comparison between the baseline and the extension plate configuration, the gradual red curve for the baseline would be compared with the oscillatory dashed green curve in the figure, leading to the conclusion that the extension plate would reduce noise at some frequencies but increase noise at some other frequencies.

A comparison similar to that shown in Figure 5-17 is presented in Figure 5-19. Shielding levels measured for the baseline configuration with the NACA 0012 airfoil alone are shown in the left plot and those obtained for the extension plate configuration are shown in the right plot. The mean flow Mach number at M = 0.16. The two plots in the figure again show the enhanced shielding effects of the extension plate configuration from the baseline. By comparing Figure 5-17 and Figure 5-19, it is seen that the flow effects are clearly very small, and probably small enough and irregular enough to not have any practical significance.

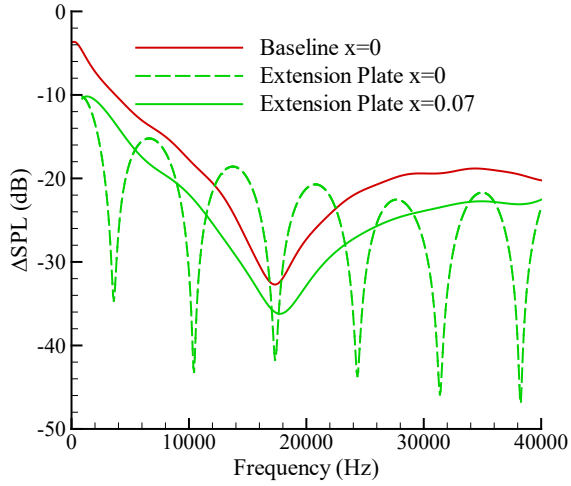


**Figure 5-18: Shielding Effects in Deep Shadow Region for M = 0 and the 70% Source Location.**

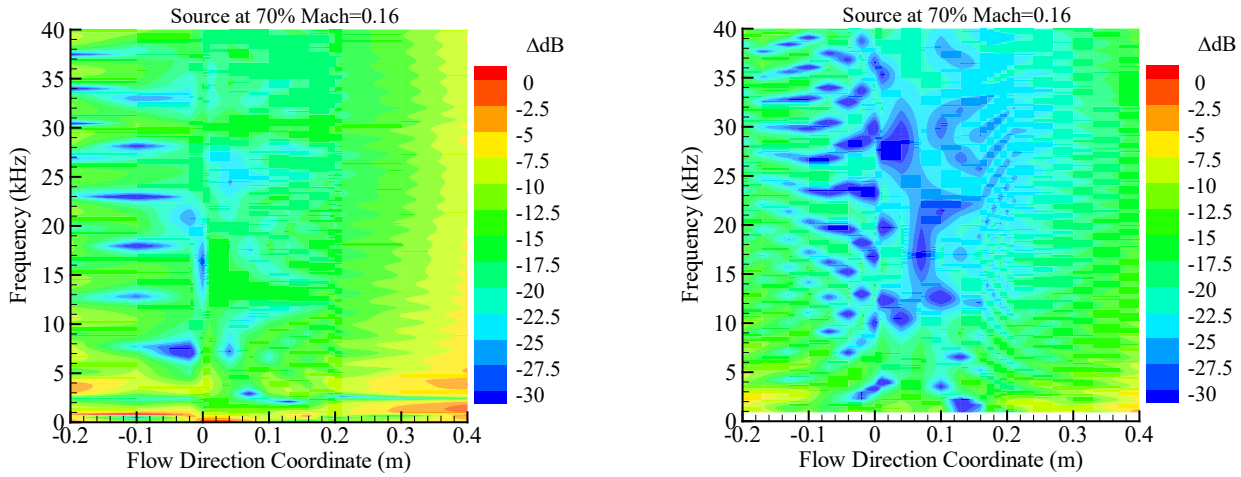


**Figure 5-19: Comparison between Baseline (Left) and Extension Plate (Right) for M = 0.16 and the 70% Source Location.**

The small mean flow effects are also illustrated in Figure 5-20 for the shifted flap configuration at zero flap angle and zero flap overhang (see Figure 5-9). Measured shielding levels for M = 0 and M = 0.16 are shown in the left plot and right plot, respectively. The source is again located at 70% chord of the main airfoil. When comparing Figure 5-19 and Figure 5-20, it is seen that the scattering patterns are organized very differently. In Figure 5-20, the dips and peaks, upstream and downstream of the nominal deep shadow locations, are no longer along the flow direction, and in the deep shadow zone, the variations with frequency become less gradual and consist of more than one low-level point. This is due to the multiple diffractions from the two scattering bodies in the geometry (the flap and the main airfoil), as well as the partial blocking of some diffractions by the flap. The overall or qualitative shielding effects provided by this shifted flap configuration seem to be less than those observed with the extension plate configuration. However, the scattering pattern associated with the shifted flap configuration may be beneficial in practical applications. Thus, referring to Figure 5-20, there is a curved band in blue color in the contour maps, starting at x = 0.1 and 5 kHz and curving up to the point of x = 0.3 and 40 kHz. Within this band, noise is reduced in comparison with the extension plate case. This can be a desirable feature because this band is mostly downstream of the main airfoil in the aft quadrant where noise reduction is usually difficult to achieve.

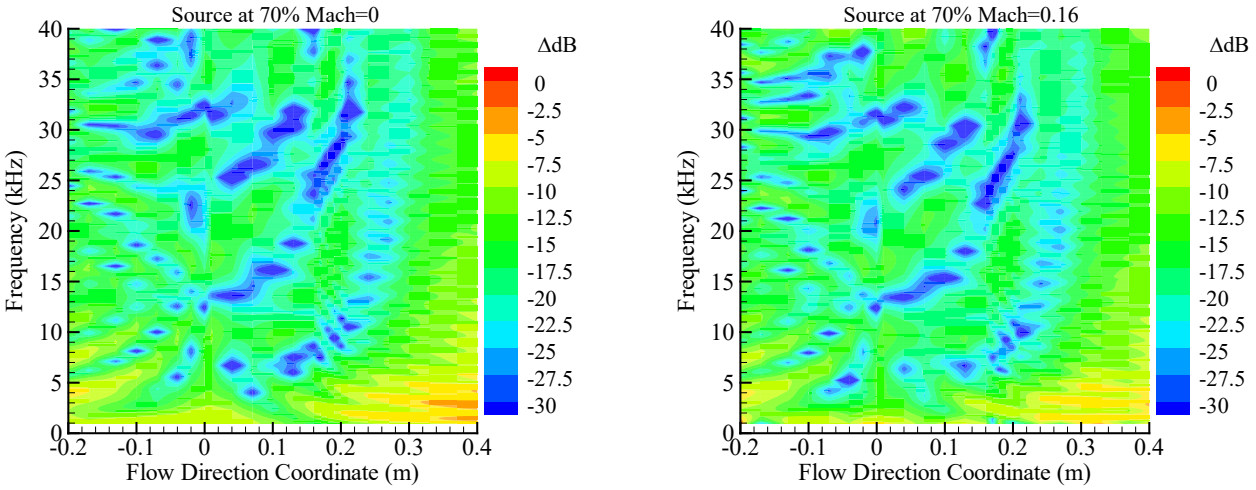


**Figure 5-20: Comparison between M = 0 (Left) and M = 0.16 (Right) for Shifted Flap at Zero Flap Angle, Zero Overhang, and the 70% Source Location.**

For the extension plate configuration, the different source locations may lead to a shift of the shadow zone on the opposite side of the geometry but not alter the main scattering characteristics, because a change in source location only changes the distances from the source to the two diffraction edges, while the edge diffraction mechanisms remain the same. For the shifted flap case, however, the source position near the trailing edge of the main airfoil may have quite different scattering features from other source locations, because the gap between the flap and the main airfoil can leak noise from the source side to the microphone side, including direct radiation from the source, as well as diffractions by the edges in this region. The leakage is directed towards the region upstream of the main airfoil trailing edge and can also interfere with other components from other edge diffractions to form scattering patterns in this region that are different from those generated with other source locations, for the same scattering geometry. These effects are shown in Figure 5-21, which compares the shielding levels measured for the extension plate and the shifted flap configurations when M = 0.16 and the source is at the 100% chordwise location (i.e., aligned with the main airfoil trailing edge). For the shifted flap configuration, the flap deflection angle and the flap overhang are both zero. Indeed, the scattering patterns for the shifted flap with a source near the trailing edge of the airfoil and shown in the right plot of Figure 5-21, are very different from those for the extension plate case (left plot in Figure 5-21). Comparing the right plot in Figure 5-20 to the right plot in Figure 5-21, it is also seen that for the same model configuration, the scattering pattern also changes with the source location. Noticeably, the leakage effects increase the noise in many patches in the contour map in the region upstream of the main airfoil trailing edge. Importantly, the noise reduction indicated by the curved band of blue color in the downstream region, discussed in the previous paragraph, still occurs for this trailing edge source.

One way to enhance shielding is to deploy a flap at a negative angle with the flap trailing edge rotated towards the source side of the scattering geometry, provided that no additional noise sources are produced, and no other design criteria are compromised by such a deployment. The shielding effects for the shifted flap at -10 degrees are shown in Figure 5-22 for M = 0.16 and zero flap overhang, respectively for the 70% (left plot) and the 100% (right plot) source location. By comparing the left plot in this figure with the right plot in Figure 5-20 the negative flap angle increases the shielding effects slightly, which may not be practically significant. By comparing the right plot in this figure with the right plot in Figure 5-21, the noise in the region upstream of the main airfoil trailing edge is increased, although only slightly and it is not likely to be of practical significance. This increase in noise is probably due to the small flap angle that only results in a small increase of the shadow region, and the dominant feature is the gap leakage that is not significantly affected by the flap angle.

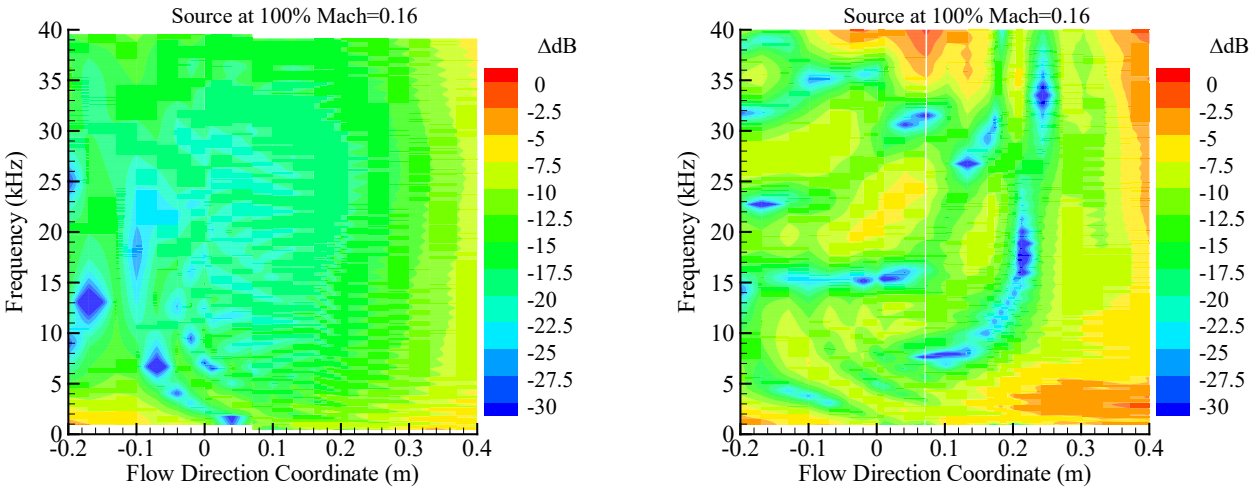


**Figure 5-21: Comparison between Extension Plate (Left) and Shifted Flap (Right) for M = 0.16 and the 100% Source Location.**

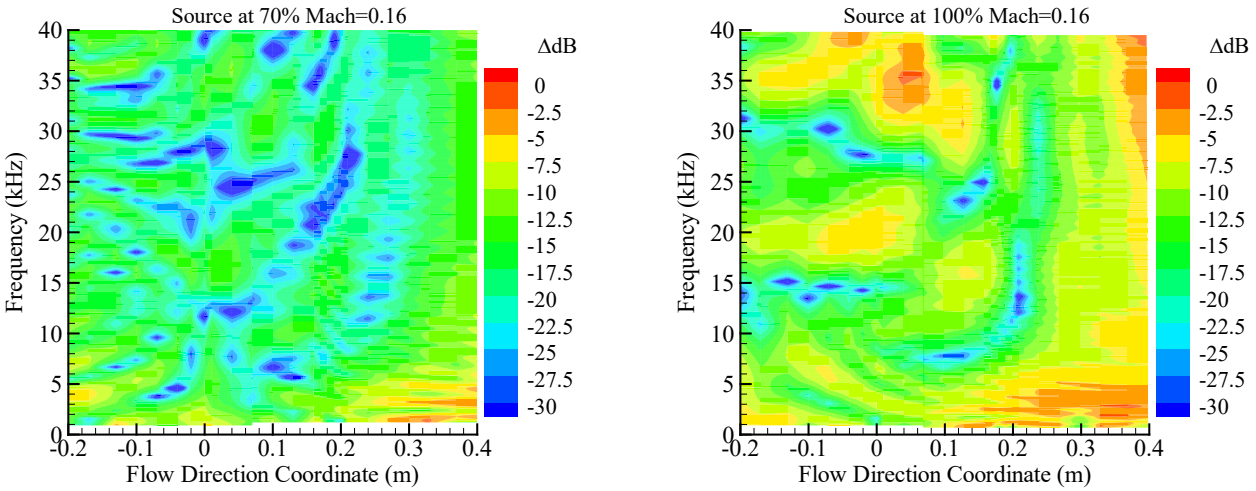


**Figure 5-22: Comparison of Different Source Locations for Shifted Flap at -10 Degrees.**

To reduce the noise in the region upstream of the main airfoil trailing edge, the gap size should be minimized and/or the local geometry in the gap should be designed to minimize noise leakage through the gap. A positive flap overhang may be one way to achieve this. A configuration is tested with a flap overhang of 6.32 mm. Results are shown in Figure 5-23, respectively for the source position of 70% and 100%, both at M = 0.16 and zero flap angle. By comparing the left plot in Figure 5-23 with the right plot in Figure 5-20 the flap with overhang is seen to enhance the shielding, especially in the region upstream of the airfoil trailing edge where the leakage seems to be stopped. With the source at the 100% chordwise position, the comparison between the right plot in Figure 5-23 and the right plot in Figure 5-21 indicates that the changes are minor without noticeable shielding enhancement. This is probably because the dominant leakage in the gap comes from direct source radiation, which the flap overhang cannot stop.

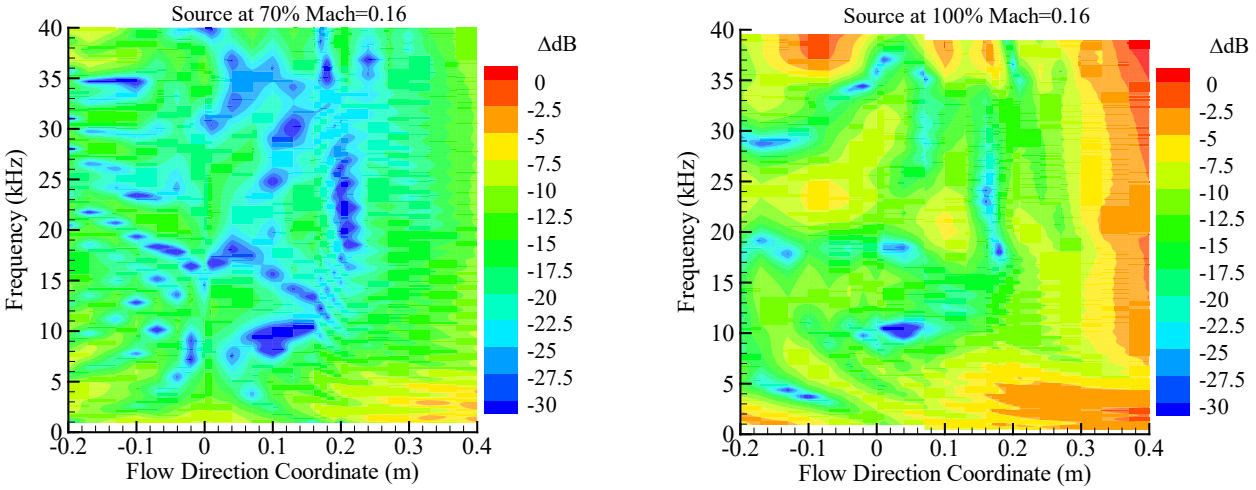


**Figure 5-23: Scattering Effects of Shifted Flap with 6.35 mm Overhang for Different Source Locations.**

# Chapter 6 – NUMERICAL ANALYSIS AND VALIDATION

**Yueping Guo**
NASA
UNITED STATES

**Patrick Zimmermann**
Airbus Defence and Space
GERMANY

**Mathieu Lorteau**
ONERA
FRANCE

**Mattias John Quas, Shia-Hui Peng and Samuel Gottfarb Bart**
FOI
SWEDEN

## 6.1 NASA NUMERICAL ANALYSIS AND VALIDATION

Yueping Guo, NASA

NASA's numerical analysis focuses on the design of the shielding flap to optimize noise reduction and follows a progressive process of parametric studies, using the PAASc prediction capability discussed in Section 3.1.1. The design process starts with the simple geometry of a baseline NACA 0012 airfoil with shielding flaps, then proceeds to a two-dimensional cross-section model of the MULDICON concept with shielding flaps. A design of the shielding flaps for the full three-dimensional MULDICON configuration is planned but has not been completed at the time of this report.

### 6.1.1 Shielding Flap Results for NACA 0012 Airfoil

The design using the basic NACA 0012 airfoil is coordinated with the experimental effort in NASA QFF, discussed in Section 5.2, with the numerical analysis conducting many parametric computations to select the most promising configurations for the QFF tests. The computational setup consists of the same layout and dimensions as in the tests with the NACA 0012 airfoil and the shielding flaps. The measurement locations are distributed along a line in the flow direction, at the midspan and on the shadow side of the airfoil. The measurement locations extend from two chord lengths of the main airfoil upstream of its leading edge to two chord lengths downstream of its trailing edge. The geometry is illustrated in Figure 6-1. The airfoil has a chord length of 200 mm and a trailing edge thickness of 0.254 mm. The source is assumed to be a coherent point monopole source and can have five positions. In the flow direction, the five positions are respectively at 0%, 50%, 70%, 75% and 100% of the main airfoil chord length, measured from its leading edge, and the source positions are 25 mm above the airfoil surface, except for the one at the 70% chordwise location that is 40 mm from the surface. In Figure 6-1, the source shown is at 70% of the airfoil chord length from its leading edge. The design parametric computations are done with three values of the mean flow Mach number, M = 0, M = 0.13 and M = 0.16, but the results are presented for static medium, because the effects of the mean flow may change the quantitative results but not the qualitative conclusions that are the basis of the design optimization.

Two types of shielding flaps are used in the computations, one being a flat plate and the other a NACA 0015 airfoil. Both have a chord length of 25.4 mm and a trailing edge thickness of 0.254 mm that is the same as the trailing edge thickness of the main airfoil. For each type of flap, three parameters are varied. They are the flap overhang in relation to the trailing edge of the main airfoil, the shift of the flap towards the microphone side, and the flap angle, defined positive when the flap is rotated towards the microphones. The values of these parameters are given in Table 6-1, together with the values of other parameters to show the complete computation matrix.

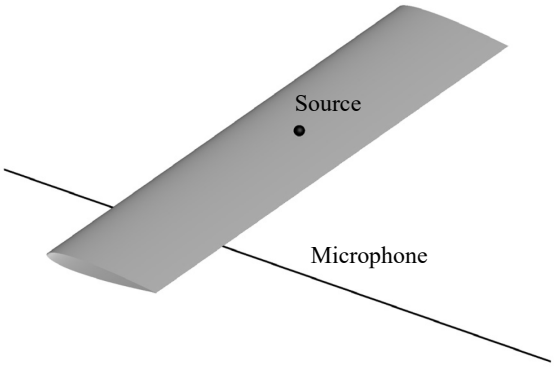


**Figure 6-1: Illustration of Computation Setup for NACA 0012 Flap Design.**

**Table 6-1: Computation Matrix for NACA 0012 Airfoil with Shielding Flap.**

| Parameter | Values |
|---|---|
| Source Position (%) | 0, 50, 70, 75, 100 |
| Mach Number | 0, 0.13, 0.16 |
| Flap Type | Plate, NACA 0015 Airfoil |
| Overhang (mm) | -6.35, 0, 6.35, 12.7, 19.05 |
| Shift (mm) | 0, 3.175, 6.35, 9.525, 12.7, 15.875, 19.05 |
| Flap Angle (Deg) | -10, 0, 10 |

From this large computation matrix, a subset of configurations is selected to present the results and analyses, which are shown in Figure 6-2, for the two types of flaps with three flap positions, namely, an extension position with the flap attached to the main airfoil, a gapped position where the flap is moved in the downstream direction to create a gap of 6.35 mm between the trailing edge of the airfoil and the leading edge of the flap, and a shifted position with the flap shifted towards the microphones by an amount of 6.35 mm.

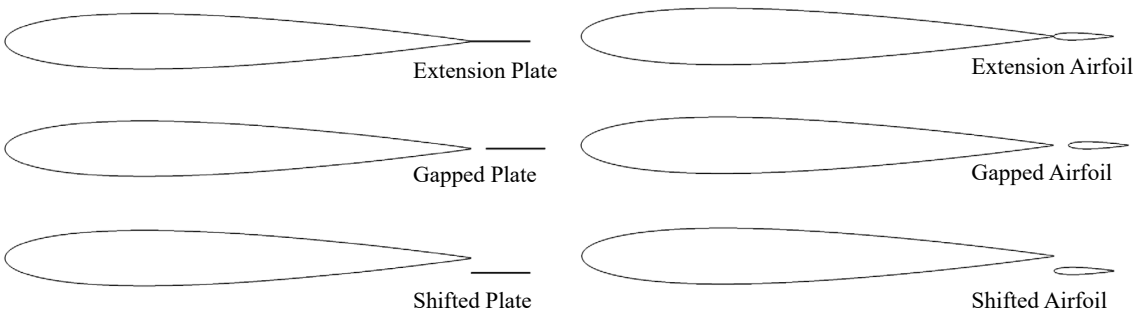


**Figure 6-2: Configurations for Shielding Flap Computation with NACA 0012 Main Airfoil.**

The effects of the extension flap on noise shielding are shown in Figure 6-3 where the ΔSPL on the vertical axis is the sound pressure level for the scattering case minus that for the isolated source, showing the shielding effects as negative values, and the horizontal axis is the coordinate in the flow direction normalized by the chord length of the main airfoil. Thus, the leading edge of the main airfoil is at zero and its trailing edge is at one. For comparison, the results for the main airfoil alone are also shown in the plots. Since the flaps in these cases effectively increase the chord length of the scattering geometry, the results and physics of the scattering are simple. The extension flaps simply move the trailing edge diffraction to a different location further downstream. The overall amplitudes in the upstream microphone positions (upstream of the mid chord of the main airfoil) are basically the same, because this spatial range is dominated by the diffraction from the main airfoil leading edge, which is the same for all three cases. The shift of the dips and peaks in this range from the case of the main airfoil alone to the cases of extension flap is due to the changes from the trailing edge diffraction, which is more clearly shown in the downstream range of the results, where the extension flap increases the shadow region, and thus lowers the noise amplitude from the case of the main airfoil alone at fixed locations. The difference between the extension plate and the extension flap in this spatial range is due to the diffraction at different trailing edge angles.

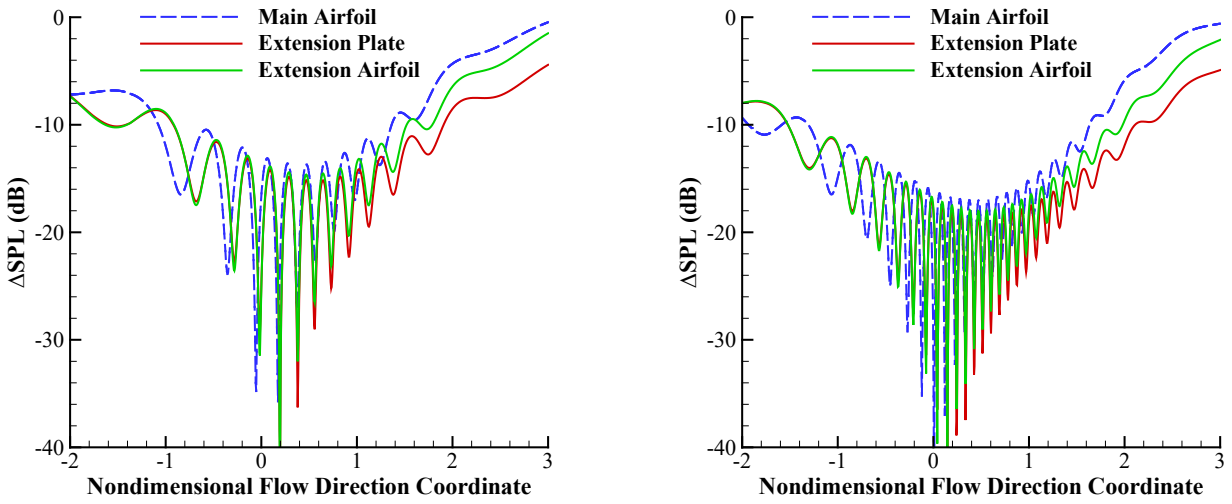


**Figure 6-3: Effects of Extension Flap on Noise Shielding for 10 kHz (Left) and 20 kHz (Right).**

For the gapped flaps, the edge diffraction occurs at four edges, which still follows the same diffraction physics, with the gap allowing the diffracted noise to reach the shadow and the partially insonified region. Thus, an increase of noise in some spatial range is expected. This is indeed confirmed by the results shown in Figure 6-4, where the noise in the region close to and slightly downstream of the trailing edge of the main airfoil is higher than in the case of the main airfoil alone, due to the combined effects of multiple edge diffraction and gap leakage. The gapped airfoil flap suffers more leakage of noise into the shadow region and the partially insonified region, in comparison with the gapped plate flap, because there is more scattering off the smooth leading edge of the flap.

When the flaps are shifted towards the microphones, the noise reduction due to shielding is increased in the region downstream of the main airfoil trailing edge, as shown in Figure 6-5. Upstream of the main airfoil trailing edge, the flaps do not block the edge diffraction so that the main airfoil scatters the noise in the same way as an airfoil without a flap, leading to almost identical results in this region for all three cases shown in the figure.

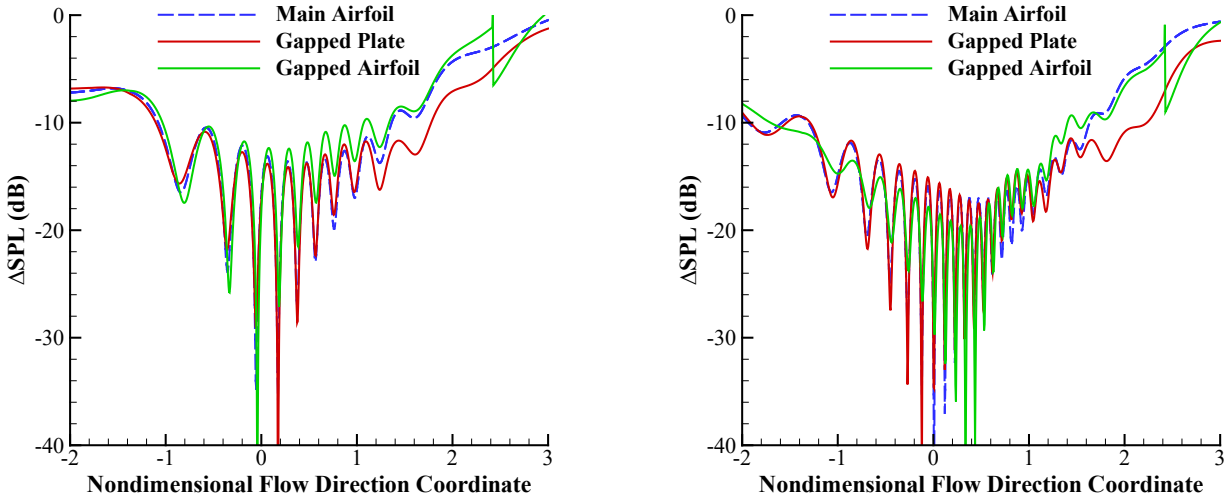


**Figure 6-4: Effects of Gapped Flap on Noise Shielding at 10 kHz (Left) and 20 kHz (Right).**

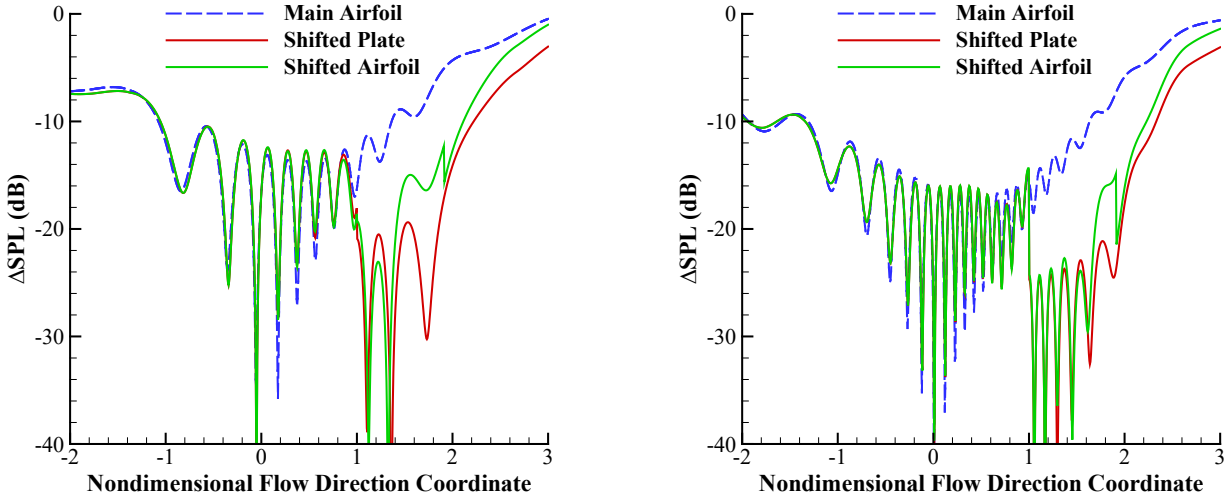


**Figure 6-5: Effects of Shifted Flap on Noise Shielding at 10 kHz (Left) and 20 kHz (Right).**

The shifted flap configuration results in a noise reduction downstream because the flap blocks the diffraction from the main airfoil trailing edge, which is a major contributor of noise in this region. With this blockage, the noise in this region mainly comes from the trailing edge of the flap, which is weaker than the main airfoil trailing edge diffraction or that of the extension flap connected to the main airfoil, because of the smaller dimension of the flap when it is not connected to the main airfoil. The scattering physics is illustrated in Figure 6-6. For an extension flap, the flap effectively increases the dimension of the scattering geometry, by 1/8 of the main airfoil chord in this case. Thus, the relative diffraction strength can be regarded as 9 units, or as being unchanged at 8 units from the baseline airfoil if the total chord is much larger than the wavelength so that the diffraction is within the limit of geometric acoustics. This strength is proportional to the noise diffracted to the far field. In comparison, when the flap is not connected to the main airfoil, the total diffraction strength of 9 units is divided between the main airfoil and the flap, approximately 8 and 1 units respectively, because the flap chord is smaller than the wavelength, and thus, has not achieved the strength of geometric diffraction. For the shifted flap, the diffraction proportional to 8 units is blocked by the flap and the remaining noise to the far field is only proportional to one unit, a much weaker contribution. The method

of geometric acoustic diffraction cannot capture this low frequency, or large wavelength, feature. The method in PAASc has a correction to account for this based on the diffraction physics.

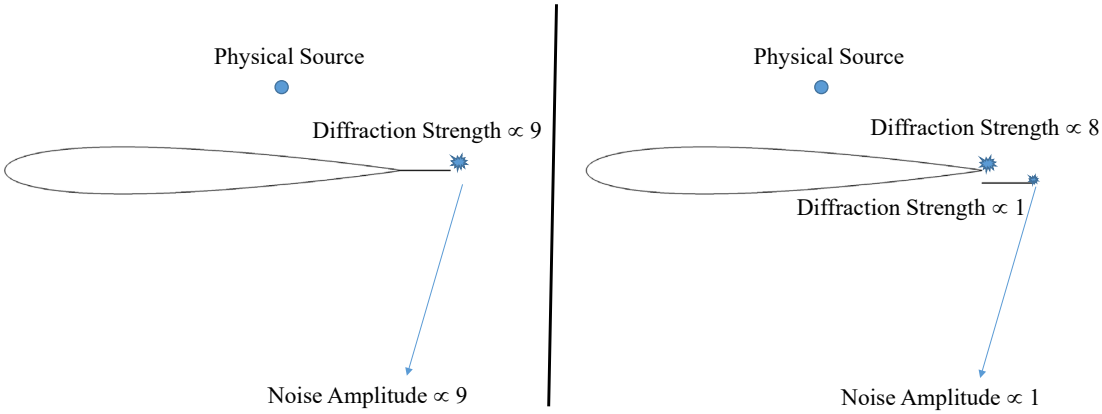


**Figure 6-6: Illustration of Diffraction Physics for Extension Flap and Shifted Flap.**

The results given in this section are a subset of the large matrix of parametric studies, designed to select the best potential shielding flap configuration for noise reduction. The parametric studies involve all the combinations of the parameters listed in Table 6-1, for a total of 3150 configurations. From the parametric studies, all shielding flap configurations have been shown to be efficient in reducing more noise, in comparison with the baseline airfoil, by increasing the shadow zone, which is intuitive because the flap increases the dimension of the scattering geometry. However, the additional noise reduction, from the baseline and between the flap configurations, is not uniform in space and in frequency. This is because the additional noise reduction can be partially or completely offset by some features of the individual configurations, in certain ranges in space and in frequency. The leakage from the gap between the flap and the main airfoil is an example, because of which, the noise levels can revert to the baseline levels at some angles. In summarizing all the configurations, the shifted flap with zero or positive angle and a small overhang seems to be the best configuration. It extends the shadow zone in the same way as other configurations, which is the most beneficial feature of shielding flaps, but with the extra benefit of blocking the propagation from the source to the microphones through the gap, minimizing the gap leakage of the diffraction by the flap leading edge, and shielding the diffraction from the main airfoil trailing edge.

The noise reduction potential by shielding flaps is most beneficial in the aft quadrant downstream of the main airfoil trailing edge. This region covers a portion of the shadow region and a portion of the partially insonified region. In aircraft noise shielding, because the engines are usually located near the trailing edges, noise shielding in the aft quadrant is usually not efficient. Thus, additional ways such as shielding flaps may be needed to help to achieve more noise reduction. The airfoil/flap geometry studied in this section is not meant to simulate any realistic vehicle. The scattering effects of a vehicle are highly dependent on the scattering geometry, as well as the source location, which is why the design process is planned to progress towards the MULDICON geometry. An intermediate step is described in the next section.

### 6.1.2 Shielding Flap Results for MULDICON Cross Section Model

As an intermediate step before the design of shielding flaps for the full configuration MULDICON vehicle, a cross-section model is considered for parametric studies, which uses the midspan cross section to construct a spanwise-invariant geometry. The measurement locations for the computations are on an arc of 10-meter radius, illustrated in Figure 6-7. The arc is on the lower side of the vehicle and its center is at the origin of the coordinate system for the scattering geometry, which is chosen to be the leading edge of the vehicle. The polar angle is defined with the upstream direction to be zero degree.

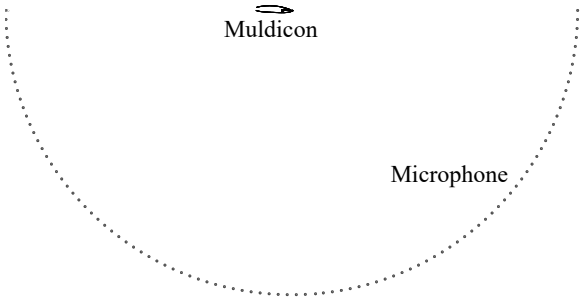


**Figure 6-7: Illustration of Microphone Positions for Computations.**

The scattering geometry is shown in Figure 6-8, together with four configurations used in the computations. The first is the baseline MULDICON geometry. The second is a simple extension plate attached to the lower edge of the exhaust nozzle. The third is a group of positions for a NACA 0015 flap with its leading edge fixed at a position inside the cavity formed by the nozzle plate and lower fuselage surface, with the flap angle at -10, 0, and 10 degrees. The fourth is also a group of positions with the flap leading edge shifted away from the nozzle flow and flap angle at three positions. The length of the extension plate and the chord of the flap are both 25.4 mm.

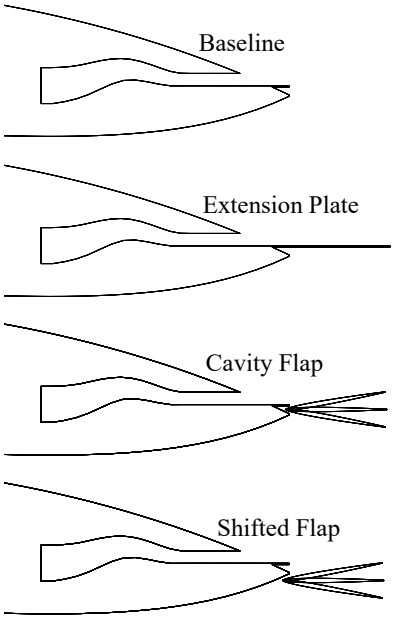


**Figure 6-8: Flap Configurations for MULDICON.**

The sources are defined to model both the fan noise and the jet noise sources in the nozzle flow. For the baseline configuration, the source locations are illustrated in Figure 6-9, for both the baseline geometry with or without flaps (upper plot) and the extension plate (lower plot) geometry. The fan noise source is modeled as a coherent source located at the exit plane of the nozzle. Three sources are used to model the jet noise sources, all of them incoherent. The one at the trailing edge of the lower edge of the nozzle and the extension plate, respectively, represents the interaction source between the jet flow and the trailing edge, which has been shown in previous reports to be the dominant source for the spectral peak. The two other incoherent sources model the distributed sources in the jet plume, one at half flap chord and the other at one flap chord downstream of the trailing edge.

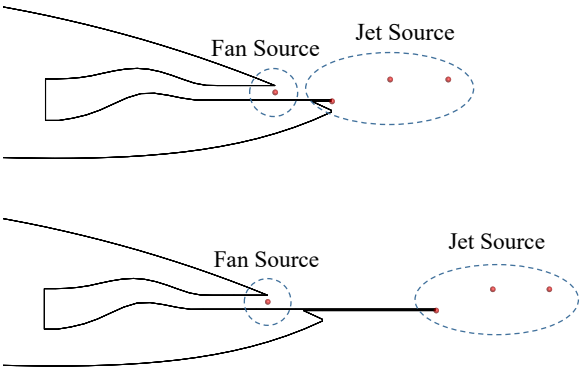


**Figure 6-9: Source Locations for Baseline/Flap (Upper) and Extension Plate (Lower) Geometry.**

Though the cross-section model cannot capture the three-dimensional scattering of the full configuration MULDICON, it includes some features that are absent in the airfoil model discussed in the previous section and that may have significant impact on the scattering characteristics. In the trailing edge region, there are multiple edges. The nozzle has a lower and an upper edge, which are not aligned. Below the lower nozzle edge, there is potentially a cavity, providing another edge for diffraction. The geometry has a thick curved body upstream of the trailing edge region, potentially acting as a shielding body to upstream angles. The sources for the MULDICON vehicle are different from those of the airfoil case. The fan noise source is very close to the scattering surface, from which efficient shielding can be expected, while the jet noise sources are mostly downstream of the geometry with at least partial direct radiation from the sources to the microphones. The jet noise sources are incoherent so that no interference pattern is expected in the scattered noise. There are altogether 96 configurations covering the parameters discussed in the previous paragraphs, which is much fewer than the 3150 cases for the NACA 0012 airfoil computations, because some parametric variations are not included here, such as the gap width and the flap overhang, the selections of which will rely on the results and analyses of the NACA 0012 computations.

The shielding effects on the fan noise component at 20 kHz, modeled by a coherent source at the nozzle exit plane, due to the flaps are shown in Figure 6-10, for the cavity flaps by the left plot and for the shifted flap by the right plot. In both cases, the shielding ΔSPL is plotted as a function of the polar angle, and the baseline and the extension plate are also shown in the plots for comparison, represented by the red and the green curve, respectively. For both groups of flaps, results for all three flap angles are shown in the figure.

The baseline configuration shows good shielding on the fan noise because the lower trailing edge of the nozzle is many wavelengths downstream of the source, so most of the polar angles under consideration are in the shadow region. For angles larger than 90 degrees in the aft quadrant, the shielding provides up to 20 dB noise reduction with the noise mostly from the weak diffraction at the lower trailing edge of the nozzle. In the forward quadrant with angles smaller than 90 degrees, the noise reduction is further enhanced by the blocking of the trailing edge diffraction by the lower edge of the cavity and by the highly curved lower body surface upstream of the cavity. Since the blocking occurs only for angles less than 90 degrees, the enhanced noise reduction has a sudden drop at this angle, as shown in the figure. In the blocked region, the noise shielding can be as much as 40 dB, which is of course only for the fan noise component with the total noise likely much higher because of the presence of other noise components. An uncertainty in this computation and the results for the baseline configuration is the size of the cavity. If the opening of the cavity is smaller than a wavelength, its lower edge cannot be treated as an independent scattering feature. Instead, the sound waves cannot distinguish it from the lower trailing edge of the nozzle. In this case, the shielding will be given by the trailing edge diffraction without any blocking and the fan noise reduction will be on the order of 20 dB, still an impressive amount of noise reduction, especially considering that this is for the baseline configuration without any added shielding device.

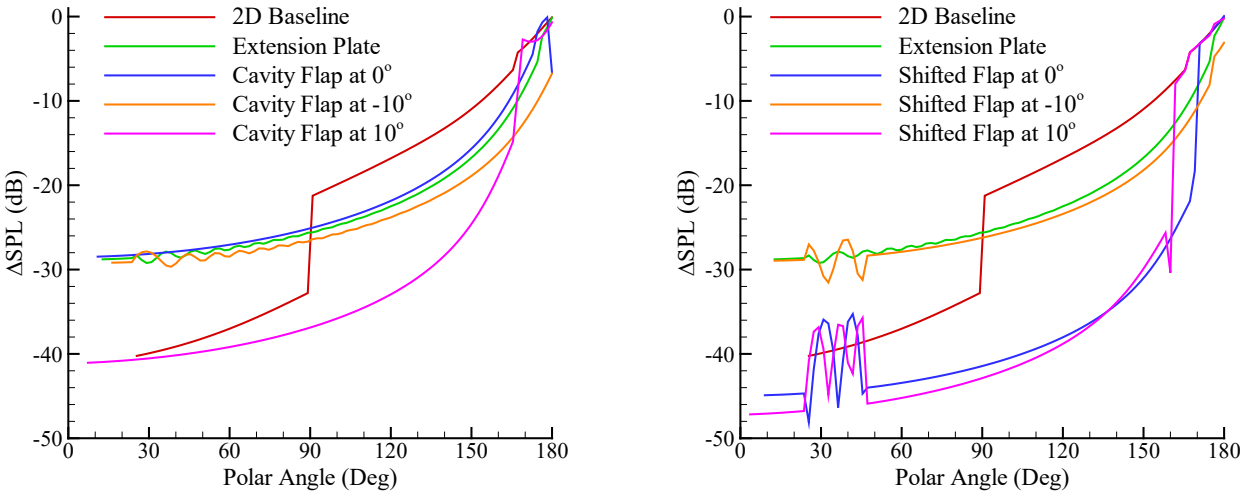


**Figure 6-10: Shielding Effects on Fan Noise at 20 kHz by Cavity Flap (Left) and Shifted Flap (Right).**

For the configuration with an extension plate, represented by the green curves in the figure, it is interesting that in comparison with the baseline, it can increase the noise reduction in the aft quadrant and decrease the noise reduction in the forward quadrant. As analyzed in the previous section for the NACA 0012 airfoil, the attached plate expands the shadow region and enhances the shielding effect, which is the reason for the increased noise reduction in the aft quadrant shown in the figure. This mechanism also applies to the forward quadrant but the extension plate, with its trailing edge further downstream, also eliminates the blocking by the lower edge of cavity. The combined effects of these two features are some noise increases in the forward quadrant. These noise increases, however, are no reasons for concern, because the noise levels in this region are already very low.

By comparing the results of all the flap configurations plotted in the figure, the shifted flap with zero or negative deployment angle appears to be the best in maximizing the shielding effect for aft fan noise, which is consistent with the conclusion from the parametric studies for the NACA 0012 airfoil discussed in the previous section. The scattering mechanisms resulting in the best shielding effects are similar for the two cases. For the MULDICON case, the main benefit comes from the blocking of the diffractions from the lower trailing edge of the nozzle and the lower edge of the cavity. Because of the presence of a gap between the main body and the flap, there is some leakage effect directed at small angles in the upstream direction, leading to some noise increase in the region between about 20 to 50 degrees, as shown by the right plot in the figure. Again, the noise increase is not a concern in practical applications because of the very low noise levels. Furthermore, real engine noise consists of other components, such as jet noise, which may not experience as much shielding and thus may overwhelm the fan noise so that the significant shielding effects on fan noise may not be noticeable in the total noise metric. The analysis presented here is only meant to understand the scattering physics.

The jet noise for the MULDICON vehicle has a component resulting from the interactions between the jet flow inside the nozzle and the lower trailing edge of the nozzle. The source location of this noise component is close to the trailing edge. Thus, an incoherent source at the trailing edge is used to model the edge noise, with the results given in Figure 6-11 for 20 kHz with the left plot for the cavity flaps and the right one for the shifted flaps. The results for the baseline and the extension plate are also given in the figure. For the baseline, the noise from the edge source is shielded by the MULDICON body in the forward angles from the trailing edge, which leads to the gradual increase in noise reduction, up to about 10 dB, as the polar angle decreases, shown in the figure by the red curves. In aft angles, the microphones have direct line of sight to the source so that the shielding is zero. The shielding effects for the baseline geometry start at about 120 degrees in polar

angle because the coordinate system is based on the leading edge of the vehicle. The extension plate does not help the shielding of the edge source at all. The plate effectively shifts the source location further downstream away from the scattering body so that the body cannot shield noise anymore, which gives zero shielding for all angles, as shown by the green curves in the figure.

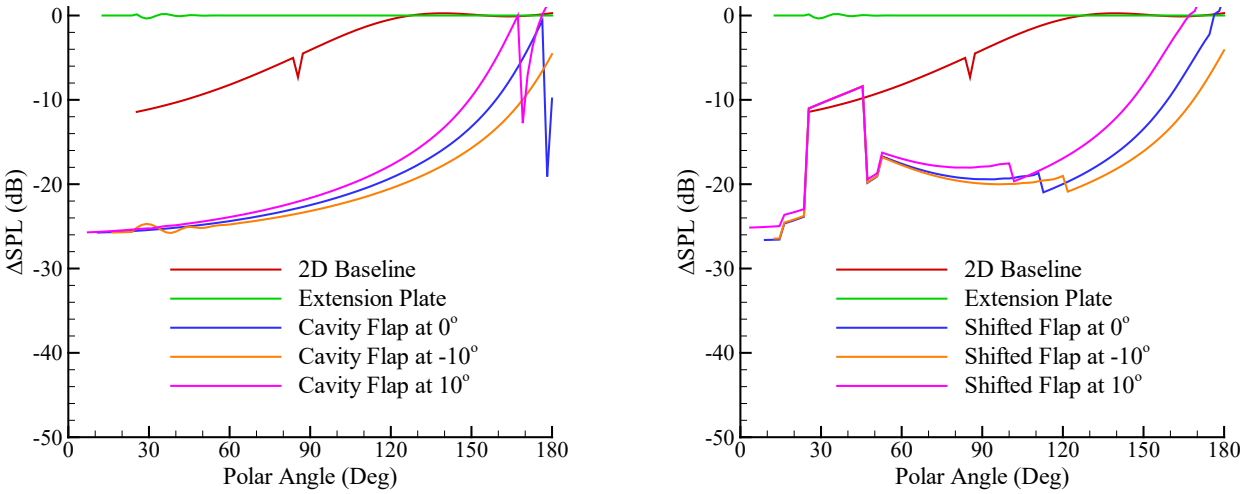


**Figure 6-11: Shielding Effects on Jet/Edge Interaction Noise at 20 kHz by Cavity Flap (Left) and Shifted Flap (Right).**

Since the source of the jet/edge interactions is at the lower trailing edge of the nozzle, all flap configurations help to significantly enhance the shielding effects by blocking the direct radiation from the source to the microphones, and by blocking the diffraction from the lower edge of the cavity for the shifted flaps that are located below the cavity. The flaps are similarly efficient in shielding except for the shifted flaps in a small angular range in the forward direction, from about 20 to 50 degrees, where the leakage from the flap gap leads to some noise increase. The angular range in the far field is determined by the size of the gap between the flap and the main body. The leakage is from the diffraction at the lower trailing edge of the nozzle, which is the same diffraction of the baseline geometry. Thus, in the leakage angular range, the baseline noise levels are the upper limits for the geometry with flaps, as clearly shown in the right plot of the figure where the noise levels for the shifted flaps are about the same as the baseline represented by the red curve. There are some variations in the shielding level as a function of the flap angle, with negative angles better than positive angles, especially in the aft directions in the partially insonified region. This is because negative angles increase the shadow region and positive angles reduce the shadow region. The negative flap angles, however, are not recommended for practical applications because the flap trailing edge is likely to intrude into the jet plume, inducing additional noise sources that can easily generate more noise to completely cancel the shielding effects.

The jet noise also has a component from sources in the jet plume, which is modeled by incoherent sources located some distance downstream of the nozzle trailing edge. The shielding effects for these sources are shown in Figure 6-12 for all the flap configurations with the source at the half flap chord location. In this case, the baseline and the extension plate have limited shielding effects, only a few dB in the forward angles. Similar to the case of edge sources, the flaps are similarly efficient in shielding except for the shifted flaps in a small angular range in the forward direction where the leakage from the flap gap leads to some noise increase, and the leaked noise levels are limited by the baseline levels. Also similarly, negative flap angles seem to give more shielding, but this should not be considered a practical configuration because of the potential of jet/edge interaction, as discussed in previous paragraphs.

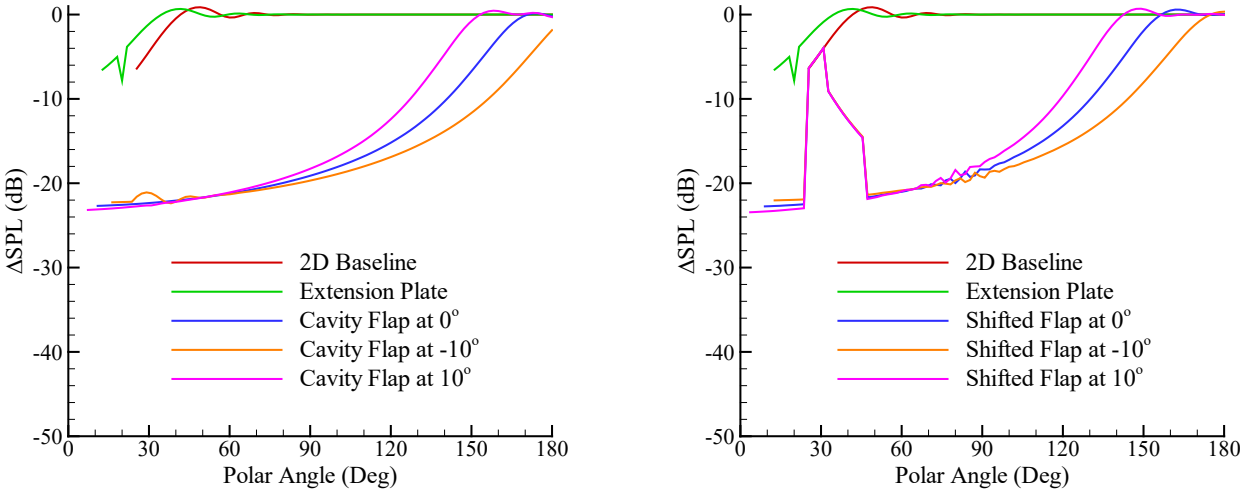


**Figure 6-12: Shielding Effects on Jet Noise from Near Edge Source at 20 kHz by Cavity Flap (Left) and Shifted Flap (Right).**

For jet noise generated by sources in the jet plume far downstream of the nozzle, an incoherent source is used, and its location is chosen to be one flap chord length downstream of the lower trailing edge of the nozzle. The shielding effects are shown in Figure 6-13. In this case, there is no shielding for both the baseline and the extension plate configuration, shown by the red and the green curves, because the source is far away from the scattering body. When a flap is added to the baseline, the flap extends the scattering body in the downstream direction and the flap trailing edge is close enough to the source to have some shielding effects, even though the noise reductions are smaller than those for other sources discussed earlier in this section. The shielding characteristics are essentially determined by the flap trailing edge, with noise reduction starting at the boundary of the shadow zone and gradually increasing going into the shadow zone as the polar angle decreases. It is interesting that for this source location, a flap with a negative angle gives less shielding in comparison with other angles, in contrast to other source locations discussed earlier in this section. This is because the source is aligned with the flap trailing edge at the zero degree position in the flow direction, and a negative angle reduces the shadow region, and thus reduces the shielding effects.

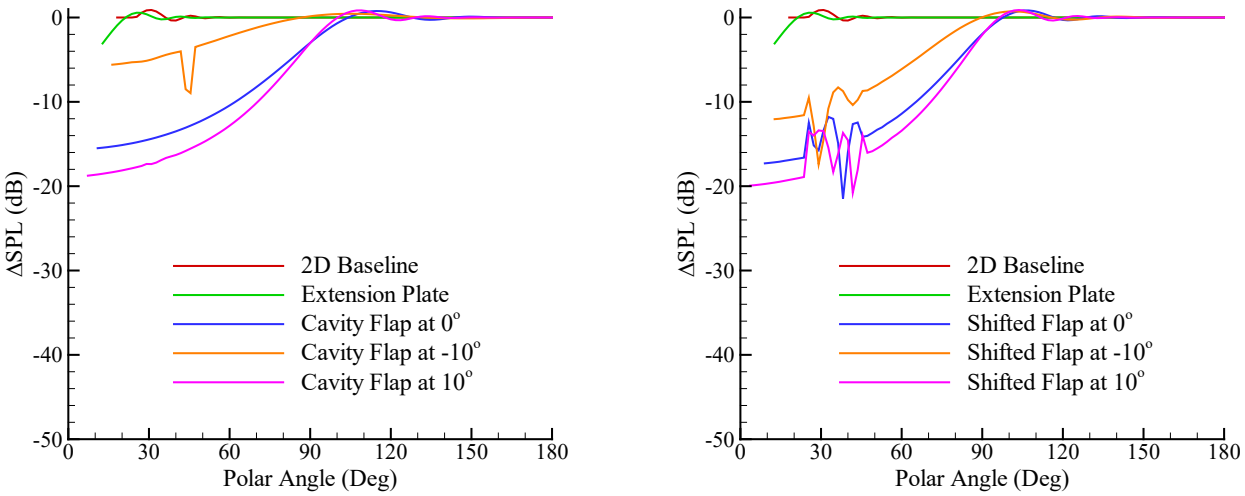


**Figure 6-13: Shielding Effects on Jet Noise from Downstream Source at 20 kHz by Cavity Flap (Left) and Shifted Flap (Right).**

From the results and analysis presented in this section, the best shielding flap for the MULDICON vehicle seems to be the shifted flap with zero or positive flap angle and with a small positive overhang. This configuration gives the best shielding benefit in the most frequency and spatial ranges for both the aft fan noise and the jet noise from the nozzle. It also has advantages in practical applications, such as avoiding jet/flap interactions.

It is important to emphasize that the computations are not simulations of the real MULDICON vehicle. The geometry is simplified as a cross-section model and the sources are modeled as simple ideal sources. Three-dimensional scattering is not captured in the results presented here. Full configuration computation is planned but has not been completed. Improvements to the calculations can be achieved by using distributed sources with realistic directivity, which is known to significantly affect scattering. For these reasons, the results presented here should be considered as representing qualitative trends, instead of quantitative effects.

### 6.1.3 Comparison with Experimental Data

From the analysis of the QFF test data, some of which is presented and discussed in Section 5.2.2, it is shown that the coherent source and the multiple propagation paths lead to scattering patterns that are dominated by rapid variations in sound pressure levels in both frequency and spatial domain, in the form of sharp dips and peaks. This makes it difficult to analyze the scattering effects and to compare results both between configurations and between predictions and data, based on single frequency and single measurement point. Instead, it is more appropriate to carefully define quantities, with integration and/or weighting and/or normalization, as metrics to assess the shielding efficiency and to compare data with predictions. This is planned but is not ready for this report. In this section, some comparisons are presented, still based on the single frequency and single measurement point results.

For the case of an extension plate attached to the baseline NACA 0012 airfoil, examples of the comparisons between data and predictions are given in Figure 6-14 at 10 kHz by the left plot and 20 kHz by the right plot, with the curves representing predictions and the symbols for the test data. The results are for M = 0 and the source position at 70% airfoil chord length. There are discrepancies between data and predictions, some of which are also seen in other cases, as will be presented later in this section. The reasons for these discrepancies, either due to mismatch of configurations and conditions between tests and computations, or due to inadequate modeling in the computations of some aspects of the scattering process, or both, will be discussed later in this section.

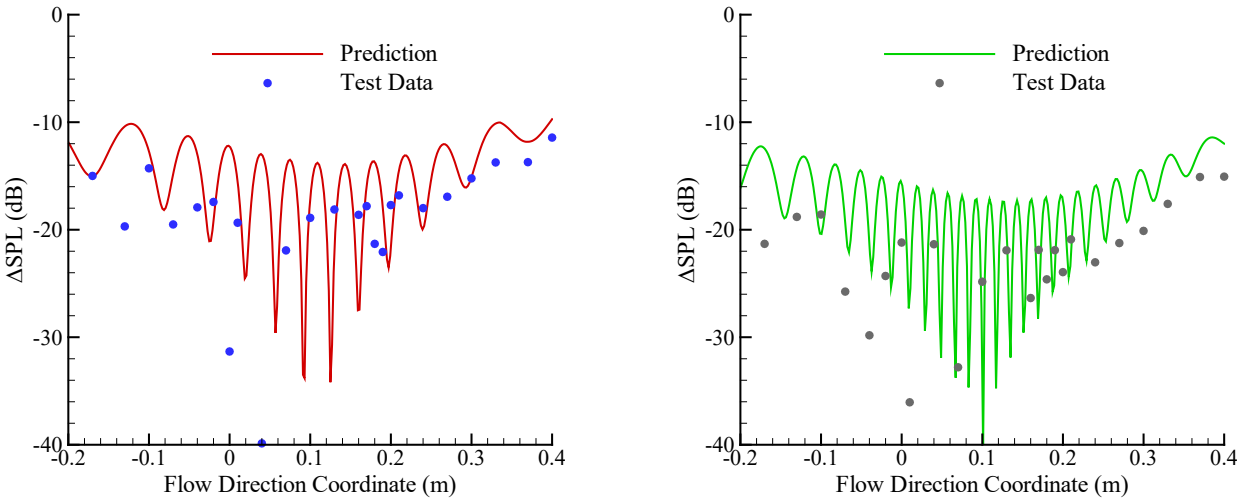


**Figure 6-14: Comparisons between Data and Predictions for Extension Plate at 10 kHz (left) and 20 kHz (Right) for M = 0 and the 70% Source Position.**

If the comparisons are made between the curves and the trends formed by the symbols, the discrepancies seem to be very large. This kind of comparisons, however, can be misleading because the measured data are sparsely distributed and simple linear interpolation between data points for coherent sources are known to be inaccurate if the data points are far apart from each other. This is indeed the case here. The distances between the data points are usually larger than the period of variations, as is clear from the figure, and thus, the sharp dips and peaks are likely missed by the measurements. In fact, many data points are right on or close to the prediction curves, indicating accurate prediction at these locations. There are some low-level data points that are far below the prediction. If the flow direction coordinates of these points are aligned with or close to any sharp dips on the curves, the discrepancies are not prediction errors of concern, but due to the sensitive natures of the dips to the precise measurement location and the precise value of the coherence, both of which are not exactly matched between tests and computations. These considerations should be applied to all the comparisons in this section.

For flaps shifted from the main airfoil chord line into the microphone side by the amount of 12.7 mm, some comparisons are given in Figure 6-15 and Figure 6-16, for flap angles of respectively zero and -10 degrees. The figure formats are the same as in Figure 6-14 with the left plots for 10 kHz and the right plots for 20 kHz and for the configuration of M = 0 and the source position at 70% airfoil chord length. For shifted flaps, an important feature predicted by the computations is the noise reduction in the downstream direction in comparison with both the baseline and the extension plate case, approximately in the range between x = 0.2 m to x = 0.35 m, namely, downstream of the trailing edge of the main airfoil. The lower noise levels are indeed measured in the tests, as shown in the two figures, but there are significant discrepancies in the details with a smaller range of the low noise region in the data than in the predictions. This again can be attributed to the reasons discussed at the end of this section. The comparisons for the region upstream of the main airfoil trailing edge are good, with many data points on or close to the prediction curves. The negative flap angle leads to changes in the scattered noise, both in the test data and in the predictions, as is clear by comparing the two figures. Since the focus for these figures is the comparisons between data and predictions, the meaning and the scattering physics of these changes will not be analyzed here. In terms of comparisons, the agreements and discrepancies are similar between the cases of zero and negative flap angle.

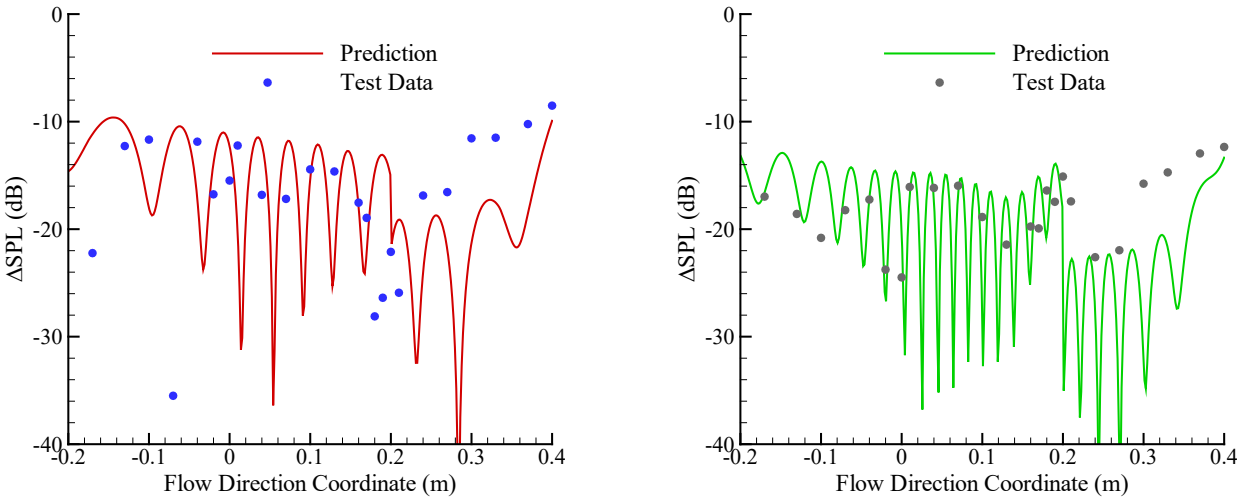


**Figure 6-15: Comparisons between Data and Predictions for Shifted Flap at Zero Angle and Zero Overhang for 10 kHz (Left) and 20 kHz (Right) for M = 0 and the 70% Source Position.**

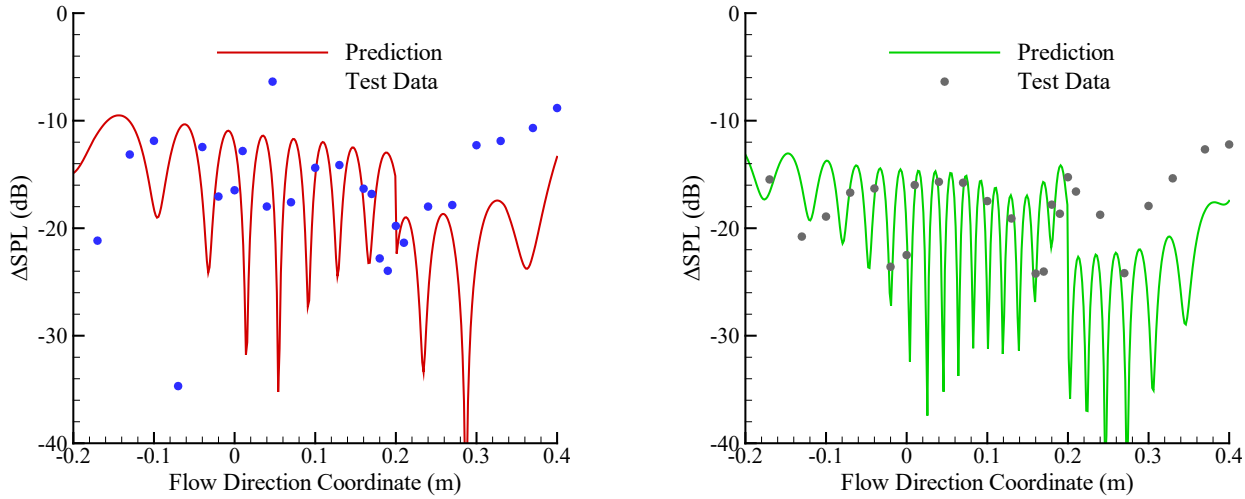


**Figure 6-16: Comparisons between Data and Predictions for Shifted Flap at -10 Degrees Angle and Zero Overhang for 10 kHz (Left) and 20 kHz (Right) for M = 0 and the 70% Source Position.**

For shifted flaps with positive overhang of 6.35 mm, some comparisons are given in Figure 6-17 and Figure 6-18 for flap angles of respectively zero and -10 degrees. The figure formats are the same as previous comparison figures with the left plots for 10 kHz and the right plots for 20 kHz and for the configuration of M = 0 and the source position at 70% airfoil chord length. The flap overhang is designed to modify the scattering by reducing the leakage from the gap between the flap and the main airfoil. The assessment of this concept is not the focus of these two figures and thus will not be discussed here. For the comparisons between data and predictions, the overall trends of agreements and discrepancies are similar to other configurations.

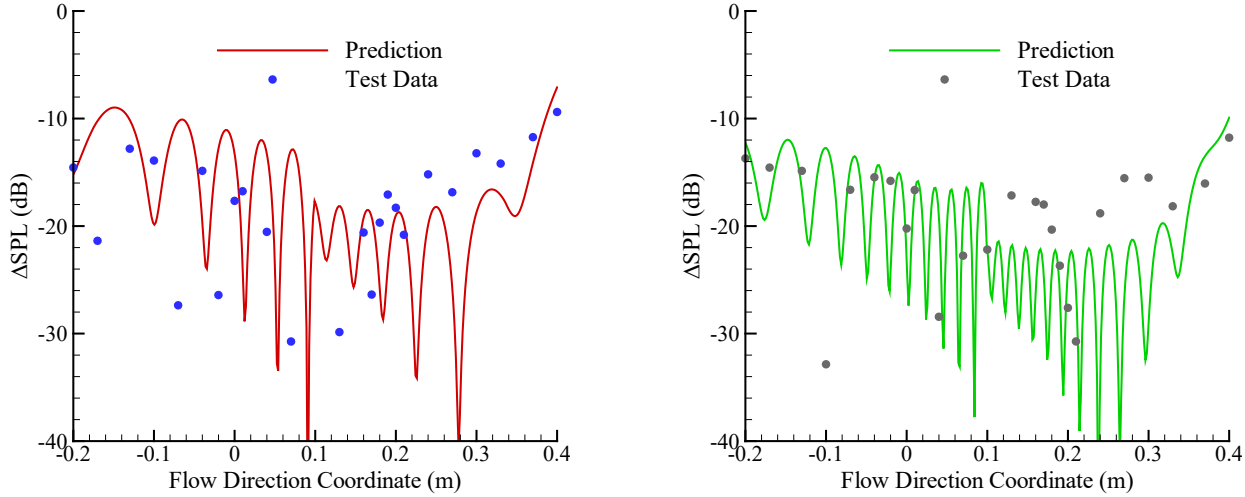


**Figure 6-17: Comparisons between Data and Predictions for Shifted Flap at Zero Angle and 6.35 mm Overhang for 10 kHz (Left) and 20 kHz (Right) for M = 0 and the 70% Source Position.**

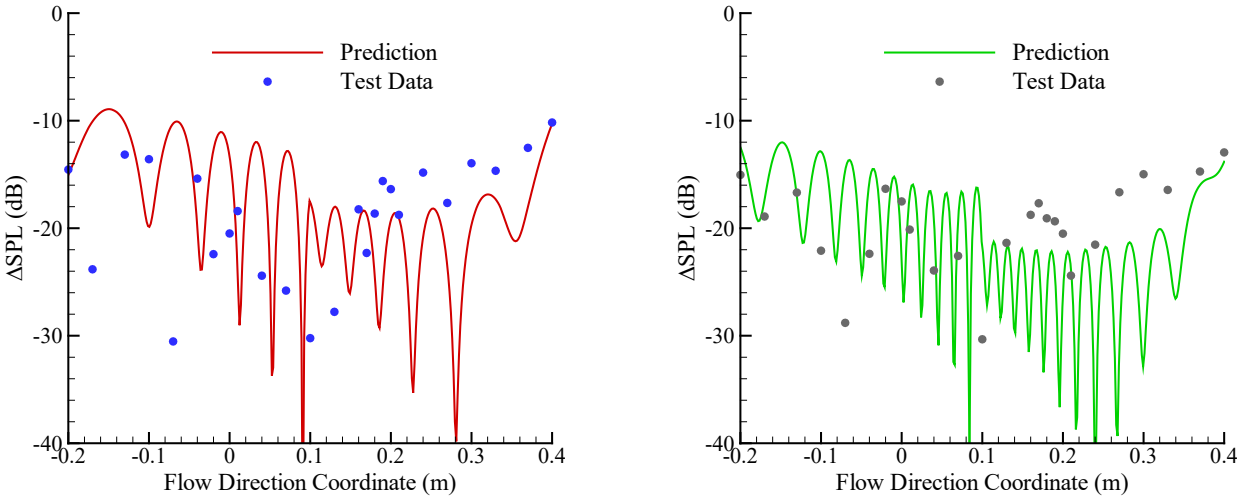


**Figure 6-18: Comparisons between Data and Predictions for Shifted Flap at -10 Degrees Angle and 6.35 mm Overhang for 10 kHz (Left) and 20 kHz (Right) for M = 0 and the 70% Source Position.**

The results presented in this section are only a subset of the test database, which includes many variations in source location, mean flow Mach number, and frequency. They are representative of other cases in the overall trends of the agreements and discrepancies between data and predictions. The agreements show the correct modeling of major aspects in the computations and the discrepancies have various reasons, some of which are due to the metric and presentation of the results, some of which result from inevitable mismatch of test and computation, and some of which point to potential improvements of the prediction methodology.

One feature related to data presentation, discussed earlier in the section, is the measurement locations that are sparse and not sufficient to capture the interference patterns resulting from the highly coherent source and multiple propagation paths in the scattering. In most cases, the data measurement locations do not coincide with the peaks and dips of the interference patterns. This can lead to misleading and incorrect data trends and patterns if interpolation is used to connect the data points, either visually or computationally. Without the true trends from the data, the best approach for comparison is to examine the agreements at individual points. In all the figures presented in this section, if the data points are simply connected, the resulting curves would look very different from the prediction curves, even though many data points are right on or close to the prediction curve.

Another feature that is also related to data presentation is the metric used in the comparisons. The quantity in the figures in this section is the conventional straightforward sound pressure level, for single frequencies in the computations and for frequency bands of 61 Hz in the data. For rapidly varying scattering patterns, there may be noticeable difference between the two frequency treatments. Even if the computations are done also for frequency bands, which is not a difficult effort, the comparisons with data may still be subject to irregular discrepancies because there are inevitably mismatches in some parameters between tests and computations that may shift the interference patterns to amplify the discrepancies. Mismatches in test conditions can occur in many parameters, including source location, source dimension, measurement location, scattering geometry, and flow condition. For computations, these parameters are precisely defined to be mathematically exact. In tests, great care is always taken to ensure accurate values of these parameters. This is usually sufficient but for highly oscillating scattering patterns, may cause noticeable errors. To avoid this, it is desirable to define quantities by integration and/or normalization, or other approaches, to minimize the sensitivity of the results.

It should be noted that there are features in the tests that are not modeled or modeled differently in the computations. One example is the source dimensions. The laser spark source used in the test has been shown to be a good approximation of a theoretical monopole source, which leads to the model of point sources in the computations. However, the laser spark source is not a point source and has dimensions in the range of 2 to 5 mm. It is not clear at this time how the laser spark source of finite dimensions can be modeled in the computation methodology used in this report, and if there is any noticeable impact to the scattering process. Another example is the scattering geometry. In the computations, the scattering bodies are modeled as smooth and rigid, but in the tests, the airfoil surfaces are treated with tripping devices to avoid flow separation. The roughness due to the tripping devices is tiny so that no significant effects are expected for mechanisms such as reflection because the acoustic wavelength is much larger than the dimensions of the roughness. It is, however, an open question whether and how the roughness can affect the smooth geometry diffraction from the airfoil leading edge, where the surface creeping waves propagating along the surface are the physical mechanism of the diffraction.

Some of the discrepancies in the comparison results are due to inadequate modeling in some aspects of the prediction methodology. One example is the low frequency correction. The methodology for the predictions is based on geometric acoustics, as discussed in section 3.1.1, which is theoretically applicable to high frequencies, or small wavelengths compared with typical dimensions in the scattering process. For the shielding flap geometry, the flap chord is 25.4 mm and the gap between the flap and the airfoil is 12.7 mm, which are both smaller than the wavelength of 34.5 mm at the frequency of 10 kHz. This in theory makes the geometric acoustics not applicable. To relax this restriction, a heuristic correction is implemented in the computations that has not been validated. One of the important objectives of the QFF tests is to provide data for validating the correction model and for identifying potential improvements. The comparisons, those presented in this section and those for other configurations, and the discrepancies revealed by the comparisons are valuable in achieving this objective.

## 6.2 AIRBUS DEFENCE AND SPACE NUMERICAL ANALYSIS AND VALIDATION

Patrick Zimmermann

The numerical analysis by Airbus Defence and Space relate to intake and jet noise calculations of the MULDICON configuration.

1) **Intake noise**

   The first study of the intake noise propagation with the monopole source is focused on varying the intake mass flow rate whereby no ambient flow is considered. To investigate the influence of the intake suction on the wave propagation and radiation mass flow rates of 0, 0.3 and 0.4 kg/s are analyzed. The directivities of the sound pressure levels at 1 kHz, shown in Figure 6-19, indicate a homogeneous characteristic in the forward direction 0-90 deg with slightly increasing SPL for higher mass flow rates. The SPL differences lie below 1 dB. A similar tendency can be seen for 2.5 kHz with a decrease in SPL between 45 – 90 deg. At higher frequencies a dominating behavior in SPL can be observed for the reference case without intake suction in the forward direction exceeding the levels with intake suction. The maximum levels lie between 25-45 deg at 5 kHz. At 10 kHz no uniform main radiation direction is given with maxima between 0-10 deg. Thereby, no consistent tendency is apparent for the mass flow rates of 0.3 and 0.4 kg/s. While the SPL values at 0.4 kg/s dominate between 0-40 deg the mass flow rate of 0.3 kg/s shows higher values in the rearward direction.

   In contrast to Figure 6-19 the trend of the 1/3-octave bands under 2 kHz, shown in Figure 6-20, indicates increasing SPL for decreasing mass flow rates. The different tendency in the directivity can be explained by oscillations in the narrowband spectrum. The 1/3-octave bands reach a minimum in noise levels at

2 kHz. Above that frequency band the results with intake suction show no clear trend regarding the SPL differences. Apart from the frequency band of 2.5 kHz the case without intake suction dominates in SPL. The maximum noise levels lie at 5 kHz for all cases.

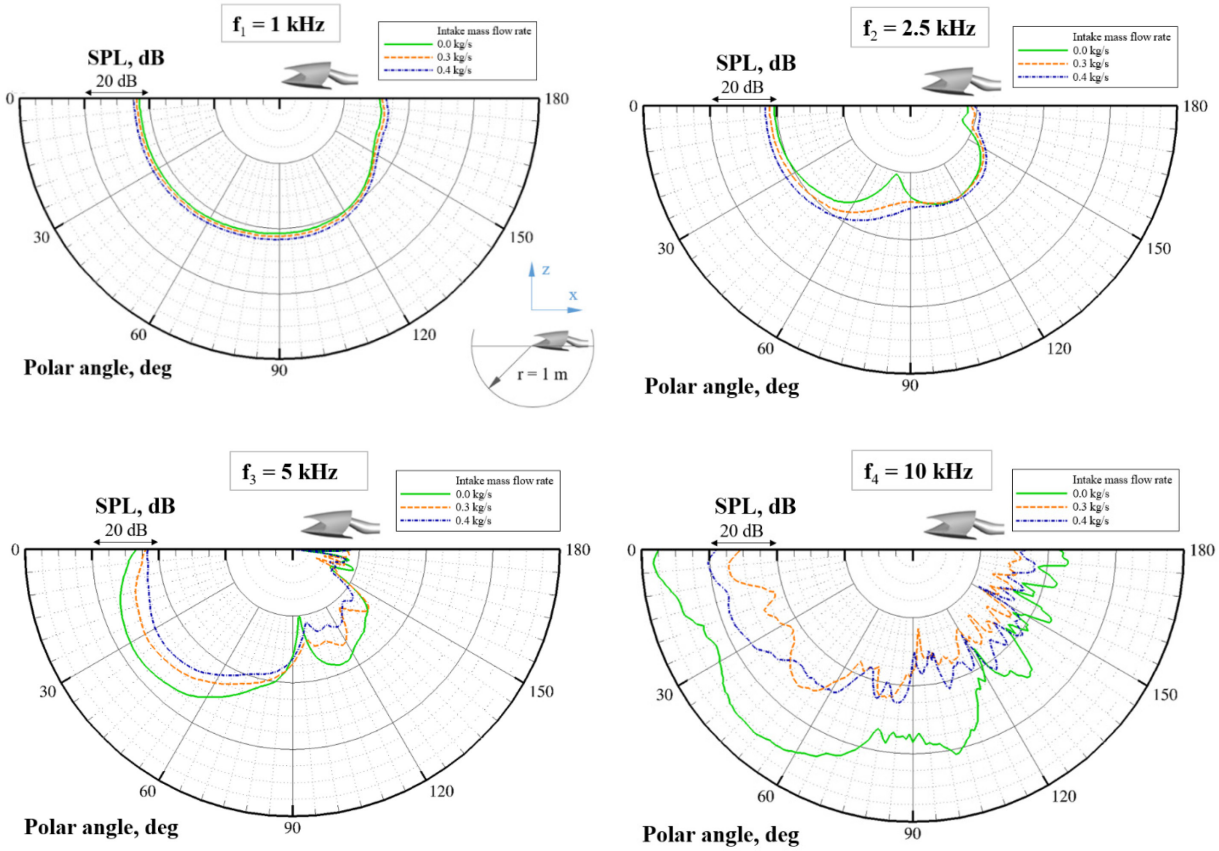


**Figure 6-19: Directivity of the Intake Noise Radiation with a Dependency on the Intake Mass Flow Rate Without Ambient Flow in 1 m Distance.**

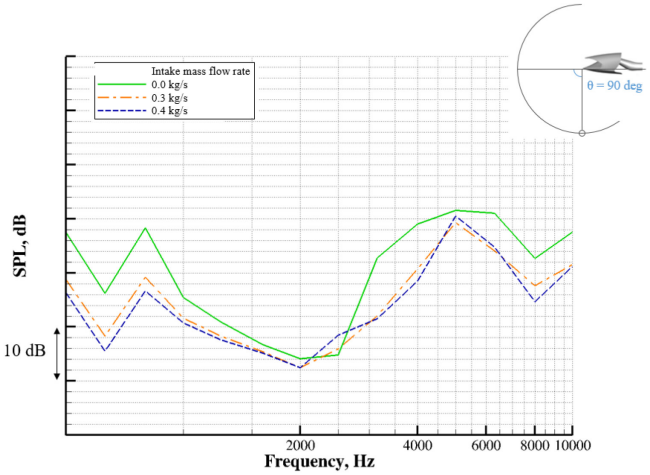


**Figure 6-20: SPL Spectra in 1/3-Octave Bands of the Intake Noise Radiation with a Dependency on the Intake Mass Flow Rate Without Ambient Flow at a 90 deg Microphone in 1 m Distance.**

As a further dependency, the acoustic installation effects are investigated for ambient flow Mach numbers of 0, 0.087 and 0.117 at a constant intake mass flow rate of 0.4 kg/s. The directivities for Ma 0.087 and Ma 0.117 show no significant differences for lower frequencies, see Figure 6-21. At 1, 2.5 and 5 kHz the SPL values of both cases deviate by less than 1 dB. All three cases show uniform directivities in the forward direction at 1 kHz whereby the reference without ambient flow differs by less than 2 dB. For higher frequencies the characteristics of the investigated cases show similarities with larger differences for certain angles.

The 1/3-octave band spectrum at the 90 deg microphone in Figure 2-9 indicates coinciding noise levels for Ma 0.087 and Ma 0.117 in all given frequency bands. The case without mean flow reaches a maximum in the frequency band of 5 kHz with the highest difference to the other cases, see Figure 6-22.

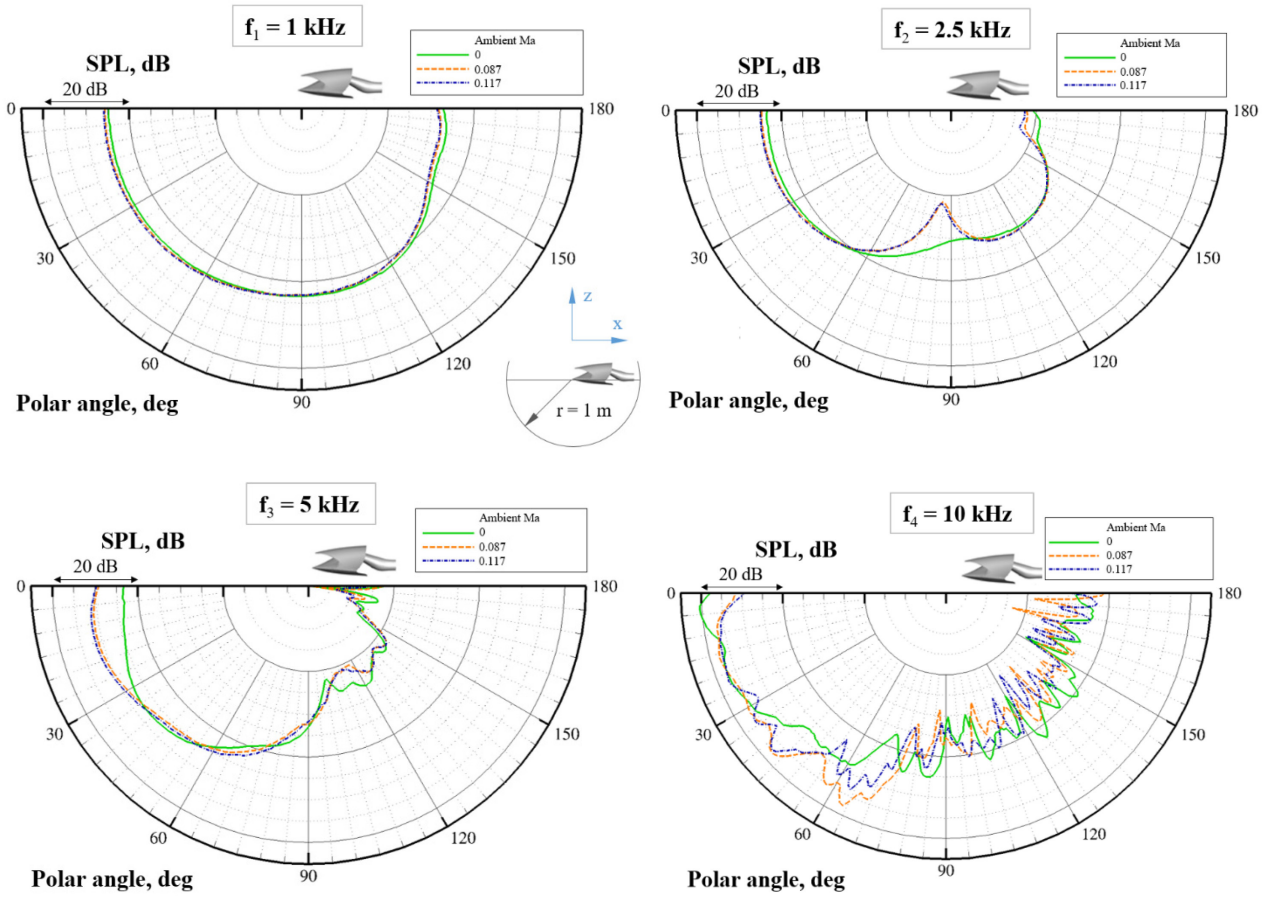


**Figure 6-21: Directivity of the Intake Noise Radiation with a Dependency on the Ambient Velocity for an Intake Mass Flow Rate of 0.4 kg/s in 1 m Distance.**

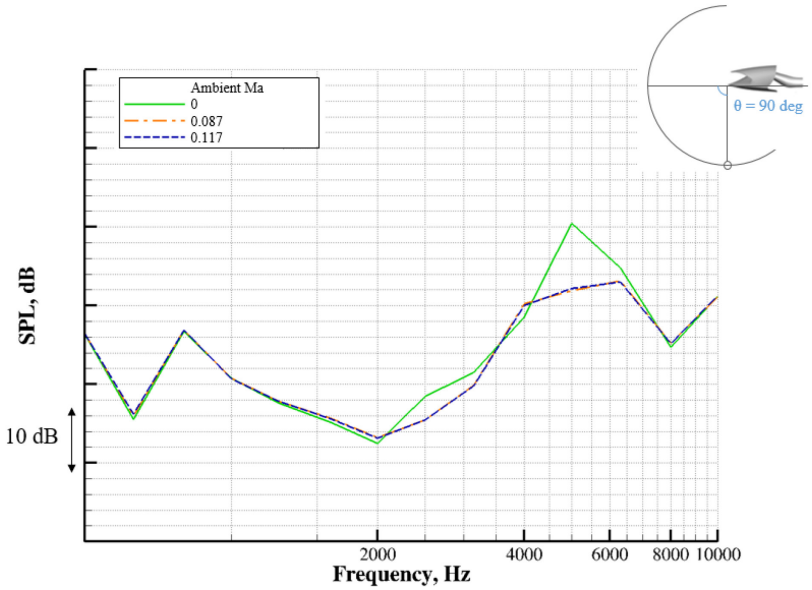


**Figure 6-22: SPL Spectra in 1/3-Octave Bands of the Intake Noise Radiation with a Dependency on the Ambient Velocity for an Intake Mass Flow Rate of 0.4 kg/s at a 90 deg Microphone in 1 m Distance.**

2) **Jet noise**

The reference case for the jet noise simulations is defined at a jet mass flow rate of 1.3 m/s and a wind tunnel velocity of 60 m/s. The sound pressure levels in 1 m distance and 90° to the nozzle trailing edge are shown as narrowband spectrum in Figure 6-23. The comparison with the wind tunnel measurement gives matching trends for higher frequencies from 6 – 15 kHz. At lower frequencies 1 – 6 kHz the results deviate more significantly. The reasons for the deviation are subject to further investigations. In addition to the classical jet mixing sources, co-flow effects in the shear layers and jet-plate interaction effects at the trailing edges have to be analyzed more detailed.

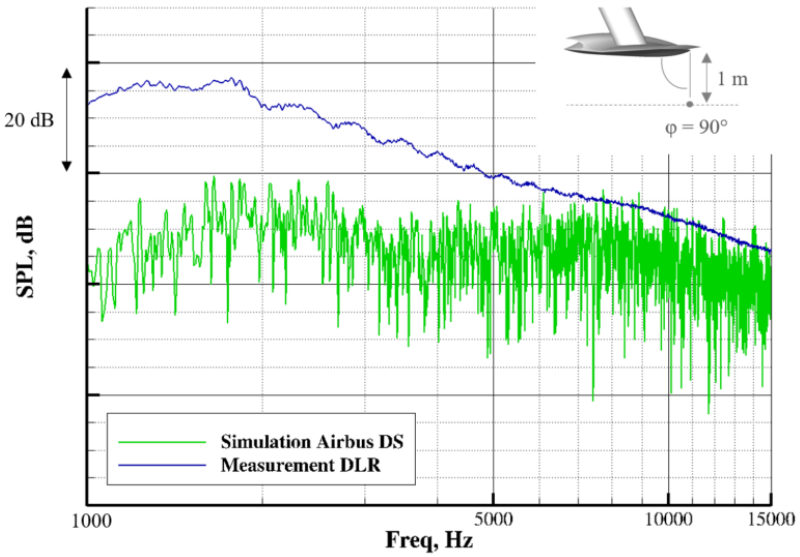


**Figure 6-23: Narrowband Spectrum at 90° Mic in 1 m Distance for Jet Mass Flow Rate 1.3 m/s and WT Velocity 60 m/s.**

The pressure fluctuations in the symmetry plane are shown in Figure 6-24 at a frequency of 12.4 kHz. The acoustic pressure field gives an impression of the directivity. The location of the dominating sources at that frequency can be limited to the area around the trailing edges and slightly downstream. The contribution of trailing edge interaction effects to the source mechanisms is to be clarified in subsequent analysis. The understanding of the source mechanisms leads the way to design effective noise mitigation concepts.

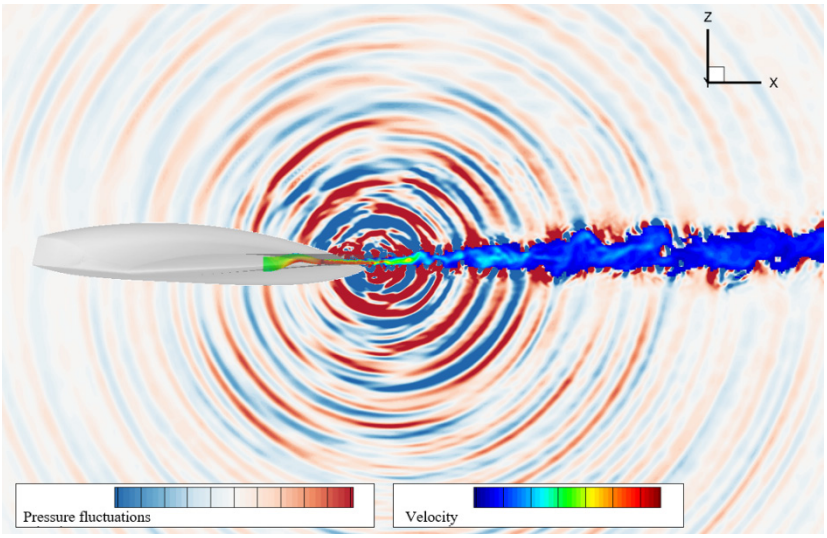


**Figure 6-24: Pressure Fluctuations at 12.4 kHz and Jet Velocity in Symmetry Plane for Jet Mass Flow Rate 1.3 m/s and WT Velocity 60 m/s.**

## 6.3 ONERA NUMERICAL ANALYSIS

Mathieu Lorteau, ONERA

This section presents the acoustic results. First, a validation of the configuration is conducted without the base flow with a BEM simulation. Then, effects of the non-uniform mean flow on the near acoustic field are illustrated by the direct outputs of the CAA computations for the three configurations. Finally, these effects are quantified by direct comparison of the directivities obtained on arc of microphones in the far field by means of a Kirchhoff integral method in the frequency domain [90].

The real part of the Fourier transform of the fluctuating pressure associated to the target frequency (i.e., 5 kHz) is presented in Figure 6-25. These pressure levels are obtained for the configuration without any flow for both the Euler computation (with sAbrinA solver) and the BEM computation.

This comparison shows that both computations provide very similar results despite some slight discrepancies, notably in the destructive interference zone on the left of the figures for which the *sAbrinA* simulation underestimates the pressure levels compared to the BEM simulation. This validates the geometric discretization of the geometry by the IBM computation performed with the Euler solver *sAbrinA*. As already mentioned, the same mesh has been employed for the three *sAbrinA* simulations.

Figure 6-26 and Figure 6-27 present the real part of the Fourier transform of the fluctuating pressure associated to the target frequency obtained on the mid-section plane of the geometry and on a horizontal plane below. These color maps are obtained for the three Euler computations and are shown with the same color scale. As a reminder, the same acoustic source has been employed for the three simulations, i.e., a monopole with a fixed arbitrary amplitude at the frequency 5 kHz.

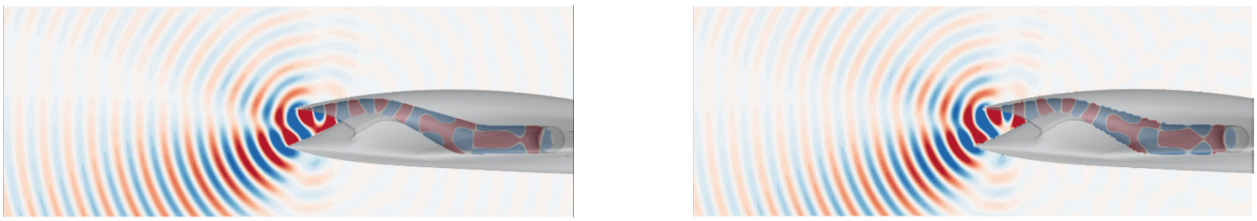

**Figure 6-25: Real Part of the Fluctuating Pressure Field Associated to 5 kHz in the Geometry Mid-Section Plane for (Left) sAbrinA Computation and (Right) BEM Computation; Without any Flow.**

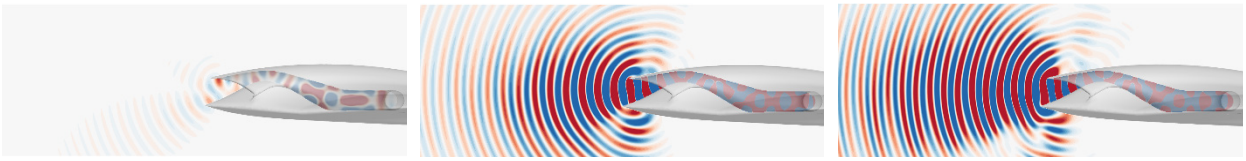

**Figure 6-26: Real Part of the Fluctuating Pressure Field Associated to 5 kHz in the Geometry Mid-Section Plane for (Left) the No Flow Configuration, (Middle) the $M_\infty$ = 0 and Q = 0.4 kg.s$^{-1}$ Configuration and (Right) the $M_\infty$ = 0.116 and Q = 0.4 kg.s$^{-1}$ Configuration.**

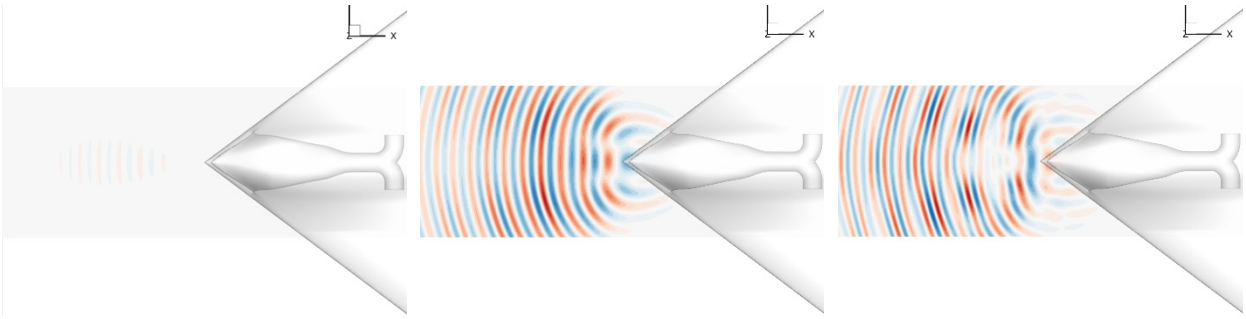

**Figure 6-27: Real Part of the Fluctuating Pressure Field Associated to 5 kHz on a Plane Below the Geometry for (Left) the No Flow Configuration, (Middle) the $M_\infty$ = 0 and Q = 0.4 kg.s$^{-1}$ Configuration and (Right) the $M_\infty$ = 0.116 and Q = 0.4 kg.s$^{-1}$ Configuration.**

These figures demonstrate that the presence of the flow has an impact on the pressure amplitudes radiated by the intake. Indeed, the pressure levels are much higher in presence of a mean flow than without. It is related to the source model used for these computations. Moreover, the comparison between the two simulations with a mean flow shows that the external flow has a limited impact on the pressure levels, the internal flow being responsible for the level increase.

One other modification due to the presence of a mean flow lies in the modification of the main direction of propagation of the acoustic waves. Indeed, the acoustic radiation of the two configurations with a mean flow presents a more homogeneous directivity around the intake than the case without mean flow for which the acoustic waves mainly radiate in the flyover direction.

These latter observations are confirmed by the directivity patterns illustrated in Figure 6-28. In these figures, the angles 0°/360° correspond to the front of the aircraft (on the left hand side of Figure 6-25for instance), the angle 180° corresponds to rear end of the aircraft (on the right hand side of Figure 6-25 for instance) and the angle 90° to positions below the aircraft.

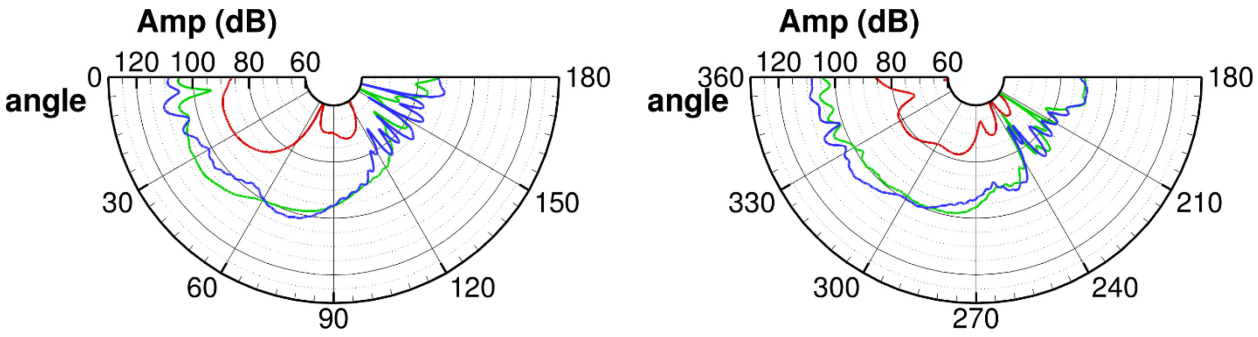


**Figure 6-28: Comparison of the Directivities at 1m in the Mid-Section Plane of the Aircraft (Left) Under the Geometry and (Right) Above. Red: M = 0, Q = 0; green: M = 0, Q = 0.4kg.s$^{-1}$; blue: M = 0.116, Q = 0.4 kg.s$^{-1}$.**

It appears that the acoustic waves of the no flow configuration are radiated mainly in a direction around 30° below and in front of the aircraft with levels being 10 dB higher than those above whereas the two other configurations do not exhibit such a difference between the radiation above and the radiation below the aircraft. When focusing on the downward direction, it appears that the two simulations at $M_\infty = 0$ have the same privileged direction of radiation around 30°. As for the $M_\infty = 0.116$ configuration, the privileged direction of radiation is around 10°, a secondary direction of radiation appears around 70°. This secondary direction of radiation can be related to the presence of the external flow at $M_\infty = 0.116$. The difference for the main direction of radiation might be related to complex interference patterns due to the presence of the local minimum of the flow velocity around the intake lips which is not present for the ($M_\infty = 0$; Q = 0.4 kg.s$^{-1}$) configuration (see Figure 3-6).

These results have been obtained for a single frequency of the source (5 kHz); it would be interesting to complete them with other frequencies. Moreover, the comparison with the numerical data of other partners and experimental data would help to improve the methodology and further the understanding of this aircraft configuration.

## 6.4 FOI ANALYSIS RESULTS

Mattias John Quas, Shia-Hui Peng and Samuel Gottfarb Bart, FOI

The first set of flow computations was carried out on the B1a design, with open intake and no extension plate. In these computations, the free stream had a corresponding Mach number of 0.22 and the mass flow, through the intake channel and outlet nozzle was 1.1 kg/s and 1.7 kg/s, respectively. The dynamic and transport properties for the farfield as well as the outlet nozzle were set corresponding to those of air at room temperature (20°C). The computations were performed with a steady state RANS approach. The results from that initial work suggested that the jet was deflecting downwards after the nozzle exit. This was not expected and was believed to be due to a Coanda-like effect with a low pressure zone close to the wall interacting with the jet flow. In the investigations, two different turbulence models were tested, the one-equation SA model by Spalart and Allmaras [72] and the more complex EARSM model by Wallin and Johansson with the Hellsten k-ω [79]. When the results were compared, the analysis suggested that the downwards displacement of the jet was more pronounced depending on the choice of RANS turbulence model, see Figure 6-29. A sensitivity analysis was furthermore performed to test the jet response to different levels of turbulence to laminar viscosity ratio at the jet outlet nozzle. In the investigation, the turbulence intensity was set to 10 percent and the ratio of turbulence to laminar viscosity was set on the jet outlet nozzle in the range from 100 to 500. The results suggested no significant effect on the jet flow deflection. The position of the downwards deflecting jet was further confirmed with the subsequent time resolved hybrid RANS-LES simulation, performed with equivalent flow conditions as to those of the steady state RANS computations.

Figure 6-30 shows the instantaneous flow field colored by Mach number from this simulation. The result suggested that the jet was exiting the outlet nozzle with a downwards displacement. The results from these initial simulations were discussed within the research group. The discussions led to a decision to create an additional design, B2, with an outlet nozzle extension plate, as shown in Figure 6-31.

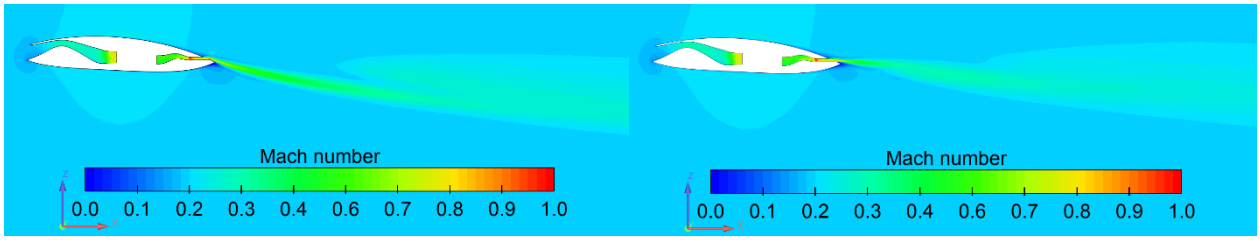


**Figure 6-29: Steady State RANS Simulations Conducted on the B1a MULDICON Design with Two Different Turbulence Models. Mean velocity field colored by Mach number in the symmetry cross section. LEFT: Computation conducted using the SA turbulence model [72]. RIGHT: Computation conducted using the EARSM model [79]. Mass flow through intake and outlet of 1.1 kg/s and 1.7 kg/s respectively.**

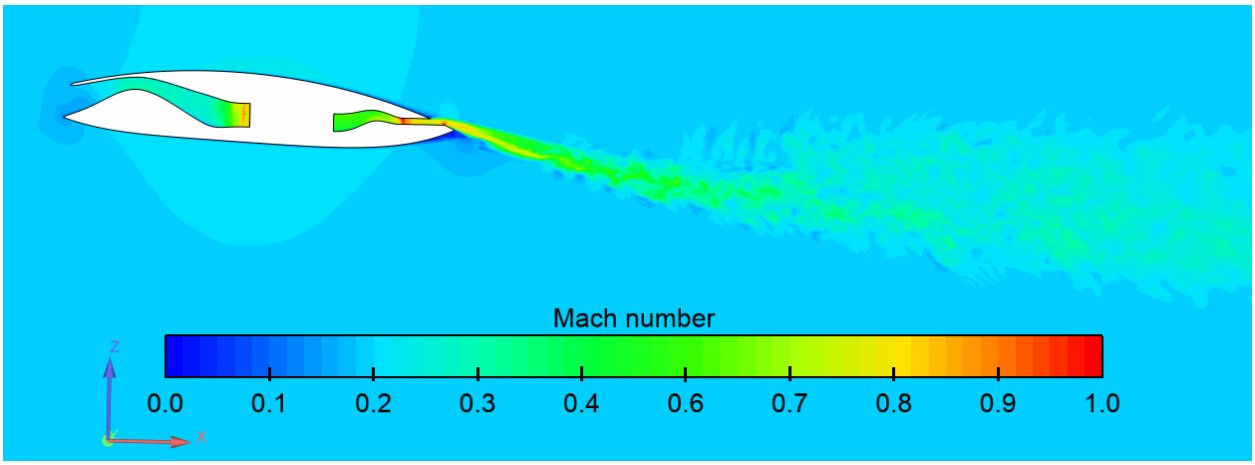


**Figure 6-30: Transient Hybrid RANS-LES Simulation of the B1a MULDICON Design Using the HYB0 Model by Peng [80], [81]. Instantaneous jet flow field colored by Mach number in symmetry cross section. The free stream velocity corresponding to Mach number 0.22. The mass flow through intake and outlet was 1.1 kg/s and 1.7 kg/s respectively.**

The initial computations were conducted on a design with an open intake channel, B1a. For the acoustic wind tunnel experimental campaign, the intake channel was covered. Therefore, a set of steady state RANS computations was conducted to compare the downstream jet flow field changes depending on an open or covered intake channel. Computations were made on all four different designs B1a, B1b, B2a and B2b. The reference conditions for further analyses were chosen to align as much as possible with the experimental setup and study conducted by DLR, see Section 5.1.2. The free stream velocity was set to 60 m/s (Mach number 0.18) and the mass flow of air at the outlet nozzle was set to 1.7 kg/s, with a turbulence intensity of 20 percent and a viscosity ratio of 500. The results from this investigation are not presented in this report but suggested that, by means of using RANS, the effect of introducing the intake cover did not impose a significant change to the jet fluid flow. Thus, an evaluation of the acoustics effect of introducing the extension plate could be based on comparing results from jet noise analyses on designs B1a and B2b.

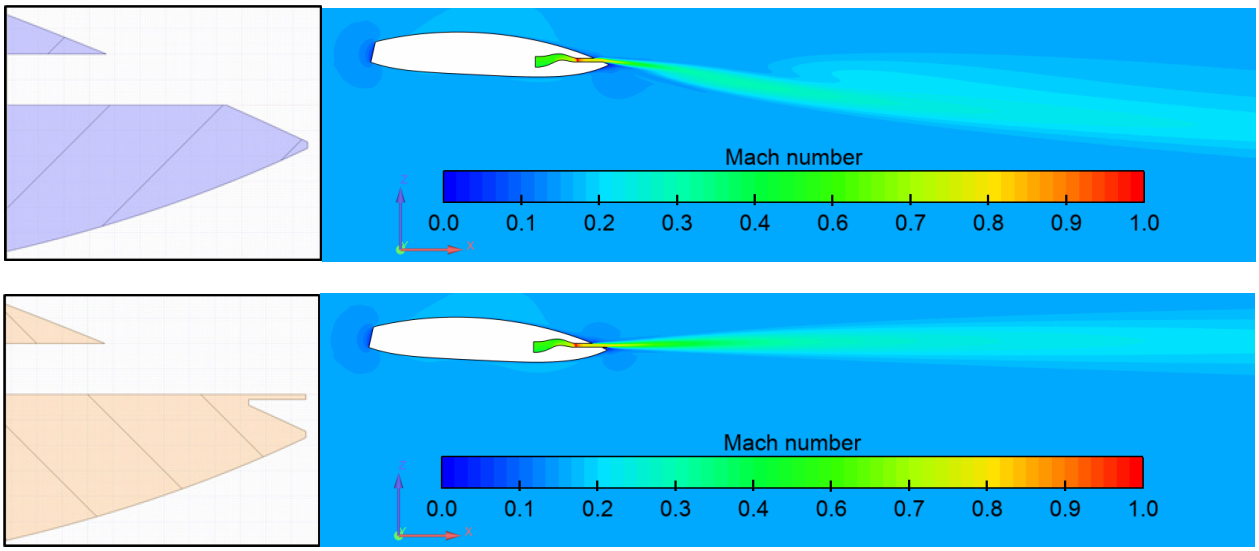


**Figure 6-31: Muldicon Designs B1b and B2b. Outlet nozzle geometry without extension plate (B1) and with extension plate (B2) in the symmetry cross section. Index *b* indicates blocked intake channel. Steady state RANS flow simulation results using SA model [72]. Free stream velocity corresponding to a Mach number of 0.18. Outlet nozzle mass flow of 1.7 kg/s. Velocity magnitude colored by Mach number in the symmetry cross section.**

The aero-acoustics simulations and subsequent analyses were done on two different designs, namely B1a and B2b. The objective was to support the group with general knowledge of the fluid flow and aero-acoustics effects from the jet and furthermore, to compare the effect on the flow induced noise due to the design change of the aft body. The simulations were conducted with initial fields from RANS computations. The simulations were run for 25 000 time steps with an incremental time step size $\Delta t$ of $1 \cdot 10^{-5}$ second. The total simulation time $T$ was 0.25 second. With the freestream flow velocity and the length scale $L_{AC}$ from Section 3.2.3 it is possible to compute the number of flow passes. The simulations were run for more than 11 flow pass times $\#T_{fp}$.

In Figure 6-32 and Figure 6-33, an instantaneous picture of the resolved flow field is shown in terms of iso-surface of vorticity colored by Mach number for the B1a and B2b designs respectively. The complex nozzle geometry gives rise to a highly three-dimensional jet flow with strong vortex roll-up at the upper rounded corners of the nozzle exit. These strong vortices are prominent close to the exit and interact with the co-flow of the ambient air in the shear layer along the full length of the jet. It is suggested from Figure 6-32 and Figure 6-33 that the position of the vortices are rather stationary close to the nozzle and that they are gradually broken up as the momentum is weakened and the interaction with the surrounding flow becomes more pronounced. The wing tip vortices are strong and also stationary in position. These are formed outside the integral surface segments surrounding the jet and should not contribute to the overall noise profile. For the B1a design in Figure 6-32, the jet flow is characterized by the downwards deflection and roll-up of large vortices when the jet leaves the nozzle. Resolved large and small scale turbulent structures corresponding to the local grid resolution is seen in the nozzle adjacent region. The results for the B2b design shown in Figure 6-33 suggest that the jet is substantially straightened by the introduction of the extension plate.

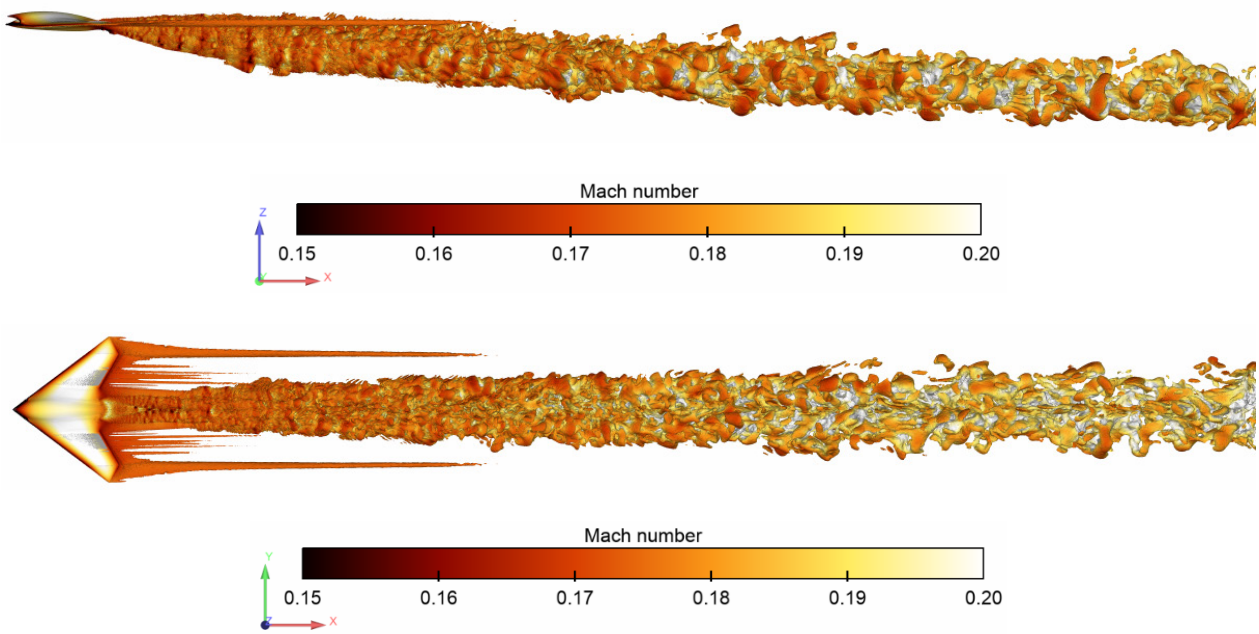


**Figure 6-32: MULDICON B1a design. Jet flow. Results from hybrid RANS-LES simulation using HYB0 model by Peng [80], [81]. Iso-surface of vorticity at a magnitude of 100 colored by the local velocity field in terms of Mach number in the range 0.15 to 0.20. Upper picture: Side view. Lower picture: Top view.**

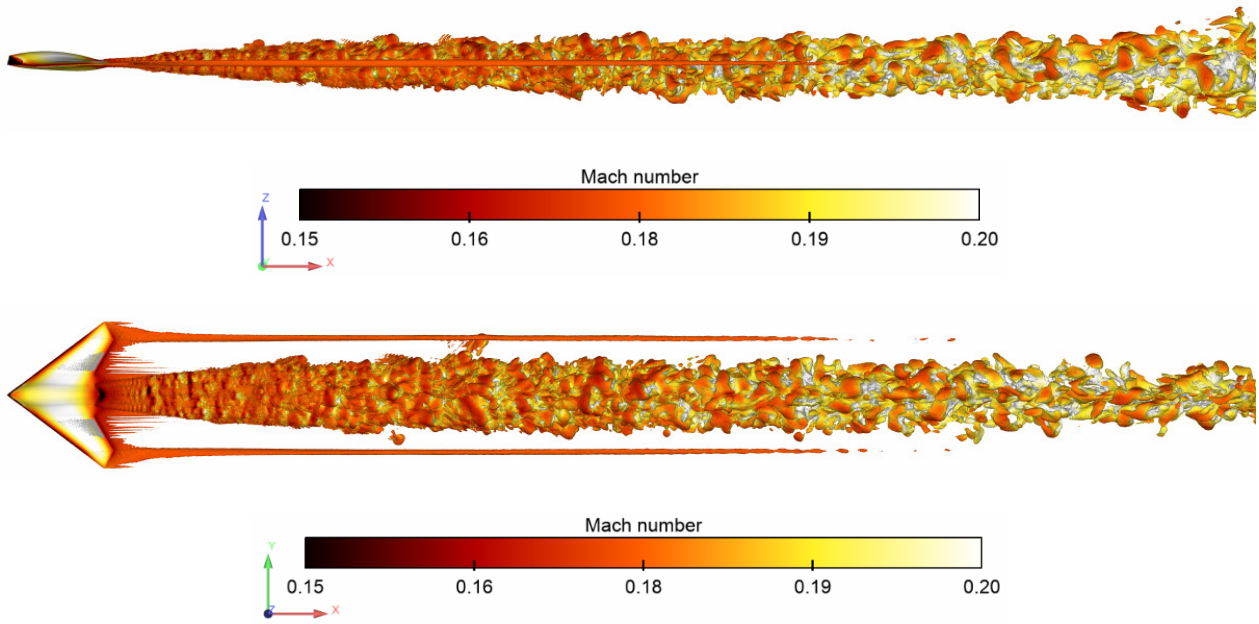


**Figure 6-33: MULDICON B2b Design. Jet flow. Results from hybrid RANS-LES simulation using HYB0 model by Peng [80], [81]. Iso-surface of vorticity at a magnitude of 100 colored by the local velocity field in terms of Mach number in the range 0.15 to 0.20. Upper picture: Side view. Lower picture: Top view.**

The acoustics sampling sets used in the present analysis contain data from the last 10 000 time steps. The frequency resolution $\Delta f$ and the theoretical maximum resolved frequency $f_N$, based on the simulation temporal resolution, suggest a spectral resolution from 10 Hz to 50 kHz. However, based on the typical grid resolution length scales in the jet region adopted to resolve the flow features, the frequency resolution is more moderate ranging up to a maximum of about 5 kHz close to the jet nozzle (region 1 in Figure 3-9) and about 1 kHz in the farther end of the jet plume (region 5 in Figure 3-9). The acoustic sources are computed based on data retrieved from all five integral surface segments 1 through 5, excluding the surfaces surrounding the MULDICON airframe (see Figure 3-4) and the closing caps at the end. The acoustic pressure is computed at the location of the observer one meter below the trailing edge of MULDICON. In Figure 6-34 the results in terms of flow induced noise as sound pressure level are shown for designs B1a and B2b. For both designs, results are based on the inner integral surface segments. The results suggest that the jet flow induced noise is higher in the frequency range 2 000 Hz up to 3 000 Hz for the B1a geometry, when compared to the B2b geometry. In the frequency range 3 000 Hz up to 7 000 Hz, the results suggest comparable noise levels. In the high frequency end of the spectrum, above 7 000 Hz, the analysis again points to the B1a jet flow noise being higher. The general impression from the analysis is that the overall noise profile in the position of the observer is somewhat lowered when the extension plate is installed.

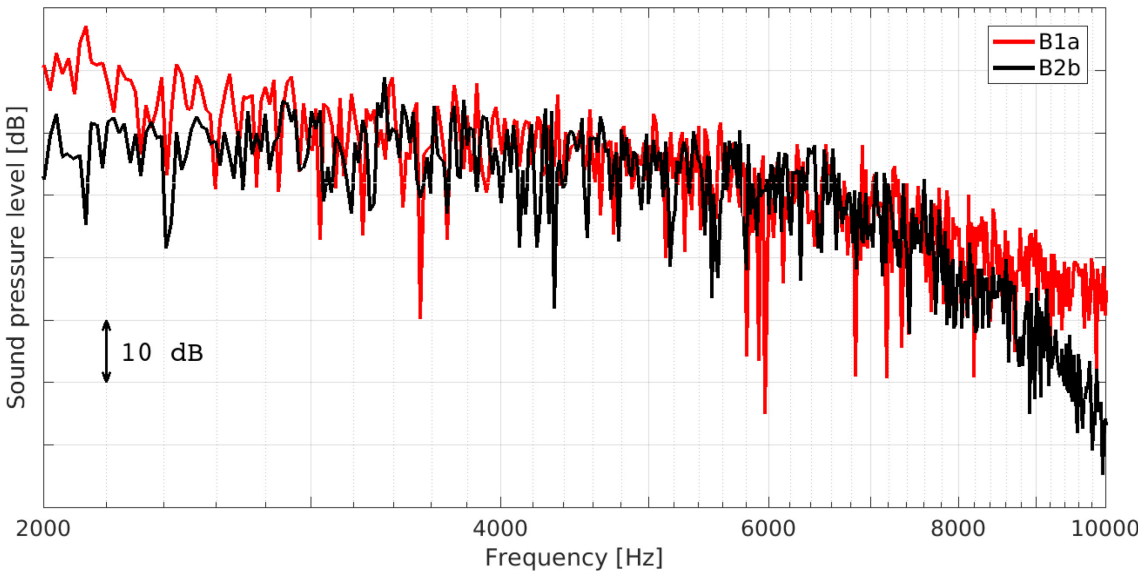


**Figure 6-34: Sound Pressure Level (dB) at the Location of the Observer 1 m Below the MULDICON Trailing Edge as a Function of Frequency in the Range 2000 Hz to 10 000 Hz. Results are based on data sampled on the inner integral surface. Designs B1a in (red line) and B2b (black line).**

It should be pointed out that the results are not yet compared to the experimental data measured by DLR, see Section 5.1.2. The simulation setup is thus expected to be further adjusted and the results are therefore interpreted as preliminary. At present, the results suggest that the overall noise levels are substantially lower than those recorded by the DLR campaign. A comparison with the nozzle flow measurements to be acquired during the CIRA campaign might gain valuable insight with regards to that, as would detailed comparison with the simulation results provided by other group members such as those by Airbus DS, see Section 6.2, Part II. These comparisons could be the subject of future work.

# Chapter 7 – CONCLUSIONS AND OUTLOOK

**Karl-Stéphane Rossignol and Jan Delfs**
DLR
GERMANY

**Russell Thomas**
NASA
UNITED STATES

(with contributions from all)

## 7.1 LESSONS LEARNED

- The first two years of work of the AVT-318 group were heavily influenced by the pandemic, which led to a massive reduction in productivity and communication. The group's work was re-initiated at the beginning of 2021, with a two year extension granted by the AVT Panel, and work meetings were held approximately every two months. This ensured a good communication between partners and also good technical progress.
- The pandemic related reduction in communication led to some issues in the coordination of the experimental work at the DLR-F24 MULDICON with partners performing numerical simulation work.
- The challenges associated with the design, fabrication, and execution of experiments during the course of a pandemic made it the more difficult to ensure an early delivery of validation data to the partners.
- Nonetheless, the overall coherence and alignment of the partners' work and schedule was good.

## 7.2 ASSESSMENT OF RESULTS

The results are assessed in view of the objectives originally set out for the working group (see Chapter 1). In summary, all the essential objectives of AVT-318 were accomplished. The following section discusses the outcome, objective by objective:

- **Demonstrating (on a realistic configuration) the qualification and applicability of tools for the prediction of the effects of propulsion system installation on received sound (using acoustics characteristics of the propulsion system without the engine itself).**
  - High-fidelity CAA simulations methods have been successfully used to investigate both intake and nozzle acoustic radiation of the baseline DLR-F24 MULDICON configuration using different approaches. A significant effort has been invested in setting up the simulation tool chains and developing best practices for grid generation.
  - Airbus Defence and Space intake noise calculations with DLR's high order DG code, matched dependencies of the noise propagation through the intake duct on intake mass flow rate and background flow velocity found in the experiment.
  - Airbus Defence and Space jet noise calculations provide basic understanding of noise mechanism. Further investigations are necessary to clarify the contributions of jet-plate interaction effects at the trailing edges and co-flow effects in the shear layers to the overall noise levels.
  - ONERA performed numerical simulations with a full Immersed Boundary Method approach of the acoustic waves radiated from the UCAV intake considering a realistic mean flow field for different flow configurations, these numerical simulations showed the influence on the acoustic directivity of the flow generated by the suction at the intake which leads to a more homogeneous acoustic radiation pattern. Currently these simulations have been performed on a single frequency, other frequencies have not yet been considered and will be considered in a follow up activity as well as a comparison with the experimental data and other partners' results.

- Initial numerical simulations provided by FOI suggested an unexpected downwards deflection of the jet plume originating in the very complex design of the MULDICON nozzle. This was investigated and further confirmed with numerical simulations using hybrid RANS-LES as well as during the later acoustic wind tunnel tests. The investigation resulted in a mitigation design with an extension plate to straighten the jet plume.

- **Predicting noise reduction technology as an exercise in aeroacoustic design at agile NATO air vehicles, particularly at the MULDICON configuration.**

  The NASA work focused on a noise reduction technology, the Shielding Flap, that could be applied to the MULDICON vehicle. The conceptual development was followed by design of key parameters using the NASA PAASc scattering prediction method on the NACA 0012 airfoil two-dimensional geometry with a companion experimental study in the NASA QFF. Predictions on the two-dimensional cross-section geometry of the MULDICON were also completed. The next steps in the development are the design of the Shielding Flap for the three-dimensional DLR MULDICON wind tunnel model and testing in the DLR NWB wind tunnel. Both of these steps could be taken in future work.

  Significant conclusions have been made with the work accomplished, including:

  - At the current level of development, the Shielding Flap represents a promising noise reduction technology that could be considered for application to a vehicle like the MULDICON with propulsion noise sources above the airframe trailing edge.
  - For the MULDICON vehicle application, the Shielding Flap should be capable of providing, upon deployment, additional noise reduction for the three aft radiating noise sources of downstream turbomachinery noise, jet-trailing edge interaction noise, and jet noise.
  - The PAASc scattering prediction method, together with the QFF tests, have provided a capable toolset for the initial exploration and development of new technology like the Shielding Flap.
  - The NASA PAASc scattering prediction method was chosen for this application based on the experience that a method that is both physics-based and yet computationally very fast is a practical approach to understanding the effects of key parameters and for informing design decisions. The application to the Shielding Flap proved this approach to be valid with some 3150 parameter variations explored in the prediction matrix while providing understanding of the mechanisms involved. Supplementing the PAASc predictions with targeted CAA predictions from AVT-318 partners would be desirable in future work.
  - To further advance the maturation of the Shielding Flap technology, higher speed wind tunnel tests (higher than the QFF) with a full three-dimensional wind tunnel model and more realistic noise sources (as planned in DLR's NWB) would be necessary.

- **Code-to-code comparisons among partners, and a dedicated validation dataset from tests in an appropriate (i.e., large enough size) acoustic wind tunnel.**

  - An exceptional aeroacoustic database on the assessment of the effects of propulsion system installation has been established in AVT-318 from test campaigns in NASA QFF and DNW-NWB wind tunnels. A generic 2D (NACA0012) assessment of the Shielding Flap concept as well as intake and nozzle acoustic investigations at the realistic 3D DLR-F24 MULDICON UCAV configuration were measured successfully.
  - A major amount of work was invested in the development, design, and fabrication of the QFF Shielding Flap setup and DLR-F24 MULDICON UCAV setup. These two experimental facilities constitute major milestones which will enable further advanced investigations relevant to acoustic radiation and reduction for military unmanned air combat vehicle.

- In particular, the DLR-F24 MULDICON UCAV Model through its modular design allows for easy testing of variation in intake and nozzle designs and its impact on acoustic radiation. This capability should be used in future work to investigate various noise reduction concepts.
- The various simulation approaches available to the group were in part validated against the measured data; an effort which will be extended in future work. Code-to-code comparison of the results could not be realized in the time frame of AVT-318 and should be the subject of future work.

## 7.3 OUTLOOK

The results of AVT-318 call for the next logical step in the form of a follow-on AVT TG to now focus on the application of noise reduction technologies to the concurrent agile (unmanned) NATO air vehicle of MULDICON type. The new group will integrate the technology and testing capability steps made in the framework of AVT-318 to design, investigate and assess noise reduction concept to be applied at the MULDICON type vehicle. A follow-on activity would be naturally concerned with aeroacoustics and the related disciplines, i.e., aerodynamics of high-speed subsonic flows, including turbulence, and aircraft design. Specifically:

- Focus on the source noise and the aeroacoustic integration effects characteristic of highly integrated military vehicles because of the relevance to acoustic detectability during war time and annoyance and hearing loss to operators in peace time.
- Advancing the qualification of aircraft noise prediction methods regarding propulsion system integration effects including installation effects of complex intakes and exhausts.
- Source noise of MULDICON vehicle as representative of jet-powered agile military air vehicles.
- Aeroacoustic simulation (CFD/CAA) with tools of different fidelity: RANS+perturbations, scale resolving, and computational aeroacoustics (CAA) approaches. With the possibility to compare numerical simulation results with measurements from wind tunnel tests, tools may be further refined and adjusted.
- Using the understanding of the noise source and integration effects mechanisms, to develop a portfolio of noise reduction technologies and design approaches applicable to military vehicles.

# Chapter 8 – REFERENCES

[1] Cummings, R.M., Liersch, C.M., and Schütte, A. "Multi-Disciplinary Design and Performance Assessment of Effective, Agile NATO Air Vehicles," 2018 Applied Aerodynamics Conference, Atlanta, Georgia, June 2018, AIAA Paper 2018-2838.

[2] Edefur, H., Tormalm, M.H., Tysell, L., and Quas, M.J. "Design and Integration of a Low Observable Intake for the MULDICON Platform. AIAA Aviation and Aeronautics Forum and Exposition," Atlanta GA, June 2018, AIAA Paper 2018-3162.

[3] Rossignol, K.-S., Pott-Pollenske, M., Delfs, J., Kolb, A., and Patrick, Z. "A Novel Test Bed for the Aeroacoustic Investigation of UCAV Configurations with Highly Integrated Propulsion Systems," 28th AIAA/CEAS Aeroacoustics Conference, 2022, p. 2856. https://doi.org/10.2514/6.2022-2856

[4] Rossignol, K.-S., Delfs, J.W., Gély, D., Bulté, J., and Hutcheson, F. "Experimental Investigations on Noise Shielding: Dependency on Reference Noise Source and Testing Environment," Atlanta, USA, 2018.

[5] Rossignol, K.-S., and Delfs, J.W. "Analysis of the Noise Shielding Characteristics of a NACA0012 2D Wing," Lyon, France, 2016.

[6] Rossignol, K.-S., Pott-Pollenske, M., Delfs, J.W., Silbermann, J., and Pereira Gomes, J.M. "Investigating Noise Shielding by Unconventional Aircraft Configurations," in 23rd AIAA/CEAS Aeroacoustics Conference, Denver, 2017.

[7] De Gregorio F. "Free Compressible Jet Investigation," Experiments in Fluids, 55, p. 1693, 2014. https://doi.org/10.1007/s00348-014-1693-9

[8] Thomas, R.H., Burley, C.L., and Guo, Y. "Progress of Aircraft System Noise Assessment with Uncertainty Quantification for the Environmentally Responsible Aviation Project," 22nd AIAA/CEAS Aeroacoustics Conference, Lyon, France, May 2016, AIAA Paper 2016-3040.

[9] June, J.C., Thomas, R.H., and Guo, Y. "System Noise Prediction Uncertainty Quantification for a Hybrid Wing-Body Transport Concept," AIAA Journal, Vol. 58, No. 3, March 2020.

[10] Czech, M.J., Thomas, R.H., and Elkoby, R. "Propulsion Airframe Aeroacoustic Integration Effects of a Hybrid Wing Body Aircraft Configuration," International Journal of Aeroacoustics, Vol. 11 (3+4), pp. 335-368, 2012.

[11] Thomas, R.H., Czech, M.J., and Doty, M.J. "High Bypass Ratio Jet Noise Reduction and Installation Effects Including Shielding Effectiveness," 51st AIAA Aerospace Sciences Meeting including the New Horizons Forum and Aerospace Exposition, Grapevine, Texas, January 2013, AIAA Paper 2013-0541.

[12] Thomas, R.H., Burley, C.L., and Olson, E.D. "Hybrid Wing Body Aircraft System Noise Assessment with Propulsion Airframe Aeroacoustic Experiments," International Journal of Aeroacoustics, Vol. 11 (3+4), pp. 369-410, 2012.

[13] Thomas, R.H., Burley, C.L., and Nickol, C.L. "Assessment of the Noise Reduction Potential of Advanced Subsonic Transport Concepts for NASA's Environmentally Responsible Aviation Project," 54th AIAA Aerospace Sciences Meeting, San Diego, California, January 2016, AIAA Paper 2016-0863.

[14] Thomas, R.H. and Guo, Y. "Ground Noise Contour Prediction for a NASA Hybrid Wing Body Subsonic Transport Aircraft," 23rd AIAA/CEAS Aeroacoustics Conference, Denver, Colorado, June 2017, AIAA Paper 2017-3194.

[15] Thomas, R.H., Guo, Y., Berton, J., and Fernandez, H. "Aircraft Noise Reduction Technology Roadmap Toward Achieving the NASA 2035 Goal," 23rd AIAA/CEAS Aeroacoustics Conference, Denver, Colorado, June 2017, AIAA Paper 2017-3193.

[16] Clark, I.A., Thomas, R.H., and Guo, Y. "Aircraft System Noise of the NASA D8 Subsonic Transport Concept, " AIAA Journal of Aircraft, Vol. 58, No. 5, pp. 1106-1120, 2021.

[17] Guo, Y. Thomas, R.H., Clark, I.A., and June, J.C. "Far-Term Noise Reduction Roadmap for the Midfuselage Nacelle Subsonic Transport," AIAA Journal of Aircraft, Vol. 56, No. 5, 2019.

[18] June, J.C., Thomas, R.H., Guo, Y., and Clark, I.A. "Far Term Noise Reduction Technology Roadmap for a Large Twin-Aisle Tube-and-Wing Subsonic Transport," 25th AIAA/CEAS Aeroacoustics Conference, Delft, The Netherlands, May 2019, AIAA Paper 2019-2428.

[19] Thomas, R.H., Guo, Y., Clark, I.A., and June, J.C. "Challenges and Opportunities for Subsonic Transport X-Plane Acoustic Flight Research," 2018 AIAA/CEAS Aeroacoustics Conference, Atlanta, Georgia, June 2018, AIAA Paper 2018-3127.

[20] Zorumski, W.E. "Aircraft Noise Prediction Program Theoretical Manual," NASA TM-83199, 1982.

[21] Guo, Y. and Thomas, R.H. "Geometric Acoustics for Aircraft Noise Scattering," 28th AIAA/CEAS Aeroacoustics Conference, Southampton, UK, June 2022, AIAA Paper 2022-3077.

[22] Thomas, R.H. and Guo, Y. "Systematic Validation of the PAAShA Shielding Prediction Method," International Journal of Aeroacoustics, Vol. 21(5-7) pp. 558-584, 2022.

[23] Ahtye, W.F. and McCulley, G. "Evaluation of Approximate Methods for the Prediction of Noise Shielding by Airframe Components," NASA Technical Paper 1004, January 1980.

[24] Hutcheson, F.V., Bahr, C.J., Thomas, R.H., and Stead, D.J. "Experimental Study of Noise Shielding by a NACA 0012 Airfoil," 2018 AIAA/CEAS Aeroacoustics Conference, Atlanta, Georgia, June 2018, AIAA Paper 2018-2821.

[25] Hutcheson, F.V., Brooks, T.F., Burley, C.L., Bahr, C.J., Stead, D.J., and Pope, D.S. "Shielding of Turbomachinery Broadband Noise from a Hybrid Wing Body Aircraft Configuration," 20th AIAA/CEAS Aeroacoustics Conference, Atlanta, Georgia, June 2014, AIAA Paper 2014-2624.

[26] Thomas, R.H., Guo, Y., Clark, I.A., and June, J.C. "Propulsion Airframe Aeroacoustics and Aircraft System Noise Flight Research Test: NASA Overview," 28th AIAA/CEAS Aeroacoustics Conference, Southampton, UK, June 2022, AIAA Paper 2022-2993.

[27] Keller, J.B. "Geometrical Theory of Diffraction," Journal of the Optical Society of America, Vol. 52, No. 2, pp. 116-130, 1962.

[28] Keller, J. "Rays, Waves and Asymptotics," Bulletin of the Am. Math. Soc., Vol. 84, No. 5, pp. 727-750, 1978.

[29] Lewis, R.M., and Boersma, J. "Uniform Asymptotic Theory of Edge Diffraction," Math. Phys., Vol. 10, No. 12, pp. 2291-2305, 1969.

[30] Pierce, A.D. "Acoustics: An Introduction to its Physical Principles and Application," McGraw-Hill, 1981.

[31] Dowling, A.P., and Ffowcs Williams, J.E. "Sound and Sources of Sound," Ellis Horwood Publishers, 1983.

[32] Crighton, D.G., Dowling, A.P., Ffowcs Williams, J.E., Heckl, M., and Leppington, F.G. "Modern Methods in Analytical Acoustics," Springer-Verlag, 1992.

[33] Morse, P.M., and Ingard, K.U. "Theoretical Acoustics," McGraw-Hill, 1968.

[34] Sommerfeld, A. "Lectures on Theoretical Physics," Optics, Vol. IV, Academic Press, 1954.

[35] Levy, B. and Keller, J.B. "Diffraction by a Smooth Object," Communications on Pure and Applied Mathematics, Vol. 12, pp. 159-209, 1959.

[36] Agarwal, A., Dowling, A.P., Shin, H.C., Graham, W., and Sefi, S. "A Ray Tracing Approach to Calculate Acoustic Shielding by the Silent Aircraft Airframe," 12th AIAA/CEAS Aeroacoustics Conference (27th AIAA Aeroacoustics Conference), Cambridge, Massachusetts, May 2006, AIAA Paper 2006-2618.

[37] Agarwal, A., and Dowling, A.P., "The Calculation of Acoustic Shielding of Engine Noise by the Silent Aircraft Airframe," 11th AIAA/CEAS Aeroacoustics Conference (26th AIAA Aeroacoustics Conference), Monterey, California, May 2005, AIAA Paper 2005-2996.

[38] van Rens, J.R.P., van Rens, B.J.E., Holten, T., and Ruijgrok, G.J.J. "Sound Level Prediction Using a Ray Tracing Algorithm for a Blended-Wing-Body," 6th AIAA/CEAS Aeroacoustics Conference, Lahaina, Hawaii, June 2000, AIAA Paper 2000-2069.

[39] Lummer, M. "Maggi-Rubinowicz Diffraction Correction for Ray-Tracing Calculations of Engine Noise Shielding," 14th AIAA/CEAS Aeroacoustics Conference (29th AIAA Aeroacoustics Conference), Vancouver, British Columbia, Canada, May 2008, AIAA 2008-3050.

[40] Colas, D.F.M. "A Diffraction Integral Based Turbomachinery Noise Shielding Method," Master's Thesis, Department of Aeronautics and Astronautics, Massachusetts Institute of Technology, 2011.

[41] Guo, Y.P., Pope, D.S., Burley, C.L., and Thomas, R.H. "Aircraft System Noise Shielding Prediction with a Kirchhoff Integral Method," 23rd AIAA/CEAS Aeroacoustics Conference, Denver, Colorado, June 2017, AIAA 2017-3196.

[42] Ganci, S. "A General Scalar Solution for the Half-Plane Problem," J. Mod. Opt., 42(8), pp. 1707-1711, August 1995.

[43] Umul, Y.Z. "Young-Kirchhoff-Rubinowicz Theory of Diffraction in the Light of Sommerfeld's Solution," J. Opt. Soc. Am. A, 25(11), pp. 2734-2742, November 2008.

[44] Waterhouse, R.V. "Diffraction Effects in a Random Sound Field," J. Acoust. Soc. Am., Vol. 35, No. 10, pp. 1610-1620, 1963.

[45] MacDonald, H.M. “A Class of Diffraction Problems,” Proc. Lond. Math. Soc., Vol. 14, pp. 410-427, 1915.

[46] Bromwich, A. “Diffraction of Waves by a Wedge,” Proc. Lond. Math. Soc., Vol. 14, pp. 450-463, 1915.

[47] Whipple, F.J.W. “Diffraction by a Wedge and Kindred Problems,” Proc. Lond. Math. Soc., Vol. 16, pp. 94-111, 1917.

[48] Biot, M.A., and Tolstoy, I. “Formulation of Wave Propagation in Infinite Media by Normal Coordinates with an Application to Diffraction,” J. Acoust. Soc. Am., Vol. 29, pp. 381-391, 1957.

[49] Sommerfeld, A. “Mathematical Theory of Diffraction,” Math. Ann., Vol. 47, pp. 317-374, 1896.

[50] Bauer, M., Dierke, J., and Ewert, R. “Application of a Discontinuous Galerkin Method to Discretize Acoustic Perturbation Equations,” AIAA JOURNAL, Vol. 49, No. 5, 2011.

[51] Lummer, M. “A Hybrid 3D Discontinuous Galerkin Code for CAA Applications,” 22nd AIAA/CEAS Aeroacoustics Conference, 2016.

[52] Lummer, M. “Computation and Validation of Acoustic Shielding at Realistic Aircraft Configurations,” 24th AIAA/CEAS Aeroacoustics Conference, 2018.

[53] Jacob, J., Malaspinas,O., and Sagaut, P. “A New Hybrid Recursive Regularised Bhatnagar-Gross-Krook Collision Model for Lattice Boltzmann Method-Based Large Eddy Simulation,” Journal of Turbulence, Taylor & Francis, pp. 1-26, 2018.

[54] Terracol, M., Manoha, E., Herrero, C., Labourasse, E., Redonnet, S., and Sagaut, P. “Hybrid Method for Airframe Noise Numerical Prediction,” Theoretical and Computational Fluid Dynamics, Vol. 19, pp. 197-227, 2005.

[55] Polacsek, C., Desquesnes, G., and Reboul, G. “An Equivalent-Source Model for Simulating Noise Generation in Turbofan Engines,” Journal of Sound and Vibration, Vol. 323, pp. 697-717, 2009.

[56] Redonnet, S., Desquesnes, G., Manoha, E., and Parzini, C. “Numerical Study of Acoustic Installation Effects with Computational Aeroacoustics Method,” AIAA Journal, Vol. 48, No. 5, pp. 929-937, 2010.

[57] Reboul, G., and Polacsek, C. “Towards Numerical Simulation of Fan Broadband Noise Aft Radiation from Aero-Engines,” AIAA Journal, Vol. 48, No. 9, pp. 2038-2048, 2010.

[58] Redonnet, S., and Druon, Y. “Computational Aeroacoustics of Realistic Co-Axial Engines,” AIAA Journal, Vol. 50, No. 5, pp. 1029-104, 2012.

[59] Redonnet, S., Manoha, E., and Sagaut, P. “Numerical simulation of propagation of small perturbations interacting with flows and solid bodies,” AIAA Paper, Vol. 3493, 2001.

[60] Redonnet, S. “Simulation de la propagation acoustique en présence d’écoulements quelconques et de structures solides, par résolution numérique des équations d’Euler,” Ph.D. thesis, Université Bordeaux 1, 2001.

[61] Lighthill, M.J. “On Sound Generated Aerodynamically. I. General Theory,” Proceedings of The Royal Soc. London, A211(1107), pp. 564-587, 1952.

[62] Eliasson, P. "EDGE, a Navier-Stokes Solver for Unstructured Grids," Proceedings of Finite Volumes for Complex Applications III, pp. 527-534, 2002.

[63] Ffowcs-Williams, J.E., and Hawkings, D.L. "Sound Generation by Turbulence and Surfaces in Arbitrary Motion," Phil. Trans. Roy Soc., 264(1151), pp. 321-342, 1969.

[64] Peng, S.-H., Tysell, L, Yao, H.-D., Davidsson, L, and Eriksson. L.-E. "CAA Analysis of a Wing Section with Flap Side-Edges Based on hybrid RANS-LES Computation," AIAA Paper 2015-2839, Dallas USA, 2015.

[65] Yao, H.-D., Davidsson, L, Eriksson. L.-E., Grundestam, O., Peng, S.-H., and Eliasson, P. "Surface Integral Analogy Approaches to Computing Noise Generated by a 3D High-Lift Wing Configuration," AIAA Paper 2012-0386, Nashville USA, 2012.

[66] Mary, I. "Flexible Aerodynamic Solver Technology in an HPC Environment," Maison de la Simulation Seminars, Vol. http://www.maisondelasimulation.fr/seminar/data/201611 slides 1.ppt , 2016.

[67] Péron, S., Renaud, T., Terracol, M., Benoit, C., and Mary, I. "An Immersed Boundary Method for Preliminary Design Aerodynamic Studies of Complex Configurations," 23rd AIAA Computational Fluid Dynamics Conference, Vol. (3623), 2017.

[68] Dandois, J., Mary, I., and Brion, V. "Large-Eddy Simulation of Laminar Transonic Buffet," Journal of Fluid Mechanics, Vol. 850, pp. 156-178, 2018.

[69] Renaud, T., Benoit, C., Péron, S., Mary, I., and Alferez, N. "Validation of an Immersed Boundary Method for Compressible Flows," AIAA Scitech 2019 Forum, Vol. 2179, 2019.

[70] Péron, S., Benoit, C., Renaud, T., and Mary, I. "An Immersed Boundary Method on Cartesian Adaptive Grids for the Simulation of Compressible Flows Around Arbitrary Geometries," Engineering with Computers, 2020.

[71] Tanguy, G., and Renaud, T. "Flow Field Assessment of the ONERA L1 Wind Tunnel Numerical Simulations," AVT-338-RSM Specialists' Meeting on Advanced Wind Tunnel Boundary Simulation, 2021.

[72] Spalart, P.R., and Allmaras, S.R. "A One-Equation Turbulence Model for Aerodynamic Flows," 30th Aerospace Sciences Meeting and Exhibit, AIAA Paper 92-0439, 1992.

[73] Nangia, R.K., Coppin, J., and Ghoreyshi, M. "A UCAV Wing Design, Assessment and Comparisons," AIAA Aviation and Aeronautics Forum and Exposition, Atlanta GA, June 2018.

[74] Schütte, A., Vormweg, J., Maye, R.G., and Jeans, T. "Aerodynamic Shaping Design and Vortical Flow Design Aspects of a 53deg Swept Flying Wing Configuration," AIAA Aviation and Aeronautics Forum and Exposition, Atlanta GA, June 2018.

[75] Dalenbring, M.J., Edefur, H., Falk, U., Tormalm, M.H., and Tysell, L. "IR Signature Design Effort for the MULDICON Configuration," AIAA Paper 2018-3167, AIAA Aviation and Aeronautics Forum and Exposition, Atlanta GA, June 2018.

[76] Schweiger, J.M., Cunningham, A., Sakarya, E., Dalenbring, M.J., and Voss, A. "Structural Design Efforts for the MULDICON Configuration," AIAA Paper 2018-3325, AIAA Aviation and Aeronautics Forum and Exposition, Atlanta GA, June 2018.

[77] Tysell, L. “An Advancing Front Grid Generation System for 3D Unstructured Grids,” ICAS-94-2.5.1, pp. 1552-1564, Proceedings of the 19th ICAS Congress, Anaheim USA, 1994.

[78] Tysell, L. “The TRITET Grid Generation System,” Proceedings of the 10th ISGG Conference on Numerical Grid Generation, Forth, Kreta, Greece: Soc. Of Grid Generation ISGG, 2007.

[79] Hellsten, A. “On the Solid-Wall Boundary Condition for w in the k – ω-Type Turbulence Modes,” Scientific Report No B-50, Series B, Helsinki University of Technology, 1998.

[80] Peng, S.-H. “Hybrid RANS-LES Modelling Based on Zero- and One-Equation Models for Turbulent Flow Simulation,” Proc. Of 4th Int. Symp. Turb. And Shear Flow Phenomena, pp. 1159-1164, Vol. 3, 2005.

[81] Peng, S.-H. “Algebraic Hybrid RANS-LES Modelling Applied to Incompressible and Compressible Turbulent Flows,” San Francisco USA, 2006, AIAA Paper 2006-3910.

[82] Tam, C., Golebiowski, M., and Seiner, J. “On the Two Components of Turbulent Mixing Noise from Supersonic Jets,” Aeroacoustics Conference, p. 1716, 1996. https://doi.org/10.2514/6.1996-1716

[83] Tam, C.K.W., Viswanathan, K., Ahuja, K.K., and Panda, J. “The Sources of Jet Noise: Experimental Evidence,” Journal of Fluid Mechanics, Vol. 615, 2008, pp. 253-292. https://doi.org/10.1017/S0022112008003704

[84] Yu, J., and Tam, C. “Experimental Investigation of the Trailing Edge Noise Mechanism,” AIAA Journal, Vol. 16, No. 10, pp. 1046-1052, 1978. https://doi.org/10.2514/3.61003

[85] Zaman, K., Fagan, A., Bridges, J., and Brown, C. “An Experimental Investigation of Resonant Interaction of a Rectangular Jet with a Flat Plate,” Journal of Fluid Mechanics, Vol. 779, pp. 751-775, 2015. https://doi.org/10.1017/jfm.2015.453.

[86] Tam, C., and Chandramouli, S. “Jet-Plate Interaction Tones Relevant to Over-the-Wing Engine Mount Concept,” Journal of Sound and Vibration, Vol. 486, 2020. https://doi.org/10.1016/j.jsv.2020.115378

[87] Michalke, A., and Michel, U. “Prediction of Jet Noise in Flight from Static Tests,” Journal of Sound and Vibration, Vol. 67, No. 3, pp. 341-367, 1979. https://doi.org/10.1016/0022-460X(79)90541-8

[88] Pilon, A., and Lyrintzis, A. “Integral Methods for Computational Aeroacoustics,” 35th Aerospace Sciences Meeting and Exhibit, p. 20, 1997.

NATO OTAN
Science & Technology Organization (STO)

# REPORT DOCUMENTATION PAGE

| 1. Recipient's Reference | 2. Originator's References | 3. Further Reference | 4. Security Classification of Document |
|---|---|---|---|
| | STO-TR-AVT-318<br>AC/323(AVT-318)TP/1203 | ISBN<br>978-92-837-2514-5 | PUBLIC RELEASE |

**5. Originator**

Science and Technology Organization
North Atlantic Treaty Organization
BP 25, F-92201 Neuilly-sur-Seine Cedex, France

**6. Title**

Low Noise Aeroacoustic Design for Turbofan Powered NATO Air Vehicles

**7. Presented at/Sponsored by**

This report contains the results of the RTG AVT-318 active in the period 2019 – 2023.

| 8. Author(s)/Editor(s) | 9. Date |
|---|---|
| Multiple | November 2024 |
| **10. Author's/Editor's Address** | **11. Pages** |
| Multiple | 112 |

**12. Distribution Statement**

This document is distributed in accordance with NATO Security Regulations and STO policies.

**13. Keywords/Descriptors**

Acoustic installation effects; Aeroacoustics; Barrier shielding method; Computational Aeroacoustics (CAA); Edge scattering; Engine integration; Fast multipole boundary element method; MULDICON configuration; Ray tracing; Shielding Flap; Sound diffraction; Sound reflection; Sound refraction; Sound shielding; UCAV

**14. Abstract**

This report contains the results of the RTG AVT-318 active in the period 2019 – 2023 and covering the establishment of validated methods to predict aeroacoustic installation effects of engine noise for highly integrated military aircraft. The background to the activity is to enable the inclusion of acoustics in the design process of military aircraft in the future with the objective to reduce annoyance in peace time operation and early detection in hostile surroundings in wartime operation. The AVT-318 Research Task Group executed a comprehensive research program to produce a validation database on two complementary test configurations. First, generic tests of the Shielding Flap concept were conducted in NASA Langley QFF facility using the basic NACA 0012 experimental approach developed by the AVT-233 task group. The Shielding Flap concept is a noise reduction device which aims at reducing aft-radiated noise. The Shielding Flap could be a deployable device, stowed in cruise in the underside of the MULDICON and deployed for noise-sensitive parts of a mission at lower speed, low-altitude flight conditions. Second, an experimental wind tunnel setup based on the MULDICON UCAV planform design (with origins in the AVT-251 task group), was adopted and modified to allow, from an experimental standpoint, the integration of complex curved intake and exhaust channels. The experimental setup allows the realization of a controlled high-velocity intake flow as well as a cold high-velocity exhaust jet. Experiments were successfully carried out in the DNW-NWB low-speed acoustic facility at DLR Braunschweig. Partners' flow and acoustic prediction methods, ranging from mid- to high-fidelity, were assessed to establish their capability to deal with more realistic and complex configurations.

NORTH ATLANTIC TREATY ORGANIZATION

SCIENCE AND TECHNOLOGY ORGANIZATION
BP 25
F-92201 NEUILLY-SUR-SEINE CEDEX
FRANCE
Télécopie 0(1)55.61.22.99

E-mail mailbox@cso.nato.int

## DIFFUSION DES PUBLICATIONS STO NON CLASSIFIEES

Les publications de l'AGARD, de la RTO et de la STO peuvent parfois être obtenues auprès des centres nationaux de distribution indiqués ci-dessous. Si vous souhaitez recevoir toutes les publications de la STO, ou simplement celles qui concernent certains Panels, vous pouvez demander d'être inclus soit à titre personnel, soit au nom de votre organisation, sur la liste d'envoi.

Les publications de la STO, de la RTO et de l'AGARD sont également en vente auprès des agences de vente indiquées ci-dessous.

Les demandes de documents STO, RTO ou AGARD doivent comporter la dénomination « STO », « RTO » ou « AGARD » selon le cas, suivi du numéro de série. Des informations analogues, telles que le titre est la date de publication sont souhaitables.

Si vous souhaitez recevoir une notification électronique de la disponibilité des rapports de la STO au fur et à mesure de leur publication, vous pouvez consulter notre site Web (http://www.sto.nato.int/) et vous abonner à ce service.

## CENTRES DE DIFFUSION NATIONAUX

**ALLEMAGNE**
BAIUDBw FA IV
Fachinformationszentrum der Bundeswehr
Ausleihservice Hardthöhe, Haus 208
Fontainengraben 150, 53123 Bonn

**BELGIQUE**
Royal High Institute for Defence – KHID/IRSD/RHID
Management of Scientific & Technological Research for Defence, National STO Coordinator
Royal Military Academy – Campus Renaissance
Renaissancelaan 30, 1000 Bruxelles

**BULGARIE**
Ministry of Defence
Defence Institute "Prof. Tsvetan Lazarov"
"Tsvetan Lazarov" bul no.2, 1592 Sofia

**CANADA**
DGSIST 2
Recherche et développement pour la défense Canada
60 Moodie Drive (7N-1-F20), Ottawa, Ontario K1A 0K2

**DANEMARK**
Danish Acquisition and Logistics Organization
Lautrupbjerg 1-5, 2750 Ballerup

**ESPAGNE**
Área de Cooperación Internacional en I+D
SDGPLATIN (DGAM), C/ Arturo Soria 289
28033 Madrid

**ESTONIE**
Estonian National Defence College
Centre for Applied Research
Riia str 12, Tartu 51013

**ETATS-UNIS**
Defense Technical Information Center
8725 John J. Kingman Road
Fort Belvoir, VA 22060-6218

**FINLAND**
Ministry for Foreign Affairs
Telecommunications Centre (24/7)
P.O Box 176, FI-00023 Government

**FRANCE**
O.N.E.R.A. (ISP)
29, Avenue de la Division Leclerc
BP 72, 92322 Châtillon Cedex
O.N.E.R.A. (ISP)

**GRECE (Correspondant)**
Defence Industry & Research General Directorate, Research Directorate
Fakinos Base Camp, S.T.G. 1020
Holargos, Athens

**HONGRIE**
Hungarian Ministry of Defence
Development and Logistics Agency
P.O.B. 25, H-1885 Budapest

**ITALIE**
Ten Col Renato NARO
Capo servizio Gestione della Conoscenza
F. Baracca Military Airport "Comparto A"

**LUXEMBOURG**
Voir Belgique

**NORVEGE**
Norwegian Defence Research Establishment, Attn: Biblioteket
P.O. Box 25, NO-2007 Kjeller

**PAYS-BAS**
Royal Netherlands Military Academy Library
P.O. Box 90.002, 4800 PA Breda

**POLOGNE**
Centralna Biblioteka Wojskowa
ul. Ostrobramska 109,
04-041 Warszawa

**PORTUGAL**
Estado Maior da Força Aérea
SDFA – Centro de Documentação
Alfragide, P-2720 Amadora

**ROUMANIE**
Romanian National Distribution Centre
Armaments Department
9-11, Drumul Taberei Street
Sector 6
061353 Bucharest

**ROYAUME-UNI**
Dstl Records Centre
Rm G02, ISAT F, Building 5
Dstl Porton Down
Salisbury SP4 0JQ

**SLOVAQUIE**
Akadémia ozbrojených síl gen.
M.R. Štefánika, Distribučné a informačné stredisko STO
Demänová 393
031 01 Liptovský Mikuláš 1

**SLOVENIE**
Ministry of Defence
Central Registry for EU & NATO
Vojkova 55
1000 Ljubljana

**SUEDE**
Regeringskansliet,
Attn: Adam Hidestå
RK IF AR 5
S-103 33 Stockholm

**TCHEQUIE**
Vojenský technický ústav s.p.
CZ Distribution Information
Mladoboleslavská 944
PO Box 18, 197 06 Praha 9

**TURQUIE**
Milli Savunma Bakanlığı (MSB)
ARGE ve Teknoloji Dairesi Başkanlığı
06650 Bakanliklar – Ankara

## AGENCES DE VENTE

**The British Library Document Supply Centre**
Boston Spa, Wetherby
West Yorkshire LS23 7BQ
ROYAUME-UNI

**Canada Institute for Scientific and Technical Information (CISTI)**
National Research Council Acquisitions
Montreal Road, Building M-55
Ottawa, Ontario K1A 0S2, CANADA

Les demandes de documents STO, RTO ou AGARD doivent comporter la dénomination « STO », « RTO » ou « AGARD » selon le cas, suivie du numéro de série (par exemple AGARD-AG-315). Des informations analogues, telles que le titre et la date de publication sont souhaitables. Des références bibliographiques complètes ainsi que des résumés des publications STO, RTO et AGARD figurent dans le « NTIS Publications Database » (http://www.ntis.gov).

NORTH ATLANTIC TREATY ORGANIZATION

SCIENCE & TECHNOLOGY ORGANIZATION
BP 25
F-92201 NEUILLY-SUR-SEINE CEDEX
FRANCE
Télécopie 0(1)55.61.22.99

E-mail mailbox@cso.nato.int

## DISTRIBUTION OF UNCLASSIFIED STO PUBLICATIONS

AGARD, RTO & STO publications are sometimes available from the National Distribution Centres listed below. If you wish to receive all STO reports, or just those relating to one or more specific STO Panels, they may be willing to include you (or your Organisation) in their distribution.

STO, RTO and AGARD reports may also be purchased from the Sales Agencies listed below.

Requests for STO, RTO or AGARD documents should include the word 'STO', 'RTO' or 'AGARD', as appropriate, followed by the serial number. Collateral information such as title and publication date is desirable.

If you wish to receive electronic notification of STO reports as they are published, please visit our website (http://www.sto.nato.int/) from where you can register for this service.

## NATIONAL DISTRIBUTION CENTRES

**BELGIUM**
Royal High Institute for Defence – KHID/IRSD/RHID
Management of Scientific & Technological Research for Defence, National STO Coordinator
Royal Military Academy – Campus Renaissance
Renaissancelaan 30, 1000 Brussels

**BULGARIA**
Ministry of Defence
Defence Institute "Prof. Tsvetan Lazarov"
"Tsvetan Lazarov" bul no.2, 1592 Sofia

**CANADA**
DSTKIM 2
Defence Research and Development Canada
60 Moodie Drive (7N-1-F20)
Ottawa, Ontario K1A 0K2

**CZECHIA**
Vojenský technický ústav s.p.
CZ Distribution Information Centre
Mladoboleslavská 944
PO Box 18, 197 06 Praha 9

**DENMARK**
Danish Acquisition and Logistics Organization (DALO)
Lautrupbjerg 1-5, 2750 Ballerup

**ESTONIA**
Estonian National Defence College
Centre for Applied Research
Riia str 12, Tartu 51013

**FINLAND**
Ministry for Foreign Affairs
Telecommunications Centre (24/7)
P.O Box 176, FI-00023 Government

**FRANCE**
O.N.E.R.A. (ISP)
29, Avenue de la Division Leclerc – BP 72
92322 Châtillon Cedex

**GERMANY**
BAIUDBw FA IV
Fachinformationszentrum der Bundeswehr
Ausleihservice Hardthöhe, Haus 208
Fontainengraben 150, 53123 Bonn

**GREECE (Point of Contact)**
Defence Industry & Research General Directorate, Research Directorate
Fakinos Base Camp, S.T.G. 1020
Holargos, Athens

**HUNGARY**
Hungarian Ministry of Defence
Development and Logistics Agency
P.O.B. 25, H-1885 Budapest

**ITALY**
Ten Col Renato NARO
Capo servizio Gestione della Conoscenza
F. Baracca Military Airport "Comparto A"
Via di Centocelle, 301, 00175, Rome

**LUXEMBOURG**
*See* Belgium

**NETHERLANDS**
Royal Netherlands Military Academy Library
P.O. Box 90.002, 4800 PA Breda

**NORWAY**
Norwegian Defence Research Establishment, Attn: Biblioteket
P.O. Box 25, NO-2007 Kjeller

**POLAND**
Centralna Biblioteka Wojskowa
ul. Ostrobramska 109
04-041 Warszawa

**PORTUGAL**
Estado Maior da Força Aérea
SDFA – Centro de Documentação
Alfragide, P-2720 Amadora

**ROMANIA**
Romanian National Distribution Centre
Armaments Department
9-11, Drumul Taberei Street, Sector 6
061353 Bucharest

**SLOVAKIA**
Akadémia ozbrojených síl gen. M.R. Štefánika, Distribučné a informačné stredisko STO
Demänová 393
031 01 Liptovský Mikuláš 1

**SLOVENIA**
Ministry of Defence
Central Registry for EU & NATO
Vojkova 55, 1000 Ljubljana

**SPAIN**
Área de Cooperación Internacional en SDGPLATIN (DGAM)
C/ Arturo Soria 289
28033 Madrid

**SWEDEN**
Regeringskansliet, Attn: Adam Hidestål
RK IF AR 5
S-103 33 Stockholm

**TÜRKIYE**
Milli Savunma Bakanlığı (MSB)
ARGE ve Teknoloji Dairesi Başkanlığı
06650 Bakanliklar – Ankara

**UNITED KINGDOM**
Dstl Records Centre
Rm G02, ISAT F, Building 5
Dstl Porton Down,
Salisbury SP4 0JQ

**UNITED STATES**
Defense Technical Information Center
8725 John J. Kingman Road
Fort Belvoir,
VA 22060-6218

## SALES AGENCIES

**The British Library Document Supply Centre**
Boston Spa, Wetherby
West Yorkshire LS23 7BQ
UNITED KINGDOM

**Canada Institute for Scientific and Technical Information (CISTI)**
National Research Council Acquisitions
Montreal Road, Building M-55
Ottawa, Ontario K1A 0S2, CANADA

Requests for STO, RTO or AGARD documents should include the word 'STO', 'RTO' or 'AGARD', as appropriate, followed by the serial number (for example, AGARD-AG-315). Collateral information such as title and publication date is desirable. Full bibliographical references and abstracts of STO, RTO and AGARD publications are given in "NTIS Publications Database" (http://www.ntis.gov).

ISBN 978-92-837-2514-5